5-4-2017

Simulations with Radiative3D: A software tool for radiative transport in 3-D Earth models

Christopher J. Sanborn
University of Connecticut - Storrs, christopher.sanborn@uconn.edu

Simulations with Radiative3D: A software tool for radiative transport in 3-D Earth models

Christopher John Sanborn, Ph.D.
University of Connecticut, 2017

This dissertation presents RADIATIVE3D, a computer code for radiative transport simulations of seismic events, including earthquakes and explosions, in 3-D Earth models, and allowing output of seismogram envelopes from virtual seismometers or information representing bulk energy transport through the model. Radiative transport is an efficient algorithm for Monte-Carlo simulation of high-frequency elastic wavefield energy transport through models featuring both large-scale (larger than wavelength) structure, simulated by deterministic ray tracing, and small-scale structure (wavelength scale and smaller), simulated by a stochastic scattering process. The 3-D models are composed of a collection of adjoining model cells inside of which material properties have simple mathematical description. Within cells, the deterministic mechanism implements curved ray paths in linear gradient background media, and the stochastic mechanism implements pseudo-random preferential scattering based on a formulation that computes mean-free-path and scattering cross sections from a characterization of material heterogeneity in which fluctuation of elastic properties are assumed to follow a von Kármán spectrum of scale lengths. Between cells, material properties may be continuous or discontinuous, in which case reflections and refractions may occur. At the model's surface, virtual seismometers may be emplaced to record signal channels representative of seismogram envelopes. After introducing the code and theory of operations, two chapters describing initial experiments with the code are presented. In Chapter 4, we present experiments in layered Earth models exploring the effects of variations in the heterogeneity spectrum and their effect on seismic coda generation. In Chapter 5 we present experiments in which crust structure is subject to localized thinning or thickening, simulating graben structures or mountain structures, and analyze their contribution to blockage of the Lg and Pg seismic phases at distant seismometers. We conclude with a roadmap describing the future continued development of RADIATIVE3D.

Simulations with Radiative3D: A software tool for radiative transport in 3-D Earth models

Christopher John Sanborn

B.S. University of Connecticut, 2003

M.S. University of Connecticut, 2011

A Dissertation

Submitted in Partial Fulfillment of the

Requirements for the Degree of

Doctor of Philosophy

at the

University of Connecticut

2017

APPROVAL PAGE

Doctor of Philosophy Dissertation

Simulations with Radiative3D: A software tool for radiative transport in 3-D Earth models

Presented by

Christopher John Sanborn, B.S., M.S.

Major Advisor _____
Vernon F. Cormier

Associate Advisor _____
Richard Jones

Associate Advisor _____
Michael C. Fehler

University of Connecticut

2017

ACKNOWLEDGMENTS

I would like to thank, first off, my advisor, Dr. Vernon Cormier, for his patience, guidance, and feedback, all of which have been enormously helpful in the completion of this dissertation. Despite the duration of this project, it has been, in the overall, quite enjoyable to work on, and having good academic support has been immeasurably important in that outcome. I thank also my associate advisors, Dr. Richard Jones and Dr. Michael Fehler, for invaluable feedback that has refined this dissertation. Additionally, I would like to acknowledge the Air Force Research Laboratories (AFRL) and Air Force Technical Applications Center (AFTAC), for providing the funding that made this project possible, and for being a cool group of scientists to work and interact with.

In addition, I thank the various fruits, nuts, berries, achenes, and samaras of my family tree, without whom, and without whose support and inspiration, I would not have been who I am or chosen the paths I have chosen, to arrive at this work, such as it is. Your contributions have been invaluable. Special mention goes out to my wonderful daughter, Dagny Elizabeth, without whom this dissertation would likely have been completed in less time, as she is and always will be the prime focus of my life, along with her mother, and any future progeny not yet known at the time of this writing.

Lastly, there is a rather large group of fellow physics graduate students and undergraduate students with whom I have spent time, now spanning, in fact, three calendar decades (though thankfully less than two counting just elapsed time), who have made the whole journey, from freshman to Ph.D., memorable and fruitful beyond compare. Though their direct contribution to this dissertation is perhaps hard to explain, I nevertheless throw particular shout outs to Cory Merow, Ron Pepino, and Mark Koudstaal. Numerous others are deserving of mention, but will have to settle for implicit rather than explicit inclusion.

Contents

List of Figures

Chapter 1

Introduction: Simulation in Seismology

This dissertation serves primarily to describe, in overview, a software package called RADIATIVE3D, planned and developed by Christopher J. Sanborn (myself) with guidance from my advisor, Vernon Cormier. A fellow student, Steven Walsh, whom I mentored during this process, also made significant contributions, under my guidance, to important components of the source code. RADIATIVE3D is a code for radiative transport simulations in three-dimensional Earth models, and allows for the simulation of synthetic seismic waveforms, such as would be recorded by a seismometer at a location of interest, or, for the wave front simulation of body-waves propagating through Earth models. An additional purpose of this dissertation is to present some initial models and simulations addressing real-world research questions that have been performed by me and members of our group during the timeframe covered by this dissertation.

A dissertation of this nature — one which describes a software code — cannot really stand on its own, as the source code itself will always be the primary documentation of what the software does. As such, the reader will frequently be referred to the source code (it is well commented) for complete details of operation or implementation, though an attempt will be made to provide enough detail here to provide the

reader the best possible chance of being able to functionally use the software or of being able to reasonably understand the source code at first read. Additionally, the author has been continuously building a "wiki" detailing the internal operation and usage of the code throughout the development process, and this too serves as an important additional resource to this dissertation.

The source code, as it stands at the time of this document, can be perused at the following location: (This is a link to a "tagged" branch of the code, recording its state at the time of this writing. In the future, of course, the code will evolve. For the *latest* version of the code, please contact the author, or find a link on the project homepage.)

```
https://rainbow.phys.uconn.edu/geophysics/trac/browser/
                Radiative3D/tags/dissertation
```

For the wiki, please browse to this location, which also serves for the time being as the project's temporary home page:

```
   https://rainbow.phys.uconn.edu/geowiki/Radiative3D
```

1.1 Simulation for event discrimination

1.1.1 Motivation

Nuclear test monitoring for enforcement of nuclear test ban treaties depends on the ability to discriminate between explosion events and naturally occurring earthquake events. In seismic data, the differences between explosions and earthquakes are greatest in the highest recordable frequency band. This motivates the development of high-frequency synthetics tools, which can be used to enhance understanding of or refine models of local and regional Earth structure. As frequency increases and wavelengths decrease, the seismic wavefield becomes sensitive to smaller-scale structure, including

the microstructure of material heterogeneity. This heterogeneity becomes a source of scattering and has important effects on seismic signals, including coda generation, in which otherwise sharp peaks on a seismogram are softened and develop long tails due the cumulative effects of deflectionary scattering. Modeling this small-scale structure with elastic solvers becomes prohibitive because of the grid fineness needed to capture features of this size and to accurately represent the short-wavelength wavefield. Radiative transport provides an alternative, by removing the need to model a wavefield in its entirety (radiative transport uses ray optics, not wave dynamics), and by using separate methodologies for the handling of small-scale (on the order of a wavelength) and large-scale (much longer than a wavelength) structure.

1.1.2 Overview of radiative transport for seismological simulation

Radiative transport is a form of Monte Carlo simulation in which the transport of energy in a model is simulated by a combination of stochastic and deterministic dynamics. In our implementation, monochromatic elastic energy is considered to originate from a source event at a fixed location and time. A quantity of that energy is then propagated as a discrete packet or bundle, which we refer to as a phonon[1] (in loose analogy to the particle representation of light as a stream of photons carrying electromagnetic energy). A phonon's path through the model is determined via a combination of ray theory to handle the deterministic propagation through the composite-medium background structure (large scale structure, capturing broad variations in elastic properties), and scattering theory, which is the stochastic handling of scattering due to small-scale heterogeneities, assumed as perturbations to the large-scale background

[1]The use of the word *phonon* here may be controversial, due to the very specific usage of the word in works describing quantized excitations of crystal latices in solid state physics (e.g. Kittel, 2004). The author of the current work is not intending any suggestion of non-classical handling of the elastic wavefield in macroscopic seismic models, but nevertheless believes the word has utility as a familiar conceptual device referring to a carrier of a specific quantity of elastic energy.

structure. A scattering event is, in essence, an interruption and randomization of a particle's otherwise deterministic progress. With a sufficient number of phonons emitted from the source event, a picture of the energy transport throughout the model begins to emerge. Records of the phonon travel paths can be used either in bulk or via selection criteria to visualize this energy transport. In bulk, the data can be used to produce movies or still-frames of the evolving wavefront throughout the 3-dimensional model. Via selection criteria, just those phonons that, for example, interact with the surface within a specified gather radius of a hypothetical seismometer can be collected and used to produce seismic waveforms of surface movement at the given location. With a sufficient quantity of virtual seismometers, travel-time curves can also be produced.

1.1.3 Why radiative transport

The principal advantage of radiative transport is the ability to simulate via Monte-Carlo techniques small-scale structure without the need for model meshes that are dense enough to explicitly describe that structure. Instead, the model mesh describes only the large-scale background medium, against which small-scale heterogeneities are assumed as a random perturbation field. The small-scale heterogeneities of the Earth model are characterized in the aggregate via a small number of statistical parameters, rather than described in fine detail as an explicit perturbation field. This represents a dramatic reduction in the storage requirements needed to describe the Earth model. Additionally, since radiative transport is not a numerical wave-equation solver, it also avoids the requirement for a simulation grid dense enough to capture the temporal and spatial derivatives in the full equations of motion. Thus, models are described with what we call a "model mesh" rather than a "simulation grid," where the necessary model mesh density is determined by the model features we wish to capture, rather than by the wavelengths we wish to simulate. (C.f. numerical finite dif-

ference methods, which might require as many as 10 grid points per wavelength. This would quickly become a limiting factor on the spatial extent of models, making models covering large distances practically infeasible.)

This sparse-mesh advantage depends on the ability to categorically separate structure into large and small scales. In general, the distinction is made by comparison of the feature size to the wavelength being simulated. Large structure is that for which $ka \gg 1$, where a is a typical feature size and k is the wavenumber corresponding to the chosen wavelength, and small scale is, for radiative transport purposes, structure for which $ka \sim 1$, which is the regime in which scattering is most prominent. Radiative transport simulations are usually carried out at a single frequency, and this choice of frequency establishes the reference size for this distinction. Our frequency range of interest is the 1 Hz to 10 Hz band, which at typical seismic velocities of 3 to 8 km/s, establishes "small scale" in the approximate range of 0.3 km to 8.0 km or smaller, and means that node spacing on our model meshes can be much larger than that.

For practical modeling purposes, large-scale structure is that which comes from published velocity models of the Earth, in which seismic wave velocities have been mapped out by tomographic inversion or other methods. Typically, these tomographic maps are either inverted from longer wavelength signals than the high-frequency signals that are of interest to us, or, in the imaging process, have had smaller-scale structure smoothed over in the regularization process required to mitigate effects of travel-time measurement errors, and thus these inversions map out the long-wavelength equivalent or composite medium average seismic velocities, which is to say they are maps of the large-scale structure. These large-scale velocity maps then form the backdrop against which small-scale heterogeneities are assumed as a perturbation field, for use in generating higher-frequency synthetics. The advantage of radiative transport is the ability to describe this perturbation field statistically and to simulate it stochas-

tically, rather than deterministically, even as the large-scale structure is handled by deterministic ray tracing.

The practical mesh fineness required to describe deterministic structure is application-specific, and can vary quite a bit. Node spacings of 10's to 100's of kilometers for lateral variations, and five to 20 kilometers for vertical variation, could be considered well within the range of typical. But a typical scale length for the material heterogeneities that become the perturbation field might easily span 0.01 to 10.0 kilometers. If features of these scale lengths were to be described explicitly, the model mesh storage requirements would increase by many orders of magnitude.

1.1.4 Necessary capabilities

A useful simulation tool for seismic modeling of heterogeneous Earth structure for purposes of understanding earthquake vs. explosion discrimination must have certain basic features, including: (1) the ability to realistically model both earthquake and explosion source events, which have distinct radiation patterns, (2) the ability to utilize descriptive Earth models that specify velocity, density, intrinsic attenuation (from internal friction, i.e. heat), and heterogeneity statistics in laterally as well as vertically varying models, and (3) the ability to output signal streams that are representative of the evolving energy propagation within the model. These will be expounded upon in what follows.

Source modeling

RADIATIVE3D uses a moment-tensor representation to describe seismic sources. Moment tensor representation is a truncation at quadrupole order of the multipole expansion of the elastic wave field at large distances from the source, and thus provides a way to parameterize complex sources as a point-source equivalent (Archambeau,

1968). Despite discarding higher-order multipoles, moment tensors provide good representation of a wide range of naturally occurring and man-made seismic sources. Both idealized shear dislocation (e.g. slip on a fault plane) and idealized explosions are exactly representable by moment tensors. In fact, the six degrees of freedom in the rank-2 symmetric moment tensor allow for the specification of a full range of event types from pure isotropic (explosion/implosion), to double couple (shear-dislocation earthquake), and various other configurations such as compensated linear vector dipole (CLVD), etc. Internally, RADIATIVE3D converts moment tensors into probability distributions describing the likelihood of phonon emission at various take-off angles from the event source.

Earth modeling and scattering

As a phonon propagates through the Earth model, its progress is determined by a combination of deterministic and stochastic dynamics. The deterministic part of a phonon's path is calculated by raytracing through a background model of explicitly defined Earth structure, in which the elastic wave velocities of longitudinally polarized P waves and transversely polarized S waves, the material density, and the intrinsic attenuation quality factor (Q) are specified. The stochastic dynamics are the randomized disruptions of the phonon trajectory that arise from scattering, and depend on statistically described structure (heterogeneity). A scattering event involves an interruption of a phonon ray trajectory at a scattering location and a re-radiation of the phonon at a deflected angle. The angular dependence of scattering is determined by the scattering shapes outlined in Sato, Fehler, and Maeda (2012), and is dependent on four statistical parameters describing heterogeneity, as well as on the background P and S elastic velocities, and on frequency. Like event sources, the scattering shapes are also represented internally as probability distributions characterizing the relative likelihood of

various deflection angles.

Signal output

Radiative3D has two basic output modes. The first is a play-by-play event stream that reports everything that happens to a phonon from generation at the source event until eventual phonon-death as the phonon either leaves the model boundaries, or is abandoned after its lifetime exceeds the window of interest. Attributes of the phonon at each time point are also reported, including position, orientation, polarization state, amplitude, and accumulated path length. This mode can be used for volumetric visualization of energy propagation throughout the whole model. The second output stream is the time-binned signals from virtual seismometers that collect and report on the energy accumulated at fixed points on the model surface. These can be used to generate synthetic seismograms (as energy envelopes) or synthetic travel-time curves.

1.2 Source mechanisms and moment tensors

Earthquakes and other seismic events are the results of complex ruptures, sudden displacements, or other disturbances (explosions, for example) occurring within a localized region at or below some location on the Earth's surface. The surface location most proximate to the disturbance is called the *epicenter*. When information is known about the depth of the disturbance, the location below the surface is referred to as the *hypocenter*. Elastic waves radiating from the seismic event can be categorized based on polarization mode. Longitudinally polarized waves are referred to as *P waves*, and transversely polarized waves are referred to as *S waves*. In general, P waves propagate with higher velocity than S waves in the same media.

The disturbance at the source of the seismic event will have some finite volume, and

will involve potentially quite complicated motions of the Earth within that volume, giving rise to a multitude of possible wave excitations that radiate energy to the far reaches of the globe. The pattern of that radiation, if predictable, measurable, and interpretable, can give information to seismologists about the nature of the disturbance that originated the source event.

Although the complexity of the source displacements can result in very difficult to interpret ground motions within the immediate vicinity of the source, at larger distances more ordered ground motions are observable, and these lend themselves to categorization of the source disturbance based on a six-element tensorial quantity called the *moment tensor*. The moment tensor parameterization is based on a series expansion of the source displacement field, truncated at second order. In essence, the moment tensor parameterization allows one to treat the source event as a point-source, with six degrees of freedom characterizing magnitude (one d.f.), wavefront initial shape (two d.f.), and orientation (three d.f.). The ground motions computed by this parameterization have high predictive power for naturally occurring events (as well as many man-made events) at sufficiently large distances from the source event, called the *far-field*. (At closer distances, higher-order *near-field* terms can dominate and substantially increase the complexity of the wave field. For example, P and S waves do not cleanly separate at near-field distances.) For a more complete discussion of why these six parameters are sufficient for the purpose of source characterization, see e.g. Aki and Richards (1980).

1.2.1 Moment and energy release

The utility of moment tensor representation lies primarily in describing the radiation patterns of P and S wavefronts emanating from the source. Thus one might, for modeling or analysis purposes, restrict oneself to dimensionless moment tensors of unit

tensorial magnitude (effectively dropping one degree of freedom), and treating the magnitude separately. The magnitude of a moment tensor can be thought of as correlating with the energy release of a seismic event, although it is not a direct equivalency.

The seismic moment, M_0, is a scalar quantity representing the magnitude of the moment tensor. For an idealized earthquake resulting from a fault rupture of area A in a medium with rigidity μ, this quantity is given by Aki and Richards, p. 117 as:

$$M_0 = \mu A \bar{u} \tag{1.1}$$

where $\bar{u}$ is the displacement along the fault, averaged over the fault area. M_0 has dimensions:

$$[M_0] = [\mu]\,[A]\,[\bar{u}] = \text{Pressure} \cdot \text{Length}^3 = \text{Energy} \tag{1.2}$$

and is proportional to (though not equal to) the strain energy W released by the seismic event. Kanamori (1977) shows that, for large earthquakes, W and M_0 are related by an approximate factor of

$$W \sim M_0 \,/\, \left(2 \times 10^4\right) \tag{1.3}$$

for a complete stress drop, or a lesser quantity for a partial stress drop. Under ideal conditions, all of this energy goes into the elastic waves. Under less than ideal conditions, some of the energy will be absorbed by inelastic deformation in the source region.

In the case of a rupture along a fault plane with orientation and fault motion described by strike, dip, and rake parameters ϕ_s, δ, and λ, respectively, Aki and Richards

give the full cartesian moment tensor elements, in terms of M_0, as:

$$M_{xx} = -M_0 \left(\sin\delta\cos\lambda\sin 2\phi_s + \sin 2\delta\sin\lambda\sin^2\phi_s\right), \tag{1.4a}$$

$$M_{xy} = \quad M_0 \left(\sin\delta\cos\lambda\cos 2\phi_s + \tfrac{1}{2}\sin 2\delta\sin\lambda\sin 2\phi_s\right) = M_{yx}, \tag{1.4b}$$

$$M_{xz} = -M_0 \left(\cos\delta\cos\lambda\cos\phi_s + \cos 2\delta\sin\lambda\sin\phi_s\right) = M_{zx}, \tag{1.4c}$$

$$M_{yy} = \quad M_0 \left(\sin\delta\cos\lambda\sin 2\phi_s - \sin 2\delta\sin\lambda\cos^2\phi_s\right), \tag{1.4d}$$

$$M_{yz} = -M_0 \left(\cos\delta\cos\lambda\sin\phi_s - \cos 2\delta\sin\lambda\cos\phi_s\right) = M_{zy}, \tag{1.4e}$$

$$M_{zz} = \quad M_0 \sin 2\delta\sin\lambda \tag{1.4f}$$

Because of the infeasibility of measuring rupture areas or energy releases directly, seismologists rely on numerous ways of estimating the magnitude of real-life seismic events, and there are several magnitude scales in common use based on seismic observables. (These magnitude scales include, e.g. body-wave magnitude m_b, surface-wave magnitude M_s, and others.) A useful conceptual link between these observable magnitudes and not-directly-observable seismic moments exists in the moment magnitude scale, M_W, where M_W is given by (Kanamori, 1977):

$$M_W = \frac{2}{3}\log_{10}\left(M_0\right) - 10.7 \tag{1.5}$$

Here, M_0 is expressed in $\mathrm{dyne}\cdot\mathrm{cm}$, and the constants are chosen by convention to establish comparability between the moment magnitude scale and other magnitude scales.

1.2.2 Characterizing focal mechanisms

Moment tensors can be expressed as 3×3 matrices. The tensor represents the source terms for a range of point-source solutions to the elastic wave equation in the far field radiation domain, including radiation patterns typical of earthquakes, explosions, cav-

ity collapses from mining operations, and other naturally occurring or artificial sources with reasonably simple mechanisms. The term *far field* means at distances large enough that, though the geometry of the seismic event may be spatially distributed, approximation as a point source is valid. There are nine elements (and thus nine degrees-of-freedom, "DF's") in a 3×3 matrix. However, physical constraints of naturally-occurring stress-release seismic events (specifically, that no net torque be released by the source event) require transpose symmetry of the moment tensor matrix. This symmetry means that focal mechanism moment tensors, in actuality, have only six degrees of freedom.

There is a multiplicity of ways to organize and categorize these degrees of freedom. We can organize them by "couples," i.e. individual elements in the matrix-representation of the tensor (e.g. Aki and Richards 1980, p. 51), or, alternatively, we can organize them categorically as follows:

- 1 DF defines the magnitude of the moment tensor.
- 2 DF's define the "shape" of the radiation pattern.
- 3 DF's define the orientation in space of the radiation pattern.

The first three DF's listed above are characterizations of the eigenspectrum of the moment tensor. The first DF, magnitude, is proportional to eigenvalues summed in quadrature. The second two locate the moment tensor in a non-euclidean 2-D space with an isotropic and a deviatoric axis, with one possible representation being that of the "fundamental lune" (Tape and Tape, 2012) illustrated in Figure 1.2.

The last three DF's determine the orientation of the eigenvector basis, but have no effect on the eigenvalues.

An alternative formulation has:

- 1 DF defines the isotropic component of the radiation pattern shape.

- 2 DF's define the deviatoric component of the radiation pattern shape. (This subspace can be spanned by selecting one of the basic double-couples as one axis, and the perpendicular axis will be a CLVD.)

- 3 DF's define the orientation in space of the radiation pattern.

In this formulation, the last three DF's are the same as before, but the first three differ. In this case, no single DF establishes the magnitude, but the magnitude can be computed as the quadrature-sum of the three DF's.

In the first formulation, the three shape DF's are isomorphic to a spherical polar coordinate system. In the second formulation, the three shape DF's are isomorphic to a euclidean coordinate system.

The latter isomorphism provides a useful context in which to define the *isotropic angle*. This is a means of characterizing the ratio of energy released by an event whose tensorial representation contains both isotropic (e.g. explosive or implosive) and deviatoric (e.g. an ideal earthquake) components. If the isotropic DF is represented moment value m_{iso} and the two deviatoric DF's are represented by moment values m_{d1} and m_{d2}, then the isotropic angle can be defined by (Bukchin et al., 2001):

$$\tan \theta_{\text{iso}} = \frac{m_{\text{iso}}}{\sqrt{m_{\text{d1}}^2 + m_{\text{d2}}^2}} \tag{1.6}$$

And as regards the former isomorphism, the two DF's representing radiation pattern shape can be selected as the isotropic angle, θ_{iso}, and a deviatoric angle ϕ_{devi} defined in terms of the ratio between m_{d1} and m_{d1}. For a good discussion on the decomposition of moment tensors into isotropic and deviatoric components, see Zhu and Ben-Zion (2013).

In what follows, we explore the classification of various focal mechanisms based on the relationships among the complete set of eigenvalues.

Isotropic moment tensors

Isotropic source disturbances emit elastic energy uniformly in all directions. An ideal explosion, where the elastic wave is initiated by a step function in pressure applied to a spherical cavity, falls into this category. An isotropic moment tensor has three identical eigenvalues. I.e.,

$$\Lambda = (\lambda, \lambda, \lambda) \tag{1.7}$$

Isotropic moment tensors with $\lambda > 0$ can represent idealized explosions, and have $\theta_{\text{iso}} = +90^{\circ}$, in which the forces are uniformly outwards in all directions. If $\lambda < 0$, then the moment tensor represents an idealized implosion, and has $\theta_{\text{iso}} = -90^{\circ}$.

In a Cartesian basis, an isotropic moment tensor will be diagonal, and the *isotropic moment*, m_{iso}, can be defined by the expression:

$$\mathsf{M} = m_{\text{iso}} \sqrt{\frac{2}{3}} \begin{bmatrix} 1 & 0 & 0 \\ 0 & 1 & 0 \\ 0 & 0 & 1 \end{bmatrix} \tag{1.8}$$

in which the moment of a pure isotropic moment tensor is $1/\sqrt{2}$ the Frobenius norm of the moment tensor. This is the same relationship as the moment M_0 of a pure deviatoric moment tensor. Although seismic moment is a concept developed to characterize rupture areas of a faults, eq. 1.8 allows the concept to be generalized for explosion sources as well.

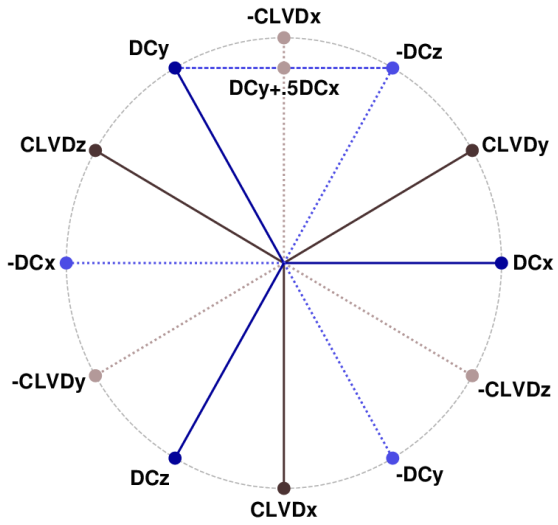

Figure 1.1: The deviatoric plane: Shown here is the traceless 2-D subspace of the 3-D eigenspace of symmetric moment tensors. Plotted around the unit circle are labeled points demarcating prototypical deviatoric focal mechanisms, such that their angular relationship within the space is visible. There are six permutations of the pure double-couple mechanism, which are not physically distinct mechanisms, but rather represent spatial rotations or negations. There are also six permutations of compensated linear-vector dipoles (CLVDs). Because of this permutation symmetry, only a subset of the plane is needed to cover the complete set of physically distinct deviatoric mechanisms. For example, the angular wedge between -CLVDz and CLVDy is such a subset. In the complete 3-D eigenspace, there is also an isotropic axis perpendicular to the plane such that points above the page add an isotropic-outwards (explosive) component, and points below the page add an isotropic-inwards (implosive) component.

Deviatoric moment tensors

Deviatoric source disturbances are those where the source region deforms without a net volume change. A deviatoric moment tensor is a trace-free moment tensor. I.e.,

$$\Lambda = (\lambda_1,\, \lambda_2,\, \lambda_3)\,, \text{where } \lambda_1 + \lambda_2 + \lambda_3 = 0 \tag{1.9}$$

Deviatoric moment tensors form a 2-D subspace, as the trace constraint leaves two DF's free. Shear dislocations, such as shear-motion along a fault, are an important subspace of the broader deviatoric space, and are the prototypical representation of ideal earthquake events. Compensated linear vector dipoles (CLVDs) are another subspace.

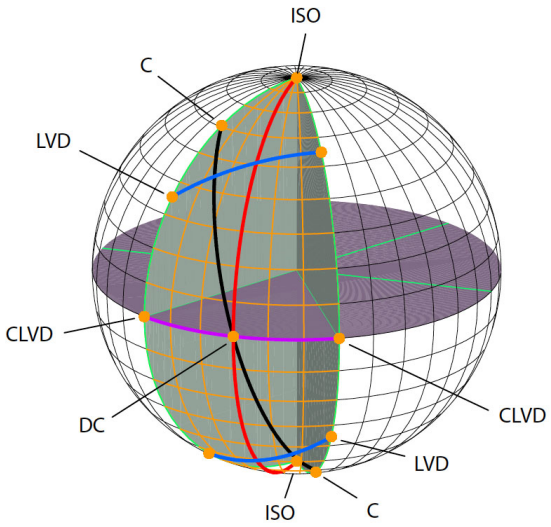

Figure 1.2: The fundamental lune, representing one sextant of the unit sphere, provides a 2-D bounded space in which to map physically distinct moment tensors sources. Only one sixth of the unit sphere is needed, because the remaining sextants represent mere permutations of the coordinate vectors, rather than physically distinct mechanisms. Shown in the horizontal is the deviatoric plane. Focal mechanisms above the plane have an isotropic outward (explosive) component. Mechanisms below the plane have an isotropic inward (implosive) component. *(after Tape and Tape, 2012)*

Double-couples

Double-couples represent shear dislocation events (such as a fault rupture), and therefor represent idealized earthquakes. A double-couple is a deviatoric moment tensor with with two equal-but-opposite eigenvalues and one zero eigenvalue. I.e.,

$$\Lambda = (+\lambda, -\lambda, 0) \tag{1.10}$$

There are three positive-sense permutations of this arrangement (three choices of the zero-eigenvector). The permutations represent 120° rotations in the *deviatoric plane* (the 2-D subspace of deviatoric moment tensors, see figure 1.1). Additionally, there are three negative-sense permutations, representing the negation of the positive-sense permutations, which are staggered 60° from the positive-sense permutations.

A prototypical pure double-couple moment tensor in diagonalized form with mo-

ment M_0 and expressed in a Cartesian basis might look like this:

$$\mathsf{M} = M_0 \begin{bmatrix} 1 & 0 & 0 \\ 0 & -1 & 0 \\ 0 & 0 & 0 \end{bmatrix} \tag{1.11}$$

And here again we see the moment is related to the Frobenius norm of the tensor by a factor of $1/\sqrt{2}$, same as the isotropic case. And as there is no isotropic component, the isotropic angle is $\theta_{\text{iso}} = 0°$. Furthermore, we can establish the convention of assigning the double couple in eq. 1.10 the deviatoric angle $\phi_{\text{devi}} = 0°$. Following this convention, the complete set of double couple mechanisms will have:

$$\phi_{\text{devi}} = n \times 60°, \quad \text{for } n \text{ an integer.} \tag{1.12}$$

CLVD: Compensated linear vector dipoles

Staggered 30° from the double-couples in the deviatoric plane are six CLVD permutations (three positive-sense permutation and their negations). CLVD stands for compensated linear-vector dipole. A CLVD is a deviatoric moment tensor that has two equal eigenvalues, and one eigenvalue that is their summed opposite. I.e.,

$$\Lambda = \left(\lambda, -\frac{1}{2}\lambda, -\frac{1}{2}\lambda\right) \tag{1.13}$$

A CLVD is a linear vector dipole (LVD, defined below) with an isotropic component subtracted out to "compensate," i.e., to make the tensor traceless, the defining property of deviatoric moment tensors. Like double couples, CLVDs have isotropic angle $\theta_{\text{iso}} =$

$0°$. The deviatoric angle is given by:

$$\phi_{\text{devi}} = (2n+1) \times 30°, \quad \text{for } n \text{ an integer.} \tag{1.14}$$

LVD: Linear vector dipoles

LVD stands for linear vector dipole. An LVD has one non-zero eigenvalue, and two zero eigenvalues. I.e.,

$$\Lambda = (\lambda,\, 0,\, 0) \tag{1.15}$$

An LVD can be thought of as the vector sum of a CLVD (a deviatoric component) and an isotropic component. An LVD is neither fully isotropic, nor fully deviatoric. It can be shown that an LVD has an isotropic angle of $\theta_{\text{iso}} \approx 35.26°$, representing a moment ratio of $m_{\text{iso}}/m_{\text{CLVD}} = 1/\sqrt{2}$. As for CLVDs, LVDs have $\phi_{\text{devi}} = (2n+1) \times 30°$, for integer n.

1.2.3 Understanding radiation patterns

Aki and Richards (1980, eq. 4.91, p. 118) give the far-field displacement vectors for P wave and S wave radiation from a moment-tensor source in homogenous media as follows:

$$\boldsymbol{u}^{\text{P}}(\boldsymbol{x}, t) = \left(\frac{\hat{\gamma} \cdot \dot{\mathsf{M}}\left(t - \frac{r}{\alpha}\right) \cdot \hat{\gamma}}{4\pi\rho\alpha^3 r} \right) \hat{\gamma} \tag{1.16}$$

$$\boldsymbol{u}^{\text{SV}}(\boldsymbol{x}, t) = \left(\frac{\hat{p} \cdot \dot{\mathsf{M}}\left(t - \frac{r}{\beta}\right) \cdot \hat{\gamma}}{4\pi\rho\beta^3 r} \right) \hat{p} \tag{1.17}$$

$$\boldsymbol{u}^{\text{SH}}(\boldsymbol{x}, t) = \left(\frac{\hat{\phi} \cdot \dot{\mathsf{M}}\left(t - \frac{r}{\beta}\right) \cdot \hat{\gamma}}{4\pi\rho\beta^3 r} \right) \hat{\phi} \tag{1.18}$$

The P wavefield is described by $\boldsymbol{u}^{\mathrm{P}}$, and two fields, $\boldsymbol{u}^{\mathrm{SV}}$ and $\boldsymbol{u}^{\mathrm{SH}}$, separately describe the vertical and horizontal component of the transversely polarized S wave displacement field. M is the moment tensor, and $\dot{\mathsf{M}}$ is its time derivative, evaluated at the retarded time $\left(t - \frac{r}{\alpha}\right)$ for P waves or $\left(t - \frac{r}{\beta}\right)$ for S waves. The material properties ρ, α, and β are mass density, P velocity, and S velocity, respectively. The unit vectors define the outward longitudinal direction ($\hat{\gamma}$), the vertical transverse direction ($\hat{p}$), and the horizontal transverse direction ($\hat{\phi}$), and correspond, in homogenous media, to the traditional $\hat{r}$, $\hat{\theta}$, $\hat{\phi}$ unit vectors in a right-hand spherical polar coordinate system in which the positive z axis is taken to point downwards, and the x axis is conventionally chosen to point northwards (such that the azimuthal coordinate increases eastward from north).

From these equations we can see the directional dependence of the P and S radiation patterns. Energy radiance, necessary for computing the directional probability of phonon emission in the radiative transport method, is proportional to the square of the numerator in each equation.

For double-couple moment tensors, which represent ideal fault-motion earthquakes, the result is a four-lobed P-wave radiation pattern interleaved with a four-lobed S-wave radiation pattern. The four lobes alternate polarity, such that the point maxima of outward first motions in the P pattern coincides with a principle axis of the moment tensor called the *pressure axis* (corresponding to the positive eigenvalue), and the maxima of inward first motions coincides with a perpendicular principle axis called the *tension axis* (corresponding to the negative eigenvalue). There is a third principle axis along which no displacements propagate, corresponding to the zero eigenvalue, and thus we can refer to it as a *null axis*. Looked at in the plane of the pressure and tension principle axes, the P and S radiation patterns are illustrated in Figure 1.3.

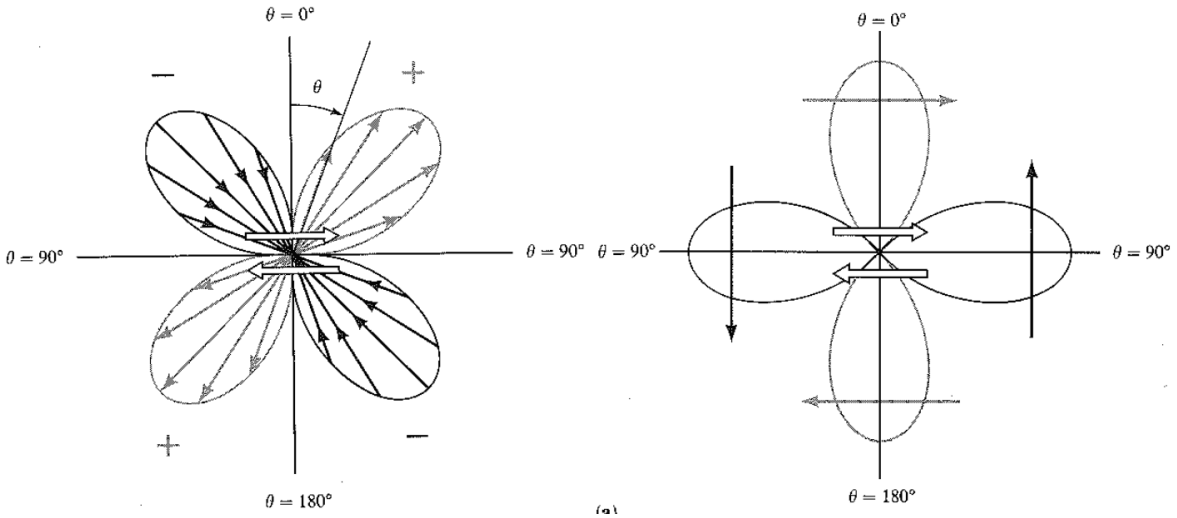

Figure 1.3: The P wave radiation pattern (left) and the S wave radiation pattern (right). Both have a four-lobed distribution, with lobes alternating in polarity. Solid arrows indicate direction of particle motion. Fault motion is indicated by block-outline arrows on both plots. *(after Aki and Richards, 1980, figures 4.5 and 4.6)*

A common way to display earthquake focal mechanisms is with *beach ball* plots. A beach ball plot illustrates the radiation pattern by mapping the zones of outward and inward P-wave polarities on a projection of the unit sphere. Conventionally, a beach ball plot is a stereographic projection of the lower hemisphere surrounding a moment tensor point source, viewed from above, looking down. Shaded regions indicate outward first motions, and unshaded regions indicate inward first motions. A beach ball plot does not indicate S-wave polarities. To supplement beach ball plots, we have developed for our work a way of illustrating both P and S motions of a source by color coding wave type and polarizations on a similar stereographic projection of the lower half sphere. Traditional beach ball plots, as well as an example of our polarization map plot, are shown in figure 1.4. Interpretation of polarization maps is explained in Figure 1.5.

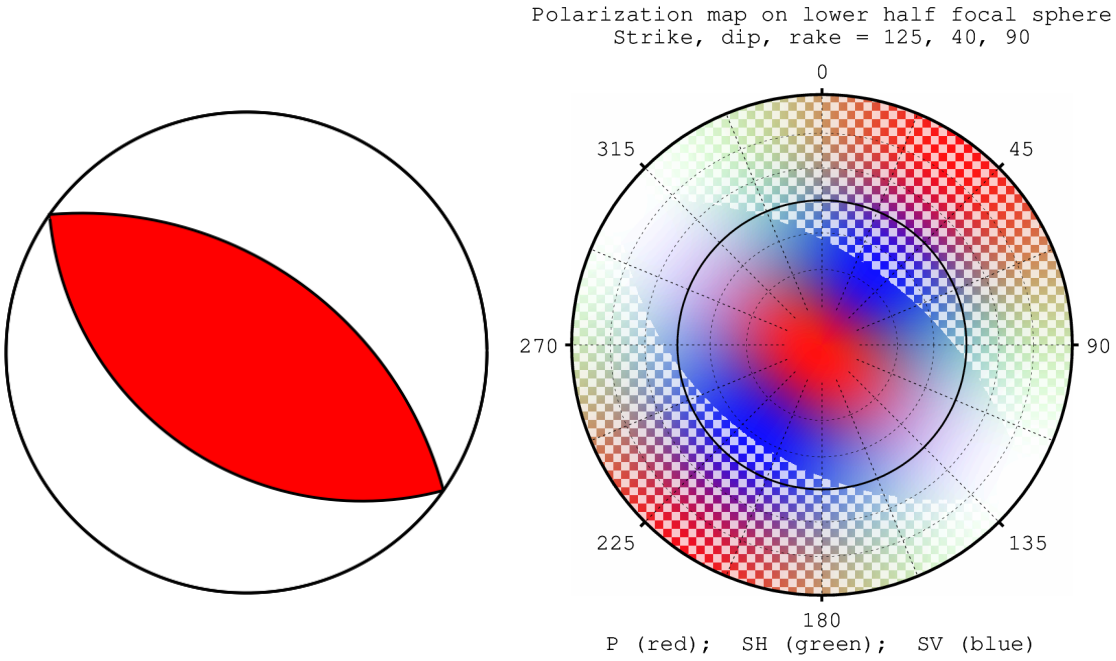

Figure 1.4: Example beach ball plot and corresponding polarization map. Interpretation of polarization maps is explained in Figure 1.5.

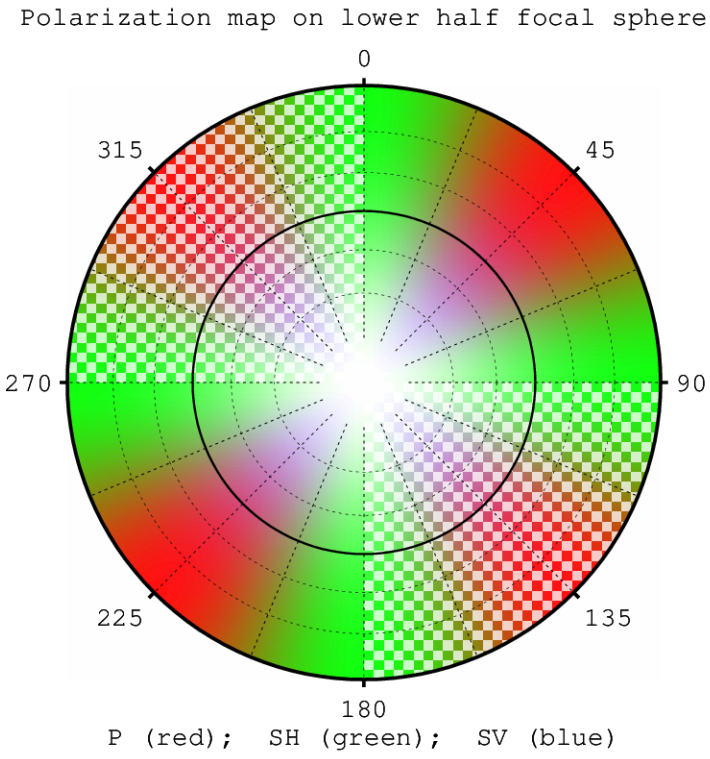

Figure 1.5: Polarization map of a strike-slip earthquake focal mechanism imaged on a stereographic projection of the interior of the lower half focal sphere. Color density indicates directional dependence of radiated energy by polarization mode, with red indicating longitudinally polarized P energy, green representing horizontally polarized S energy, and blue indicating vertically polarized S energy. Here the compressional principal axis is at 45° (or alternately 225°) azimuth, and the tensional principal axis is at 135° (or 315°) azimuth. The null axis is directed into the page. The checkerboard mask indicates the tensional region, or the region where the P amplitude is negative. Observe that there are azimuths that completely isolate S polarized energy (the green SH lobes), but that no azimuths completely isolate P energy, due to the presence of some SV energy near the poles. The double-couple mechanism shown here has a strike of 0°, dip of 90° and rake of 0°.

Chapter 2

Radiative Transport

2.1 Theory

There is a rich mathematical formalism devoted to the ray theoretical approach to solving wavefront propagation problems. The author here will predominantly direct the reader to two works, Aki and Richards (1980), and Červenỳ (2001), rather than reproduce or summarize their works here. A few key takeaway points, however, are presented in the following subsections for easy reference. Radiative transport extends ray theory in that it solves for the transport of energy through elastic structures. Ray theory contributes the geometrical component of this. Also important in energy transport solutions is scattering by small-scale structure too intricate to attempt via ray theory. For this, there is a statistical treatment covered in detail in Sato, Fehler, and Maeda (2012). A summary of important concepts from that work, relevant to this thesis, are presented in subsection 2.1.6.

2.1.1 Ray theory

Ray theory is a means of solving elastic wave problems by considering rays rather than wave dynamics. A *ray* is an abstraction of the propagation direction of a wavefront and

allows approximate solutions to the wavefield to be found that become more accurate as frequency approaches infinity, or equivalently, as the ratio of the wavelength of the wavefield to the scale length of the medium in which it propagates approaches zero. The *scale length* in this context characterizes how sharply the wave velocity in a medium varies over distance and is defined as the ratio of the wave velocity in the medium to the spatial gradient of that velocity. More rigorously, rays are defined in terms of energy flux. In a propagating wavefront, an elastic energy flux vector S_i can be expressed as a product of the stress field τ_{ij} and the particle velocity field $\dot{u}_j$ as

$$S_i = -\tau_{ij}\dot{u}_j \tag{2.1}$$

This vector identifies the direction of energy transport at each point in the wave field. A *ray* can be defined as a path through the medium whose tangent at each point along the path is determined by the energy flux vector. Thus rays define paths of energy transport through the medium. A velocity of energy transport, called the *group velocity*, can be computed by dividing the time-averaged energy flux by the time averaged elastic energy density, averaging over a natural time period such as one period of oscillation. The group velocity is given by:

$$\mathcal{U}_i = \bar{S}_i/\bar{E} \tag{2.2}$$

where $\mathcal{U}_i$ represents group velocity, and the bar over top of $\bar{S}_i$ and $\bar{E}$ indicates average over a temporal period. For a transient signal, with no natural time period, but a finite duration, the time-averaged ratio of S_i to E may be replaced by a time-integrated ratio:

$$\mathcal{U}_i = \hat{S}_i/\hat{E} \tag{2.3}$$

where the hat represents time integration over a time window large enough to contain the signal. This allows the definition to be useful for short impulsive signals such as

might arise from an earthquake or explosion event. In the above, the elastic energy density E is composed of a kinetic and potential part (owing to strain energy), and is given by

$$E = \tfrac{1}{2} c_{ijkl} e_{ij} e_{kl} + \tfrac{1}{2} \rho \dot{u}_i \dot{u}_i \tag{2.4}$$

with e_{ij} and c_{ijkl} referring to the elastic strain and elastic stiffness tensors, respectively.

By understanding the path along which energy is transported, and the velocity of that transport at any point along the path, it is possible to construct a parametric representation of the transport of a finite quanta of that energy, which we might call a *phonon*, as a function of time. This transport of phonons is a key component of the technique called *radiative transport*, which will be further explicated below.

The full elastic wave equation can be very difficult to solve in the general case. However, in certain simple geometries and elastic regimes the solutions may be quite simple and yield useful geometric ray solutions. In other geometries or elastic regimes, the solutions may simplify nicely to a high degree of approximation. For example, in non-dispersive, linear isotropic media, where the bulk and shear moduli are spatially uniform, plane wave solutions divide cleanly into P waves, polarized longitudinally, and S waves, polarized transversely. The P and S waves have distinct phase velocities α and β, respectively, which are also identical to the group velocities of the respective waves. This allows phonons for P and S wave modes to be treated as distinct and independent entities with readily-computable ray trajectories. In anisotropic media, the solutions divide into three wave modes, one called quasi-P (qP), and two distinct quasi-S (qS1 and qS2) modes. However the wave modes are not completely independent, and may interact with each other, although treating them as independent wave modes may still be a useful approximation. A similar interaction between P and S modes can occur in isotropic but strongly spatially varying media, complicating solutions, but this interaction is generally small and may be ignorable to an acceptable

degree of approximation. Additionally, an attenuating medium (where energy in the wavefront can be lost to thermal heating of the background medium) will include some dispersion, which can distort pulse shapes or cause ray paths to separate based on frequency component. However, in narrow frequency bands and at sufficiently moderate levels of intrinsic attenuation, these effects are small and can often be ignored.

In summary, ray theory generally concerns itself with two main aspects of approximate solutions to the full wave equation: (1) the pathways along which energy flows, called rays, and (2) the amplitudes of the wave at each point along the path. Computing the amplitudes along rays in a non-attenuating medium is a matter of considering how the energy spreads out due to the geometric aspects of the wavefront. (For example, a spherical wavefront in a homogenous medium results in an inverse r-squared law in energy, and correspondingly an inverse-r law in amplitude.) This geometric determinism of the amplitudes is referred to as *geometric spreading*. In an attenuating medium, there is also a decay of amplitude with travel time along the trajectory of the ray, which can be readily computed. The technique of radiative transport borrows from ray theory the computation of ray path trajectories, and may consider also the amplitude effects due to intrinsic attenuation. However the effects of geometric spreading, while an important component of ray theory generally, are of less importance to the radiative transport technique, as it is replaced by a Monte Carlo counting of phonons reaching a destination, which will be further explained below.

Ray path geometries

For the purposes of this dissertation, which seeks ultimately to explain a particular implementation of the radiative transport technique, two ray geometry results are relevant:

1. Rays follow straight-line paths in spatially uniform, linearly elastic isotropic

media. The velocity of propagation is independent of location or direction, but does depend on wave mode (P or S).

2. Ray paths are circular arc segments in linear elastic isotropic media whose elastic velocities (α and β for P, S waves, respectively) are first-order linearly varying (constant gradient) functions of space. Velocity of propagation is a function of position but is not a function of direction.

2.1.2 Radiative transport

Radiative transport seeks to find solutions to elastic problems by looking at energy transport through an Earth model. "Solutions" here does not necessarily refer to a full elastic solution, such as "what is the stress-strain state of the medium at all points in the elastic model at a given time," but is usually a more limited question, such as "what energy signal is recorded at the surface of the model in the vicinity of a hypothesized virtual seismometer," or "what is the approximate volumetric energy distribution throughout the model at a particular time t." The phrase "energy signal" in the preceding could, for example, refer to a synthetic seismic envelope, giving information about the amplitude of ground motion as a function of time, but neglecting phase information. Or, it could refer to a full-waveform synthetic seismogram, inclusive of phase information, if sufficient care is taken to track this information through the simulation.

The general strategy of radiative transport is one of *phonon spraying*, which is to say that phonons carrying an initial energy quantity and assigned an initial wave mode (P or S) are considered to have originated from a source and are assigned an initial travel direction, chosen randomly from an angular probability distribution which mimics the angular distribution of energy output from a hypothesized source mechanism, and as such may represent an earthquake, explosion, or other seismic event. The paths

these phonons take are then computed via ray-theory, and tracked until such time as the phonons reach a neighborhood in the model where an energy or ground-motion signal is desired, and the relevant information of that phonon is binned into a digitized signal which will become, after a sufficient number of phonons are simulated, a good synthetic representation of an envelope or waveform signal.

Because energy captured is a function of the number of phonons reaching a destination and the path-attenuated energy that they carry, all of the amplitude affects of geometric spreading are computed implicitly, and ray-theory based geometric amplitude results do not need to be explicitly computed. The only information needed from ray theory is how to compute the ray paths.

The final element of radiative transport is that so-called non-deterministic affects may also be considered. This, for example, might include scattering from small-scale spatially random perturbations to the velocity model of the medium, such as might occur in heterogeneous media. This can be handled by a pseudo-random process of interrupting a raypath at random intervals and reorienting its continued progress. This can be a good model of Earth-like scattering if an appropriate characterization of the directionality and frequency of scattering can be arrived at. Such a characterization is discussed in section 2.1.6.

2.1.3 Reflection and transmission at interfaces

In any realistic Earth model, the parameters characterizing the elastic media will be functions of position. In our implementation we take a cellular approach to constructing laterally and depth varying models. This means that the models we consider are composed of adjoining volumetric cells of simple geometry in which a single set of parameters characterize the media in a way suitable for calculating paths within the cell. When a phonon travels from one cell to another cell, it is possible for there to

be a discontinuity in those material parameters. This arrangement could be used to model a sharp interface in the Earth's structure, such as occurs at the Mohorovičić discontinuity. These discontinuities can produce reflections, refractions, diffractions, and conversions between P and S polarization modes in the propagating wave. In the ray method, diffraction is generally ignored, but the remaining effects can be treated by the following formalism.

Both Aki and Richards (1980), and Červenỳ (2001), as well as other sources, contain thorough formal development of reflection and transmission of rays. Here we will prefer the formalism of Cerveny, and present a summary of the important results.

The formalism of Cerveny presents ray amplitudes in a ray-centered coordinate system denoted by a superscript (q) on amplitude vectors. For example, the particle displacement vector $u(\boldsymbol{x}, t)$ is written as:

$$u^{(q)}(\boldsymbol{x}, t) = \boldsymbol{U}^{(q)}(\boldsymbol{x}) F\left(t - T(\boldsymbol{x})\right) \tag{2.5}$$

In the ray-centered coordinate system, three position-dependent unit vectors, $\boldsymbol{e}_i^{(q)}$, define the meaning of the elements of the amplitude vectors. Unit vector $\boldsymbol{e}_3^{(q)}$ is chosen identical to the ray tangent (i.e., points in the direction of ray propagation), and thus defines the P polarization direction. Unit vectors $\boldsymbol{e}_1^{(q)}$ and $\boldsymbol{e}_2^{(q)}$ are transverse to this, and serve to define the S polarization directions. When considering reflection and transmission from a planar sharp interface, unit vector $\boldsymbol{e}_1^{(q)}$ can be chosen to be in the incidence plane, and thus serves to define vertical polarization with respect to the interface. Unit vector $\boldsymbol{e}_2^{(q)} = \boldsymbol{e}_3^{(q)} \times \boldsymbol{e}_1^{(q)}$ then serves to define horizontal polarization. Thus,

amplitude vectors for P and S waves, respectively, can be written as:

$$\boldsymbol{U}_{\mathrm{P}}^{(q)} = \begin{bmatrix} 0 \\ 0 \\ A \end{bmatrix}; \qquad \boldsymbol{U}_{\mathrm{S}}^{(q)} = \begin{bmatrix} B \\ C \\ 0 \end{bmatrix} \tag{2.6}$$

where A is the P wave amplitude, and B and C denote the SV and SH components of the S wave amplitudes.

The utility of this representation is that it lends itself to a convenient formalism for reflection and transmission where matrix operators can be constructed that give the outgoing amplitudes for reflected and transmitted waves in terms of an incident wave. Thus, the vector $\boldsymbol{U}^{(q)\mathrm{R}}$ gives the amplitudes of all three possible reflected modes in terms of the incident amplitude vector $\boldsymbol{U}^{(q)\mathrm{I}}$ according to:

$$U_k^{\mathrm{R}} = R_{ik}^{\mathrm{R}} U_i^{\mathrm{I}} \tag{2.7}$$

where the (q) basis specifier is taken as implicit, and superscripts R and I refer to reflected and incident. Likewise, the amplitudes of all three possible transmitted modes, denoted by superscript T, are given by:

$$U_k^{\mathrm{T}} = R_{ik}^{\mathrm{T}} U_i^{\mathrm{I}} \tag{2.8}$$

The reflection and transmission matrices, $\mathbf{R}^{\mathrm{R}}$ and $\mathbf{R}^{\mathrm{T}}$, each have the following arrangement when expressed in the ray-centered basis:

$$\mathbf{R} = \begin{bmatrix} R_{11} & 0 & R_{13} \\ 0 & R_{22} & 0 \\ R_{31} & 0 & R_{33} \end{bmatrix} \tag{2.9}$$

and the elements R_{ik} indicate the amplitude ratios of output mode k to input mode i. Thus for a unit amplitude incident P wave, R_{33} and R_{31} give the amplitudes of the outgoing P and SV wave, respectively. Likewise, for an incident SV wave, R_{13} and R_{11} give the relative amplitudes of the outgoing P and SV waves. For an incident SH wave, the outgoing amplitude, relative to the incident amplitude, is given by R_{22}. Note that because the SH mode does not excite motion in the incidence plane, that there is no interaction with the P and SV modes, and thus $R_{12} = R_{21} = R_{23} = R_{32} = 0$. Note also the order of indices in eqs. 2.7 and 2.8. This reflects the fact that our preference for using the first index for the incident ray mode necessitates that we multiply the incident amplitude vector by the transpose of the matrix $\mathbf{R}$ in order to compute the outgoing ray amplitudes.

The $\mathbf{R}^{\mathrm{R}}$ and $\mathbf{R}^{\mathrm{T}}$ matrices give the relative amplitudes of the reflected and transmitted waves, and are referred to as *displacement coefficient matrices* for reflection and transmission. However, for radiative transport, the quantity of interest for reflection/-transmission handling is not the amplitudes, but rather the flux of energy that goes into each outgoing wave. This is because in radiative transport we are tracking the progress of phonons representing finite quanta of energy. Thus the partition of that energy into the various outgoing waves is the quantity of interest. In our particular implementation, for every phonon entering an interface, we simulate only one phonon exiting, and thus we use the energy of each mode to establish the weighted probabilities of each outgoing possibility. In this way, a large number of phonons striking the interface will apportion themselves appropriately among the outgoing rays.

Another set of matrices, denoted $\mathcal{R}^{\mathrm{R}}$ and $\mathcal{R}^{\mathrm{T}}$ for reflection and transmission, respectively, and referred to as the *normalized reflection and transmission displacement coefficient matrices*, enable us to compute ratios of energy flux between the incident and outgoing waves. They are, of course, related to $\mathbf{R}^{\mathrm{R}}$ and $\mathbf{R}^{\mathrm{T}}$. The energy flux relationship is given

in terms of the energy flux crossing the interface, and is denoted $S_i n_i$, where $\boldsymbol{n}$ is a unit vector normal to the interface. As energy is proportional to the square of amplitude, we expect the relationship to be second order in $\mathcal{R}$. And indeed, for a particular conversion channel $m \to n$, where $n, m \in \{1, 2, 3\}$ and represent the incident and outgoing wave modes, respectively, the relationship is given by:

$$\left| S_i^{(n)} n_i \right| = \mathcal{R}_{mn} \mathcal{R}_{mn}^* \left| S_i^{(m)} n_i \right| \tag{2.10}$$

Here indices m and n are free and are not summed over. The relationship represents a single incident to outgoing channel. The necessity of the absolute values, and the complex-conjugate multiplication of $\mathcal{R}$ is a result of the fact that the $\mathcal{R}$ matrices still retain the same phase information as the $\mathbf{R}$ matrices. It is the moduli that are the relevant quantity when computing energy fluxes.

If we "vectorize" the incident energy flux crossing the interface by polarization mode in the same way that we did for the displacement amplitudes (eq. 2.6), we get:

$$\boldsymbol{E}_{\mathrm{P}}^{(q)} = \begin{bmatrix} 0 \\ 0 \\ \varepsilon_{\mathrm{P}} \end{bmatrix}; \qquad \boldsymbol{E}_{\mathrm{S}}^{(q)} = \begin{bmatrix} \varepsilon_{\mathrm{SV}} \\ \varepsilon_{\mathrm{SH}} \\ 0 \end{bmatrix} \tag{2.11}$$

for incident P and S waves, respectively. (Here the superscript (q) denotes only that we are separating energy by the wave mode that carries it and is not meant to suggest that scalar energy is a vector quantity.) And with the incident and outgoing energy fluxes thus indexed, we can write the outgoing reflected and transmitted energies in terms

of energy flux matrices $\mathbf{\Phi}^{\mathrm{R}}$ and $\mathbf{\Phi}^{\mathrm{T}}$ as:

$$E_n^{\mathrm{R}} = \Phi_{mn}^{\mathrm{R}} E_m^{\mathrm{I}} \tag{2.12}$$

$$E_n^{\mathrm{T}} = \Phi_{mn}^{\mathrm{T}} E_m^{\mathrm{I}} \tag{2.13}$$

where the elements of the $\mathbf{\Phi}$ matrix (for the reflection or transmission case) can be given in terms of the (corresponding) $\mathcal{R}$ elements according to:

$$\Phi_{mn} = \begin{bmatrix} \mathcal{R}_{11}\mathcal{R}_{11}^* & 0 & \mathcal{R}_{13}\mathcal{R}_{13}^* \\ 0 & \mathcal{R}_{22}\mathcal{R}_{22}^* & 0 \\ \mathcal{R}_{31}\mathcal{R}_{31}^* & 0 & \mathcal{R}_{33}\mathcal{R}_{33}^* \end{bmatrix} \tag{2.14}$$

Eqs. 2.12 and 2.13 are for energy flux rate, or a position-dependent density of energy crossing the interface per unit time. However, for radiative transport, as we have implemented it, we consider a phonon representing a finite energy quantity in a finite (though unspecified) volume of space, which will cross the interface in a finite (but again unspecified) interval of time. Thus we are not dealing with flux rates, but rather quanta of energy which we know cross the interface, but we do not know according to what time profile they do so. It is not a problem, however, as the rate at which energy is deposited into the outgoing ray products is always proportional to the rate at which energy is deposited into the interface by the incident phonon, no matter the time function over which that deposit occurs. Thus any conclusion we may draw from the analysis of flux rates must also apply to the total energy quantities, and our formulation is therefore appropriate for the phonon metaphor.

As a final note, before we list out the formulas for the $\mathbf{R}$ and $\mathcal{R}$ matrices for reflection and transmission, we point out that energy conservation requires that the summation of reflected and transmitted energies must sum to the incident energy. Or, in other

words:

$$\sum_{n=1,2,3} E_n^{\mathrm{R}} + \sum_{n=1,2,3} E_n^{\mathrm{T}} = \sum_{m=1,2,3} E_m^{\mathrm{I}} \tag{2.15}$$

and careful inspection of the coefficient values should reveal that this relationship holds.

2.1.3.1 Coefficients enumerated

The normalized displacement reflection and transmission coefficients (the $\mathcal{R}$ matrix elements), necessary for computing energy flux matrix $\mathbf{\Phi}$ (eq. 2.14) are presented here. They are reproduced from Červenỳ (2001), section 5.3.3. The parameter ϵ, which appears in the off-diagonal coefficients, is discussed in Cerveny's section 5.3.2, defined in Cerveny's eq. 5.3.1, and illustrated in Cerveny's figure 5.9. If one is careful to choose polarization vector orientation in a consistent way and in accordance with subfigure (a) of Cerveny's figure 5.9, then one can simply take $\epsilon = 1$. For an explanation of when $\epsilon = -1$ might be appropriate or convenient, the reader should consult the aforementioned sections and figures.

The non-normalized displacement coefficients (the $\mathbf{R}$ matrix elements) are presented in Červenỳ (2001), section 5.3.1, but are not reproduced here. Conceptually, the non-normalized coefficients are important to understanding the normalized coefficients, but since the normalized coefficients (the $\mathcal{R}$ matrix elements) have closed-form expression, it will suffice to refer the reader to Cerveny if he or she desires to see the formulation of the non-normalized coefficients. These coefficients will again be important in understanding the *conversion coefficients*, represented as a matrix $\mathcal{D}$, and which will be discussed in the next subsection of this work, but these coefficients will again have closed-form expression and so the elements of $\mathbf{R}$ remain unnecessary to our present goals.

Normalized displacement reflection coefficients

$$\mathcal{R}^{\mathrm{R}}_{11} = D^{-1}\left[q^2p^2P_1P_2P_3P_4 + \rho_1\rho_2\left(\alpha_1\beta_2P_2P_3 - \alpha_2\beta_1P_1P_4\right)\right.$$
$$\left. - \alpha_1\beta_1P_3P_4Y^2 + \alpha_2\beta_2P_1P_2X^2 - \alpha_1\alpha_2\beta_1\beta_2p^2Z^2\right] \tag{2.16}$$

$$\mathcal{R}^{\mathrm{R}}_{22} = \bar{D}^{-1}\left(\rho_1\beta_1P_2 - \rho_2\beta_2P_4\right) \tag{2.17}$$

$$\mathcal{R}^{\mathrm{R}}_{33} = D^{-1}\left[q^2p^2P_1P_2P_3P_4 + \rho_1\rho_2(\alpha_2\beta_1P_1P_4 - \alpha_1\beta_2P_2P_3)\right.$$
$$\left. - \alpha_1\beta_1P_3P_4Y^2 + \alpha_2\beta_2P_1P_2X^2 - \alpha_1\alpha_2\beta_1\beta_2p^2Z^2\right] \tag{2.18}$$

$$\mathcal{R}^{\mathrm{R}}_{13} = -2\epsilon p\left(\beta_1\alpha_1P_1P_2\right)^{1/2}D^{-1}\left(qP_3P_4Y + \beta_2\alpha_2XZ\right) \tag{2.19}$$

$$\mathcal{R}^{\mathrm{R}}_{31} = -\mathcal{R}_{13} \tag{2.20}$$

Normalized displacement transmission coefficients

$$\mathcal{R}^{\mathrm{T}}_{11} = 2\left(\beta_1\beta_2\rho_1\rho_2P_2P_4\right)^{1/2}D^{-1}\left(\alpha_1P_3Y + \alpha_2P_1X\right) \tag{2.21}$$

$$\mathcal{R}^{\mathrm{T}}_{22} = 2\left(\beta_1\beta_2\rho_1\rho_2P_2P_4\right)^{1/2}\bar{D}^{-1} \tag{2.22}$$

$$\mathcal{R}^{\mathrm{T}}_{33} = 2\left(\alpha_1\alpha_2\rho_1\rho_2P_1P_3\right)^{1/2}D^{-1}\left(\beta_2P_2X + \beta_1P_4Y\right) \tag{2.23}$$

$$\mathcal{R}^{\mathrm{T}}_{13} = 2\epsilon p\left(\beta_1\alpha_2\rho_1\rho_2P_2P_3\right)^{1/2}D^{-1}\left(qP_1P_4 - \alpha_1\beta_2Z\right) \tag{2.24}$$

$$\mathcal{R}^{\mathrm{T}}_{31} = -2\epsilon p\left(\alpha_1\beta_2\rho_1\rho_2P_1P_4\right)^{1/2}D^{-1}\left(qP_2P_3 - \beta_1\alpha_2Z\right) \tag{2.25}$$

Symbols used

In the above coefficients, p is the horizontal slowness of the incident ray, α, β, and ρ are the P-wave velocity, S-wave velocity, and density of the medium on either the incident side (subscript 1) or transmission side (subscript 2), and the remaining symbols are given as:

$$q = 2\left(\rho_2\beta_2^2 - \rho_1\beta_1^2\right) \tag{2.26}$$

$$X = \rho_2 - qp^2 \tag{2.27}$$

$$Y = \rho_1 + qp^2 \tag{2.28}$$

$$Z = \rho_2 - \rho_1 - qp^2 \tag{2.29}$$

$$P_1 = \left(1 - \alpha_1^2 p^2\right)^{1/2} \tag{2.30}$$

$$P_2 = \left(1 - \beta_1^2 p^2\right)^{1/2} \tag{2.31}$$

$$P_3 = \left(1 - \alpha_2^2 p^2\right)^{1/2} \tag{2.32}$$

$$P_4 = \left(1 - \beta_2^2 p^2\right)^{1/2} \tag{2.33}$$

$$\begin{aligned} D = {} & q^2 p^2 P_1 P_2 P_3 P_4 + \rho_1\rho_2\left(\beta_1\alpha_2 P_1 P_4 + \alpha_1\beta_2 P_2 P_3\right) \\ & + \alpha_1\beta_1 P_3 P_4 Y^2 + \alpha_2\beta_2 P_1 P_2 X^2 + \alpha_1\alpha_2\beta_1\beta_2 p^2 Z^2 \end{aligned} \tag{2.34}$$

$$\bar{D} = \rho_1\beta_1 P_2 + \rho_2\beta_2 P_4 \tag{2.35}$$

Note that the symbols $P_{i\in\{1,2,3,4\}}$ are the cosines of the angles of reflected and transmitted P and S waves, respectively. Should the outgoing rays go post-critical, the quantities under the square roots in the P expressions become negative, and we follow the convention of taking the positive root such that the P parameters become positive-imaginary in this case.

2.1.4 Components of motion at interfaces

Although energy flux rates are the determining factor for reflection and transmission, allowing us to compute how the energy of an incident phonon will partition across the resultant reflected and transmitted rays, and we have stipulated that the displacement amplitudes of the resultant rays are unimportant in that computation, the displace-

ment amplitudes nevertheless become important if we suppose a hypothetical seismic receiver embedded in the interface (which may be the free surface or an at-depth interface). In this case, ground motion is the vector sum of all waves present on either side of the interface (either the reflected side or the transmitted side). In fact, we can equivalently determine ground motion by by summing the transmitted P and S waves, *or* by summing the incident wave and reflected P and S waves.

In working with the incident and resultant rays, we have used ray-centered vector bases, denoted by superscript (q) and basis vectors $\boldsymbol{e}_i$, which are different for each resultant ray. In order to get ground motion, however, we will desire a single basis in which to express the net ground motion resulting from the summation of the contributing rays. We will choose a local basis set, oriented with respect to the interface plane at the point of reflection/transmission. We denote these basis vectors $\boldsymbol{i}_i$, and we choose $\boldsymbol{i}_3$ perpendicular to the interface plane, $\boldsymbol{i}_2$ perpendicular to the plane of incidence and in the same direction as the SH-aligned $\boldsymbol{e}_2$ vector common to all the ray-centered bases, and the last one, $\boldsymbol{i}_1$ is taken mutually perpendicular to both. This basis is illustrated in Figure 2.1. We will denote vectors expressed in this basis with a superscript (z), and we can construct change-of-basis matrices $\mathbf{C}^{\{\mathrm{I,rP,rS,tP,tS}\}}$ to take you from the (q) basis for each of the five possible ray-centered bases to the local (z) basis, as follows:

$$\boldsymbol{U}^{(z)} = \mathbf{C}\boldsymbol{U}^{(q)} \tag{2.36}$$

where $\mathbf{C}$ is composed of the $\boldsymbol{e}_i$ basis vectors expressed in the (z) basis, or

$$\mathbf{C} = \left[\boldsymbol{e}_1^{(z)\mathrm{tS}}, \boldsymbol{e}_2^{(z)\mathrm{tS}}, \boldsymbol{e}_3^{(z)\mathrm{tP}}\right] \tag{2.37}$$

or, expressed in index notation:

$$C_{ij} = \boldsymbol{i}_i \cdot \boldsymbol{e}_j \tag{2.38}$$

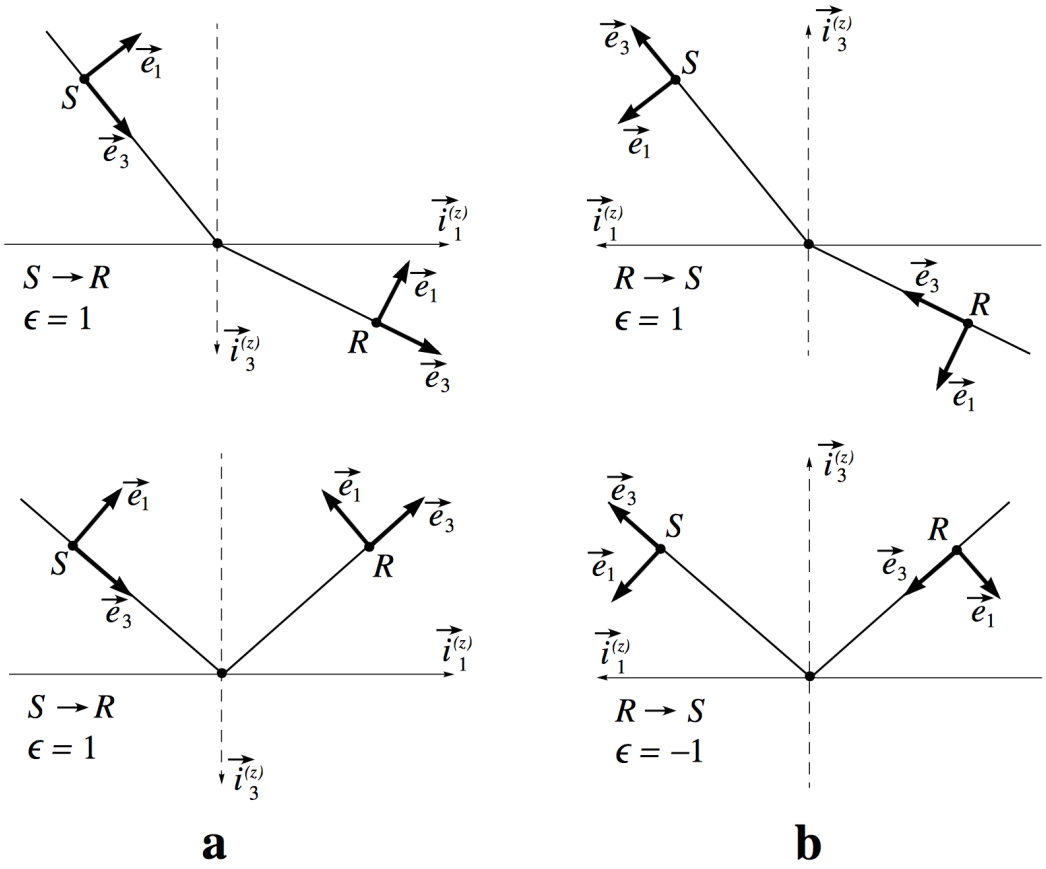

Figure 2.1: Choice of basis vector $\boldsymbol{e}_i$ in the forward (a) and backward (b) propagation along ray Ω., after Červeny̌ (2001) Figure 5.9. In the backward propagation, $\boldsymbol{e}_1$ and $\boldsymbol{e}_3$ are chosen in the opposite directions than in the forward propagation. The local Cartesian coordinate systems at the points of incidence on structural interfaces are also changed as follows: $\boldsymbol{i}_1^{(z)}$ and $\boldsymbol{i}_3^{(z)}$ are chosen in the opposite directions than in the forward propagation. Unit vectors $\boldsymbol{e}_2$ and $\boldsymbol{i}_2^{(z)}$ remain the same in both cases. In the present chapter, we consider only forward propagation, but retain the ϵ parameter, defined as $\epsilon = \operatorname{sgn}(\boldsymbol{e}_3 \cdot \boldsymbol{i}_3)$ where $\boldsymbol{e}_3$ is for the incident ray, so that our results remain general.

For example, the matrix $\mathbf{C}^{\mathrm{tP}}$, for converting from the $\boldsymbol{e}_i$ basis for transmitted P to the local $\boldsymbol{i}_i$ basis, can be expressed via Snell's law in terms of the ray parameter p, the velocities α and β, and the cosine parameters $P_{n\in\{1,2,3,4\}}$ as:

$$\mathbf{C}^{\mathrm{tP}} = \begin{bmatrix} \epsilon P_3 & 0 & \alpha_2 p \\ 0 & 1 & 0 \\ -\alpha_2 p & 0 & \epsilon P_3 \end{bmatrix} \tag{2.39}$$

And likewise, $\mathbf{C}^{\mathrm{tS}}$ is:

$$\mathbf{C}^{\mathrm{tS}} = \begin{bmatrix} \epsilon P_4 & 0 & \beta_2 p \\ 0 & 1 & 0 \\ -\beta_2 p & 0 & \epsilon P_4 \end{bmatrix} \tag{2.40}$$

After combining elements from $\mathbf{C}^{\mathrm{tP}}$ and $\mathbf{C}^{\mathrm{tS}}$ according to the form suggested by eq. 2.37, we get:

$$\mathbf{C} = \begin{bmatrix} \epsilon P_4 & 0 & \alpha_2 p \\ 0 & 1 & 0 \\ -\beta_2 p & 0 & \epsilon P_3 \end{bmatrix} \tag{2.41}$$

Thus, using the displacement coefficient matrix for transmission, R_{jk}, and the conversion matrix C_{ij}, we can get the local basis ground motion amplitude vector $U_i^{(z)}$ in terms of the incident ray amplitude vector $U_k^{(q)}$, and in the process define the *conversion coefficient matrix*, which we will denote by $\mathcal{D}_{ik}$ as:

$$U_i^{(z)} = C_{ij} R_{kj}^{\mathrm{T}} U_k^{(q)} \equiv \mathcal{D}_{ik} U_k^{(q)} \tag{2.42}$$

Now, by inspection of the structure of the $\mathbf{C}$ and $\mathbf{R}$ matrices, we can see that, by considering the amplitudes on the transmission side of the interface, we can compute

the $\mathcal{D}_{ik}$ elements as:

$$\mathcal{D}_{11} = \epsilon P_4 R_{11} + \alpha_2 p R_{13} \qquad (\text{SV} \rightarrow \boldsymbol{i}_1) \tag{2.43}$$

$$\mathcal{D}_{13} = \epsilon P_4 R_{31} + \alpha_2 p R_{33} \qquad (\text{P} \rightarrow \boldsymbol{i}_1) \tag{2.44}$$

$$\mathcal{D}_{22} = R_{22} \qquad (\text{SH} \rightarrow \boldsymbol{i}_2) \tag{2.45}$$

$$\mathcal{D}_{31} = -\beta_2 p R_{11} + \epsilon P_3 R_{13} \qquad (\text{SV} \rightarrow \boldsymbol{i}_3) \tag{2.46}$$

$$\mathcal{D}_{33} = -\beta_2 p R_{31} + \epsilon P_3 R_{33} \qquad (\text{P} \rightarrow \boldsymbol{i}_3) \tag{2.47}$$

and the particular correspondence between incident wave mode and the component of motion excited on the interface is noted. Next, if we substitute the expressions for the $\mathbf{R}$ matrices for transmission, (which can be found in Červeny̌ (2001) eq. 5.3.3), we can write out the $\mathcal{D}_{ik}$ elements explicitly. Doing so, we get:

$$\mathcal{D}_{11} = 2\epsilon\rho_1\beta_1 P_2 D^{-1}\left[\rho_2\alpha_2 P_1 P_4 + \alpha_1 P_3 P_4 Y - \alpha_1\alpha_2\beta_2 p^2 Z\right] \tag{2.48}$$

$$\mathcal{D}_{13} = 2\rho_1\alpha_1 p P_1 D^{-1}\left[\rho_2\beta_1\alpha_2 P_4 + \alpha_2\beta_2 P_2 X - q P_2 P_3 P_4\right] \tag{2.49}$$

$$\mathcal{D}_{22} = 2\rho_1\beta_1 P_2 \bar{D}^{-1} \tag{2.50}$$

$$\mathcal{D}_{31} = 2\rho_1\beta_1 p P_2 D^{-1}\left[q P_1 P_3 P_4 - \alpha_2\beta_2 P_1 X - \rho_2\beta_2\alpha_1 P_3\right] \tag{2.51}$$

$$\mathcal{D}_{33} = 2\epsilon\rho_1\alpha_1 P_1 D^{-1}\left[\rho_2\beta_2 P_2 P_3 + \beta_1 P_3 P_4 Y - \alpha_2\beta_1\beta_2 p^2 Z\right] \tag{2.52}$$

and these will allow us to compute ground motion at an interface (including the free surface) for an incident ray of known amplitude. In the case of the free surface, the above coefficients are simply computed with $\alpha_2 = \beta_2 = \rho_2 = 0$.

2.1.5 Displacement amplitudes from phonons:

In subsection 2.1.4, we showed how the amplitude of ground motion could be computed at an interface for a ray of known amplitude and polarization interacting with

the interface at a particular time and location (eq. 2.42). The computation takes into account the effects of both the incident and product rays resulting from reflection/-transmission at the interface. The utility of this computation is that it allows us to compute what a receiver would record if it were situated on the interface. The natural use case for this would be a receiver situated at the free surface, but the results are general enough for a receiver situated at an at-depth interface as well.

For our radiative transport implementation, we track the trajectories of phonons assumed to carry discrete quantities of energy through hypothesized Earth models. We treat receivers as flat plates coplanar with interfaces, spanning a "gather area" that serves to catch phonons interacting with the interface in a neighborhood of the receiver. Identifying the receiver with a particular interface allows us to use the conversion coefficient coefficient matrix $\mathcal{D}$ to get local ground motion from the ray-centered phonon amplitudes $\boldsymbol{U}^{(q)}$. But to do this, we need a relationship between the energy a phonon transports and the amplitude of the ray it is intended to represent.

To establish this relationship, we assume that within a sufficiently small neighborhood of the point-like phonon, the the phonon is representative of a plane wave. Considering also the assumption of a narrowband simulation, we assume that over a brief time window, the plane wave is harmonic with angular frequency ω. With these assumptions, we have the relationship between time-averaged energy density ε and displacement amplitude A as:

$$\varepsilon = \frac{1}{2}\rho\omega^2 \left|A\right|^2 \tag{2.53}$$

The energy density of a single phonon is not a defined quantity, but we can get a local approximation to energy density by looking at the local number density of phonons. Thus:

$$\varepsilon = n\,\delta E_0 \tag{2.54}$$

where δE_0 is the quantity of energy carried by a single phonon and n is the number density of phonons in a given locality. With the energy density defined in terms of phonon density, we can define the energy flux vector as:

$$\boldsymbol{S} = \varepsilon \boldsymbol{v} \tag{2.55}$$

where v is the group velocity appropriate for the polarization mode of the phonon (either α for P wave or β for S wave).

Now, to get an approximation of energy density as recorded by a virtual receiver, which we assume samples phonons intersecting the interface over a finite gather area δA, and records them in indexed temporal bins t_i of width δt, we take the total energy E collected by the receiver in a given time window as proportional to both the number of phonons collected and the time and area integrated flux crossing the interface, or:

$$\begin{aligned} E &= \boldsymbol{S} \cdot \delta \boldsymbol{A}\, \delta t = N\, \delta E_0 \\ &= \varepsilon v\, \delta A\, \delta t\, \cos\theta \end{aligned} \tag{2.56}$$

where N is the number of phonons intersecting the gather area in the given time window at incidence angle θ. This now allows us to express the energy density as recorded by a virtual receiver at time t_i as:

$$\varepsilon = \frac{N\, \delta E_0}{v\, \delta A\, \delta t\, \cos\theta} \tag{2.57}$$

Substituting into eq. 2.53 and solving for amplitude, we get:

$$|A|^2 = \frac{2N\delta E_0}{\rho\omega^2 v\, \delta A\, \delta t \cos\theta} = \Lambda^2 \frac{N}{v \cos\theta} \tag{2.58}$$

where Λ can be thought of as a constant for a given receiver, and is defined by

$$\Lambda^2 = \frac{2\,\delta E_0}{\rho\,\omega^2\,\delta A\,\delta t} \tag{2.59}$$

Finally, we can write the amplitude vectors in the ray-centered basis for single phonon arrivals at a receiver interface. For P and S wave modes, respectively, and with S wave polarization vector $\hat{\pi}$, we have:

$$\boldsymbol{U}_{\mathrm{P}}^{(q)} = \Lambda \sqrt{\frac{N}{\alpha \cos\theta}} \begin{bmatrix} 0 \\ 0 \\ 1 \end{bmatrix} \tag{2.60}$$

$$\boldsymbol{U}_{\mathrm{S}}^{(q)} = \Lambda \sqrt{\frac{N}{\beta \cos\theta}} \begin{bmatrix} \hat{\pi} \cdot \boldsymbol{e}_1^{(q)} \\ \hat{\pi} \cdot \boldsymbol{e}_2^{(q)} \\ 0 \end{bmatrix} \tag{2.61}$$

These amplitude can now be used with equation 2.42 to calculate the contribution of a single phonon to the local ground motion as recorded by a receiver embedded in an interface or at the free surface. For a single phonon, it would be natural to take $N = 1$. However, we leave the parameter in the formulation as a proxy for intrinsic attenuation, which may be modeled as a decay in the energy carried by the phonon as it propagates through the model. We can define the instantaneous energy δE carried by the phonon as a fraction of the initial energy δE_0 assigned to the phonon at origination as:

$$\delta E = N\,\delta E_0 \tag{2.62}$$

and use this quantity N in the amplitude formulas, allowing us to keep δE_0 and Λ constant.

2.1.6 Scattering Theory

To handle scattering in our implementation of the radiative transport algorithm, we used the scattering model of Sato, Fehler, and Maeda (2012). Sato et al. derive a set of formulas to describe the statistical likelihood of radiation by polarization mode at a given deflection angle relative to an incident wave vector. This gives us a directional map to use when simulating a scattering event. When tracking a phonon's trajectory, a scattering event is an interruption and re-radiation of the phonon with a new, deflected, propagation direction and, possibly, a new polarization mode (e.g. P/S conversion). The new direction and mode are chosen at random using the directional map as a weight function.

The directional maps come from the scattering coefficients, or g functions, which are derived in terms of a statistical characterization of the heterogeneity spectrum of the local medium. The heterogeneity spectrum can be defined as the autocorrelation strength of the local velocity and density structure as a function of spatial wavenumber. A few simplifying assumptions are made by assuming: (1) that the autocorrelation strengths will follow a von Kármán spectrum, parameterized by an average fractional fluctuation size ϵ, a corner scale a, and a decay rate factor κ called the Hurst parameter, (2) that the density spectrum is proportional to the velocity spectrum by a fixed ratio, ν, (3) that the background ratio γ_0 of P and S velocities is locally uniform, and (4) that the fractional fluctuation of P and S velocities are equal. The parameters characterizing the heterogeneity and determining the scattering coefficients are listed in Table 2.1.

When the scattering coefficients are known, they can be averaged over all deflection angles to give a scattering probability per unit length, from which a mean-free-path can be computed. This is the average propagation distance between scattering events, assuming that individual path lengths are chosen at random and exponentially distributed.

Param.	Description		Category
ϵ	Average fractional fluctuation amplitude:	$\epsilon = \frac{\delta\alpha}{\alpha_0} = \frac{\delta\beta}{\beta_0}$	Het. spec.
a	von Kármán spectrum corner scale		Het. spec.
κ	Hurst parameter; establishes decay rate		Het. spec.
ν	Density fluctuation rel. to veloc. fluctuation:	$\frac{\delta\rho}{\rho_0} = \nu\frac{\delta\beta}{\beta_0}$	Het. spec.
α_0, β_0	Local background P and S velocities		Background
γ_0	Ratio of P and S background velocities:	$\gamma_0 = \alpha_0/\beta_0$	Background
ℓ_0	S-wavenumber of the backgrnd. medium:	$\ell_0 = \omega/\beta_0$	Background
ω	Angular frequency		Freq. band

Table 2.1: Parameters employed in computing the frequency-dependent scattering coefficients $g^{ij}(\psi, \zeta; \omega)$ for a heterogeneous medium characterized by a von Kármán spectrum. Parameters are categorized into those describing the heterogeneity spectrum, those describing the local equivalent-medium background medium, and the frequency at which the coefficients are to be calculated.

2.1.6.1 Basic scattering shapes

The directional maps of scattering probability determined by the scattering coefficients exhibit a complicated dependence on the local medium and heterogeneity spectrum, but some order can be brought to the complexity by observing that the directional dependance can be separated into a factor that depends only on the local background medium and just one of the heterogeneity parameters (ν, which does not describe the spectrum as such but rather the ratio of density fluctuations to velocity fluctuations), and a PSDF factor that that depends on the heterogeneity spectrum and envelopes the directional dependance in the deflection-angle coordinate. The factor that depends only background medium and ν is composed of a set of functions $X_k^{ij}(\psi, \zeta)$ that are referred to as the *basic scattering patterns*. These are derived in Sato et al. Chapter 4 and presented below in eqs. 2.63. These establish the nodal and lobal structure of the scat-

tering directional map. The PSDF factor will skew the amplitudes of the lobal structure and can shift the directional dependence to more favor forward over backward scattering. The basic scattering shapes are illustrated in Figure 2.2. They are indexed by incoming ray mode (P or S), outgoing ray mode (P or S), and outgoing polarization direction (r for longitudinal, ψ for transverse in the polar direction, ζ for transverse in the azimuthal direction).

The X functions are shown below, and depend only on the material parameters γ_0 and ν, and on the deflection angles ψ and ζ, which establish a spherical polar coordinate system with respect to the incident wave vector. The azimuthal coordinate ζ is defined with reference to the incident S polarization vector for incoming S waves.

$$X_r^{PP}(\psi,\zeta) = \frac{1}{\gamma_0^2}\left[\nu\left(-1+\cos\psi+\frac{2}{\gamma_0^2}\sin^2\psi\right)-2+\frac{4}{\gamma_0^2}\sin^2\psi\right] \tag{2.63a}$$

$$X_\psi^{PS}(\psi,\zeta) = -\sin\psi\left[\nu\left(1-\frac{2}{\gamma_0}\cos\psi\right)-\frac{4}{\gamma_0}\cos\psi\right] \tag{2.63b}$$

$$X_r^{SP}(\psi,\zeta) = \frac{1}{\gamma_0^2}\sin\psi\cos\zeta\left[\nu\left(1-\frac{2}{\gamma_0}\cos\psi\right)-\frac{4}{\gamma_0}\cos\psi\right] \tag{2.63c}$$

$$X_\psi^{SS}(\psi,\zeta) = \cos\zeta\left[\nu\left(\cos\psi-\cos 2\psi\right)-2\cos 2\psi\right] \tag{2.63d}$$

$$X_\zeta^{SS}(\psi,\zeta) = \sin\zeta\left[\nu\left(\cos\psi-1\right)+2\cos\psi\right] \tag{2.63e}$$

2.1.6.2 Power spectral density function

In computing the scattering coefficients (g functions), the basic scattering shapes (X functions) will be enveloped by the power spectral density function (PSDF) that summarizes the heterogeneity spectrum in a particular scattering regime. The PSDF gives the functional dependence of heterogeneity strength on wavenumber vector, and can be computed as the Fourier transform of the autocorrelation of a medium (see Sato et al., 2012, Chapter 2). For an isotropic von Kármán spectrum in 3-D, the PSDF de-

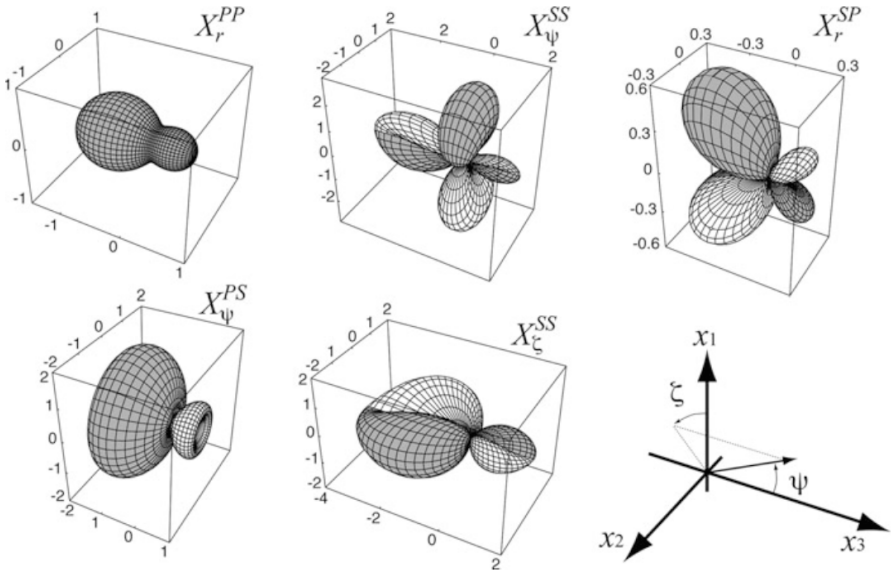

Figure 2.2: 3-D views of basic scattering patterns in 3-D elastic random media for $\gamma_0 = \sqrt{3}$ and $\nu = 0.8$. Incident plane wave is propagating in direction x_3 and S-wave is polarized in direction x_1. Gray shaded area shows the negative polarization in scattering amplitude. *(after Sato et al., 2012, Figure 4.7)*

pends on the heterogeneity parameters ϵ, a, and κ, and on scalar wavenumber parameter m, and is given by:

$$P(m) = \frac{8\pi^{3/2}\epsilon^2 a^3}{\left(1 + a^2 m^2\right)^{\kappa+3/2}} \frac{\Gamma\left(\kappa + 3/2\right)}{\Gamma\left(\kappa\right)} \tag{2.64}$$

where Γ is the gamma function.

2.1.6.3 Scattering coefficients

The scattering coefficients are computed as products of the basic scattering shapes and the PSDF functions with some coefficients that control overall amplitude. These are derived in Sato et al. (2012) and presented below. They are a set of functions $g^{ij}(\psi, \zeta)$ with i and j being elements of $\{P, S\}$ indicating incoming (i) and outgoing (j) wave polarization types, and ψ, ζ respectively representing the polar angle from the direction of propagation and azimuthal angle measured from the initial S polarization axis. The g

functions are:

$$g^{PP}(\psi,\zeta) = \frac{\ell_0^4}{4\pi}\left|X_r^{PP}(\psi,\zeta)\right|^2 P\left(\frac{2\ell_0}{\gamma_0}\sin\frac{\psi}{2}\right) \tag{2.65}$$

$$g^{PS}(\psi,\zeta) = \frac{1}{\gamma_0}\frac{\ell_0^4}{4\pi}\left|X_\psi^{PS}(\psi,\zeta)\right|^2 P\left(\frac{\ell_0}{\gamma_0}\sqrt{1+\gamma_0^2-2\gamma_0\cos\psi}\right) \tag{2.66}$$

$$g^{SP}(\psi,\zeta) = \gamma_0\frac{\ell_0^4}{4\pi}\left|X_r^{SP}(\psi,\zeta)\right|^2 P\left(\frac{\ell_0}{\gamma_0}\sqrt{1+\gamma_0^2-2\gamma_0\cos\psi}\right) \tag{2.67}$$

$$g^{SS}(\psi,\zeta) = \frac{\ell_0^4}{4\pi}\left(\left|X_\psi^{SS}(\psi,\zeta)\right|^2+\left|X_\zeta^{SS}(\psi,\zeta)\right|^2\right) P\left(2\ell_0\sin\frac{\psi}{2}\right) \tag{2.68}$$

The arguments to the PSDFs are the magnitudes of the vector differences between the incoming and the outgoing (scattered) wavenumbers. I.e., for each $P(m)$, we have taken $m = |\boldsymbol{k}_{\text{out}} - \boldsymbol{k}_{\text{in}}|$ and used the result as the argument. Recall that the quantity ℓ_0 is the S wavenumber and note that ℓ_0/γ_0 is the P wavenumber. Since the PSDF that we have chosen to implement is for an isotropic medium, only the magnitude m matters, and not the direction of the vector difference. Further, m, when computed in terms of the scattering angles ψ and ζ, only has dependence on the deflection angle ψ, but not on ζ. This means that the PSDF contribution to the g functions imparts no additional azimuthal dependence, but only affects the ψ dependence. Furthermore, both m and $P(m)$ are monotonic, meaning the PSDF factor cannot add structure (e.g. additional lobes) to the basic scattering shapes but instead only affects the amplitude ratios of the lobes. The PSDF factor can control the overall scattering probability and can shift scattering probability from the backward direction to the forward direction, but it does not change the fundamental shape of the directional pattern.

The dimension of the g functions are inverse length, and they represent a probability of scattering into a given direction per unit length that a phonon has traveled.

2.1.6.4 g_0 and the total scattering coefficient

Averaging a g function over the full solid-angle yields a net probability of scattering into any direction per unit length traveled. If one also sums on the outgoing polarization index (P and S) for a given input index, one gets the total probability per unit length of scattering in any direction, and any output wave type/polarization. This quantity is called g_0.

In other words, for a phonon that starts out with P polarization, we have:

$$g_0^{(P)} = g_0^{PP} + g_0^{PS}$$

and similarly for S phonons. The individual g_0^{**} values are:

$$g_0^{PP} = \frac{1}{4\pi} \oint_{4\pi} g^{PP}(\psi, \zeta)\, \mathrm{d}\Omega$$

and so on. From this, we compute the mean free paths for P and S scattering as:

$$\Lambda_{\mathrm{MFP}}^{\mathrm{P}} = 1/g_0^{(P)}$$
$$\Lambda_{\mathrm{MFP}}^{\mathrm{S}} = 1/g_0^{(S)}$$

2.1.7 Ratio of P to S energy

In this subsection we briefly explore the ratio of P to S energy in a scattering medium and its time evolution from some initial distribution. This is one area of inquiry that could be explored with RADIATIVE3D, our radiative transport code.

2.1.7.1 Scattering conversions

Sato's derivation of the g_0's gives us a set of total-scattering coefficients covering four scattering channels: P→P, P→S, S→P, and S→S. The g_0's tell us a probability of scattering per unit length. The presence of the mode-conversion channels suggests the possibility of an equilibrium distribution of energy among the two modes that may be independent of the initial P/S energy apportionment from the source event. The scattering coefficients, and thus the equilibrium points, are frequency dependent. For a given frequency ω, we can get a rate of conversion scattering in the time domain by defining:

$$Q_{PS}^{-1} = \frac{g_0^{PS}\alpha}{\omega}, \qquad Q_{SP}^{-1} = \frac{g_0^{SP}\beta}{\omega}$$

And for later convenience, we'll define a "total conversion scatter rate" by:

$$Q_{\mathrm{TCS}}^{-1} = Q_{PS}^{-1} + Q_{SP}^{-1}$$

It is then possible to define a scattering conversion operator by:

$$\mathsf{Q}_{\mathrm{Conv.}}^{-1} = \begin{bmatrix} Q_{PS}^{-1} & -Q_{SP}^{-1} \\ -Q_{PS}^{-1} & Q_{SP}^{-1} \end{bmatrix} \tag{2.69}$$

which acts on a population vector $\boldsymbol{p} = \left[\begin{smallmatrix} P \\ S \end{smallmatrix}\right]$, where P and S represent equivalently either the number count of P and S phonons or the energy in the P and S modes, respectively, to give a differential equation in cycle-time by:

$$\frac{\mathrm{d}\boldsymbol{p}}{\mathrm{d}(\omega t)} = -\mathsf{Q}_{\mathrm{Conv.}}^{-1}\boldsymbol{p}$$

such that $\boldsymbol{p}$ has the canonical solution:

$$\boldsymbol{p}(t) = \mathsf{T}\boldsymbol{p} \tag{2.70}$$

where

$$\mathsf{T} = \exp\left[-\omega t\, \mathsf{Q}^{-1}_{\text{Conv.}}\right]$$

Carrying out the matrix exponential, we get

$$\mathsf{T} = \mathsf{T}_1 + \mathrm{e}^{-\omega t\, Q^{-1}_{\text{TCS}}}\, \mathsf{T}_2$$

with

$$\mathsf{T}_1 = \frac{1}{Q^{-1}_{\text{TCS}}} \begin{bmatrix} Q^{-1}_{SP} & Q^{-1}_{SP} \\ Q^{-1}_{PS} & Q^{-1}_{PS} \end{bmatrix}, \qquad \mathsf{T}_2 = \frac{1}{Q^{-1}_{\text{TCS}}} \begin{bmatrix} Q^{-1}_{PS} & -Q^{-1}_{SP} \\ -Q^{-1}_{PS} & Q^{-1}_{SP} \end{bmatrix}$$

Both T_1 and T_2 share the same eigenbasis, and both have eigenvalues of zero and one. The eigenbasis is non-orthogonal, with one vector establishing the equilibrium population distribution, and the other directed along lines of constant population. The basis set is:

$$\begin{aligned} \boldsymbol{v_1} &= \frac{1}{Q^{-1}_{\text{TCS}}} \left(Q^{-1}_{SP},\, Q^{-1}_{PS}\right) \\ \boldsymbol{v}_2 &= (-1,\, 1) \end{aligned}$$

Although T_1 and T_2 have numerically the same eigenvalues, their association to the eigenvectors is reversed, such that, with respect to the eigenbasis, T_1 has eigenvalues $\{\lambda_1 = 1, \lambda_2 = 0\}$, and T_2 has $\{\lambda_1 = 0, \lambda_2 = 1\}$. This means that if we express a population vector as a vector sum in the eigenbasis, e.g.,

$$\boldsymbol{p} = q\boldsymbol{v}_1 + r_0\boldsymbol{v}_2$$

where q is the total population $q = P + S$, and r_0 is a factor that expresses how far the initial apportionment between P and S is from the equilibrium apportionment, then we see that, owing to the zero eigenvalues, the operator T operating on $\boldsymbol{p}$ isolates the effects of T_1 and T_2 on $\boldsymbol{v}_1$ and $\boldsymbol{v}_2$, respectively, and that, owing to the unit eigenvalues, the operators acting on their respective basis vectors are identities, such that:

$$\begin{aligned} \mathsf{T}\,\boldsymbol{p} &= q\mathsf{T}_1\boldsymbol{v}_1 + r_0 \mathrm{e}^{-\omega \mathrm{t}\, \mathrm{Q}_{\mathrm{TCS}}^{-1}} \mathsf{T}_2\boldsymbol{v}_2 \\ &= q\boldsymbol{v}_1 + r_0 \mathrm{e}^{-\omega \mathrm{t}\, \mathrm{Q}_{\mathrm{TCS}}^{-1}} \boldsymbol{v}_2 \end{aligned}$$

From this, we see that the system approaches an equilibrium population $\boldsymbol{p}_{\mathrm{eq.}} = q\boldsymbol{v}_1$, and that the discrepancy from equilibrium, $r_0 \mathrm{e}^{-\omega \mathrm{t}\, \mathrm{Q}_{\mathrm{TCS}}^{-1}} \boldsymbol{v}_2$, decays to zero with time constant $\omega Q_{\mathrm{TCS}}^{-1}$ along a path that keeps the total population q constant. Or in other words, the population as a function of time is:

$$\boldsymbol{p}(t) = \boldsymbol{p}_{\mathrm{eq.}} + r_0 \mathrm{e}^{-\omega \mathrm{t}\, \mathrm{Q}_{\mathrm{TCS}}^{-1}} \boldsymbol{v}_2$$

where the equilibrium distribution $\boldsymbol{p}_{\mathrm{eq.}}$ satisfies:

$$\begin{aligned} P + S &= q \\ P/S &= Q_{SP}^{-1}/Q_{PS}^{-1} \end{aligned}$$

2.1.7.2 Conversion-attenuation operator

The conversion operator (eq. 2.69) of the previous subsection provides a mechanism to predict an equilibrium distribution of phonons in a given scattering regime, however it tells us nothing about energy density in an attenuating medium. Even rough estimates based on assumed attenuation coefficients Q_P^{-1} and Q_S^{-1} would be complicated by the fact that any phonon's history includes an oscillation between P and S states. However,

to analyze the time evolution of an ensemble of phonons that includes the effects of intrinsic attenuation, we can construct a more generalized attenuation operator that includes scattering-conversion within it.

As before, we have the operator Q^{-1}, which we construct as follows:

$$\mathsf{Q}^{-1} = \begin{bmatrix} Q_P^{-1} + Q_{PS}^{-1} & -Q_{SP}^{-1} \\ -Q_{PS}^{-1} & Q_S^{-1} + Q_{SP}^{-1} \end{bmatrix}$$

and the differential equation it is constructed to represent:

$$\frac{\mathrm{d}\boldsymbol{p}}{\mathrm{d}(\omega t)} = -\mathsf{Q}^{-1}\boldsymbol{p}$$

The general solution is as in eq. 2.70, with the evolution operator $\mathsf{T}(\omega t)$ arising from computing the matrix exponential of $-\omega t\mathsf{Q}^{-1}$:

$$\mathsf{T}(\omega t) = \exp\left[-\omega t\,\mathsf{Q}^{-1}\right]$$

The resultant operator, however, is considerably more complicated than the previous case. As before, the operator is a linear combination of two component operators, however there are two time constants involved in the current case. The component operators are as follows:

$$\begin{aligned} \Omega &= \frac{1}{2A}\begin{pmatrix} A-F & 2Q_{SP}^{-1} \\ 2Q_{PS}^{-1} & A+F \end{pmatrix} \\ \Phi &= \frac{1}{2A}\begin{pmatrix} A+F & -2Q_{SP}^{-1} \\ -2Q_{PS}^{-1} & A-F \end{pmatrix} \end{aligned}$$

with the following definitions:

$$\begin{aligned} A &= \sqrt{F^2 + 4Q_{PS}^{-1}Q_{SP}^{-1}} \\ B &= Q_{PS}^{-1} + Q_{SP}^{-1} + Q_P^{-1} + Q_S^{-1} = \mathrm{Tr}\left(\mathsf{Q}\right) \\ F &= Q_{PS}^{-1} - Q_{SP}^{-1} + Q_P^{-1} - Q_S^{-1} = \left(\mathsf{Q}_{11} - \mathsf{Q}_{22}\right) \end{aligned}$$

Leaving the derivation aside, it can be shown that the operator T is composed of Ω and Φ according to the following formula:

$$\mathsf{T}(\omega t) = \mathrm{e}^{-\omega t/\tau_{\mathrm{decay}}}\left(\Omega + \Phi \mathrm{e}^{-\omega t/\tau_\Phi}\right)$$

where the two time constants, τ_{decay} and τ_Φ are given by:

$$\begin{aligned} \tau_{\mathrm{decay}}^{-1} &= \frac{1}{2}\left(B - A\right) \\ \tau_\Phi^{-1} &= A \end{aligned}$$

As in the analysis of the previous subsection, the two component operators of T share an eigenvector basis, and both have eigenvalue spectrum of $\{0, 1\}$, though reversing the association to the respective eigenvectors. This means that if an energy population vector $\boldsymbol{p}$ is decomposed into the eigenvector basis, then the component operators act on the vector components in mutually independent fashion.

The eigenvectors are:

$$\begin{aligned} \boldsymbol{v}_{\mathrm{eq.}} &= \left(\left(A - F\right), 2Q_{PS}^{-1}\right) \\ \boldsymbol{v}_{\mathrm{slip}} &= \left(-\left(A + F\right), 2Q_{PS}^{-1}\right) \end{aligned}$$

The equilibrium vector, $\boldsymbol{v}_{\mathrm{eq.}}$, establishes an energy population ratio ($E_P/E_S =$

$(A - F)/2Q_{PS}^{-1}$) that is stable with respect to time. Populations on this axis will decay in total population with time constant τ_{decay}, but the ratio will not change. The population slip vector, $\boldsymbol{v}_{\text{slip}}$, establishes the pathway along which, separate from the overall decay, the population will approach the equilibrium ratio. This process occurs with time constant τ_{Φ}, which is necessarily faster than τ_{decay}. So long as there is some conversion scattering in each direction, $\boldsymbol{v}_{\text{slip}}$ will be linearly independent of $\boldsymbol{v}_{\text{eq.}}$, though it will not necessarily be perpendicular to it nor will it necessarily be along a line that preserves total population. Thus, before equilibration has completed, the equilibration process itself will add or detract from the overall decay rate. However, once the population ratio is sufficiently near equilibrium, the overall decay will be controlled by the τ_{decay} time constant, which may be of utility in predicting energy fall-off in long-tail coda windows of seismograms in regions of high scattering.

2.1.7.3 Other loss mechanisms, and relation to seismic coda

The analysis here assumes an ensemble of phonons in Brownian motion (i.e., having no preferred or dominant direction) in a localized region, as may occur in a region of strongly deflectionary scattering long after a wavefront has moved through. Intrinsic attenuation alone, however, is not the only mechanism in play that can reduce the energy of the ensemble. The only scattering events considered in the attenuation operator are those that result in mode conversions, and it is assumed that scattered phonons remain in the the population. However, there will of course be a portion of energy that gets lost due to scattering into the deep Earth. Fortunately, the Crust-Mantle boundary has a sizable velocity jump that makes it good reflector, and this will tend to keep some of the energy in the crust. The portion of energy lost through this boundary will likely be proportional to the fraction of phonons incident on the boundary at angles that favor transmission. As the trajectories of the phonons are randomized by the Brownian

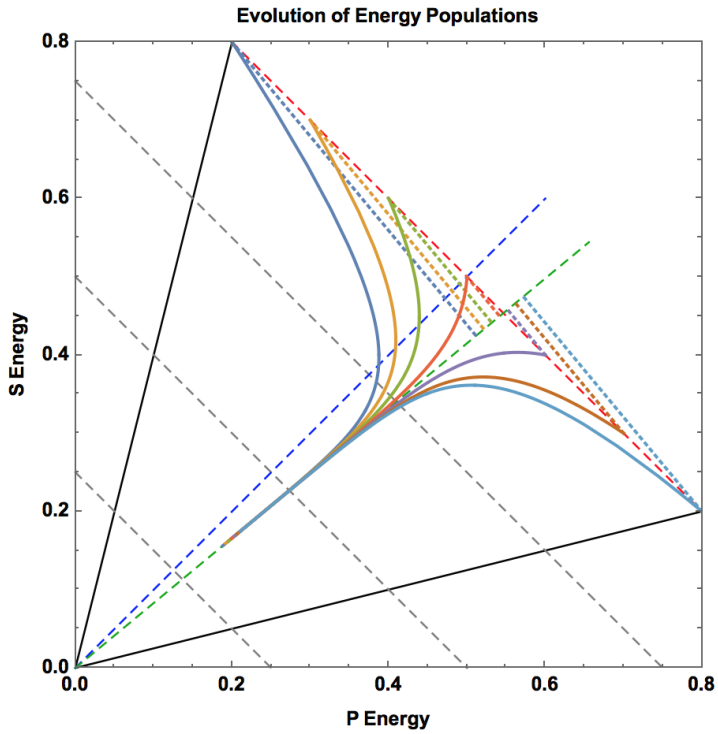

Figure 2.3: Time evolution of energy populations over one decay time. Seven initial populations with $E_{\text{total}} = 1.0$ but different ratios of E_P/E_S are shown evolving over one decay time τ_{decay}. Dashed green radius indicates the equilibrium eigenvector $\boldsymbol{v}_{\text{eq.}}$. Dashed population lines illustrate the evolution towards equilibrium that happens on time scale $\tau_\Phi < \tau_{\text{decay}}$, following paths parallel to $\boldsymbol{v}_{\text{slip}}$. Solid lines show evolution path through population space.

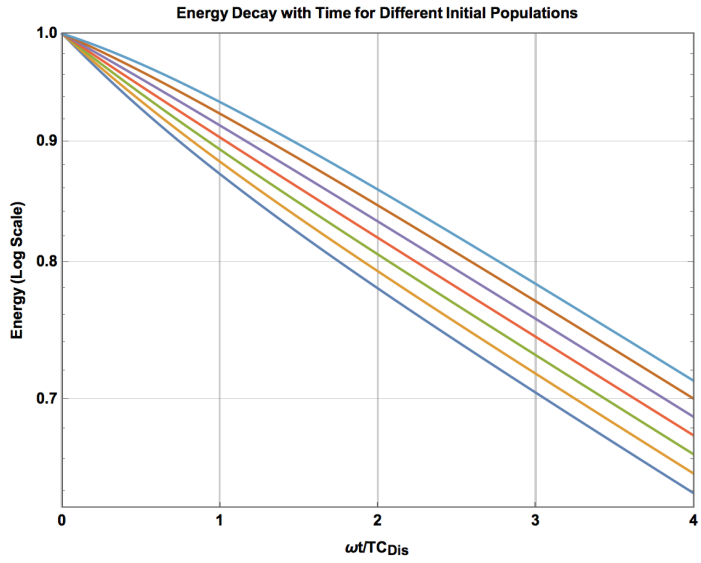

Figure 2.4: Decay of total energy for seven initial populations over four equilibrium times. After equilibrium distribution is achieved, energy decay is an exponential with $1/\mathrm{e}$ time of τ_{decay}.

motion, this will be analogous to an evaporative process, and the loss can likely be modeled as an exponential decay, which could be added as a term in the Q_P^{-1} and Q_S^{-1} parameters.

The other decay mechanism not accounted for here would be the gradual spreading-out of the energy ensemble laterally along the crust layer, thus diminishing the energy density. This is likely governed by a diffusion equation, like an expanding gas cloud, or heat dissipation, and is quite possibly just another exponential term.

If these additional two loss mechanisms are suitably accounted for, it may be possible to make quite accurate predictions for the rate of decay in the long tail region of the coda in high-scattering geographical regions, if details of the material properties and heterogeneity spectrum of the medium are sufficiently well known.

2.2 Implementation

We have implemented a radiative transport algorithm for use with 3-D Earth models in a software package that we call RADIATIVE3D. A very topical overview of the implementation will be given in the next few subsections, and an introduction to how to run the software and interpret its output is given in Chapter 3, "*Radiative3D: Usage*."

2.2.1 Representation of material properties

To represent Earth models, RADIATIVE3D uses a cellular strategy where space is subdivided into adjoining cells in which material properties have mathematically simple representation. Two particular strategies are implemented in RADIATIVE3D.

In one strategy, space is subdivided into stacked layers of uniform material properties separated by interface planes. These are similar to the stratified 1-D models used in numerous time-honored simulation strategies, such as the reflectivity method

(e.g., Kennett, 1983) and others, except that in our implementation the interfaces are allowed to take on arbitrary orientation, allowing a degree of very simple lateral variation (thickening and thinning of layers) to be modeled. The material properties that we represent in the model cells are: two seismic wave velocities (for P and S waves), density, two intrinsic attenuation quality factors ("Q" factors, one each for P and S waves), and a set of parameters describing the heterogeneity spectrum of small velocity perturbations within the model cell which control scattering behavior within the cell. These properties are all uniform throughout the layer cells, and are discontinuous across cell boundaries.

In the other strategy, space is subdivided into adjoining tetrahedral model cells, and three of the material properties, (density, P velocity, and S velocity) are allowed to have gradients, and thus vary linearly within the cell, while the remaining properties are treated as uniform throughout the tetrahedral cell. Tetrahedra are a natural geometry for linearly varying properties because values specified on the four corners uniquely determine the gradient and values throughout the cell. Additionally, because adjoining tetrahedra share three vertices, values may be continuous across cell boundaries. (Or they may, if the user so chooses, be discontinuous.) This allows for smoothly-varying material properties to be modeled.

2.2.2 Ray paths in tetrahedral linear gradient media

If seismic velocities are spatially uniform within a model cell, then phonon ray paths are easy to compute, as they are simply straight-line paths. Changes in phonon trajectory need only be computed when ray paths refract or reflect across cell boundaries, or when they are interrupted by scattering events.

However, if the seismic wave velocities are spatially varying, then the ray paths are curves, and computing them can be complicated. The choice to restrict spatial vari-

ability to simple gradients in tetrahedral model cells, however, yields a simple closed form solution: the ray paths are circular arc segments. The intersection of the circular arc with the surface of a tetrahedral model cell marks the point where a phonon transmits from one cell to the adjoining cell, and the point at which a new arc radius and orientation need be calculated to continue the trajectory through the adjoining cell. The complete phonon trajectory, from generation at the source event to termination at a model boundary or propagation time-out, is a piecewise continuous series of arc segments where the arc parameters are recomputed at cell surfaces or at randomly chosen scattering events. Linear gradients in tetrahedral model cells were utilized by at least one forgoing code, a ray tracing path solver called Raytrace3d by William Menke. Raytrace3d makes no consideration of scattering, and computes only complete paths through tetrahedra. Menke details the formulas used to compute arc paths and their intersections with the surfaces of tetrahedra in an appendix hosted at `ftp://ftp.ldeo.columbia.edu/pub/menke/r3dpaper.pdf`. We further discuss the computation of ray path intersections with tetrahedra surfaces as implemented in our own code in a wiki page located at `https://rainbow.phys.uconn.edu/geowiki/Cell_face_(Radiative3D)`.

2.2.3 The Phonon Propagation Loop

The main loop in RADIATIVE3D is **`Phonon::Propagate()`**, a method of the **`Phonon`** class , declared and defined in *phonons.hpp* and *phonons.cpp*, respectively. **`Phonon::Propagate()`** is responsible for determining the whole trajectory of a phonon, beginning just after generation at the source event, and concluding with phonon death, which will occur either when the phonon exits the model at a non-reflecting model boundary (typically all boundaries except the one representing the Earth's surface), or when the phonon's accrued propagation time exceeds

`Phonon::cm_ttl`, a class member that stores phonon "time to live," which the user may set via a command line option. **`Phonon::Propagate()`** also coordinates the recording of all interactions of the phonon with the virtual seismometers , and the reporting of all vertices of the piecewise trajectory of the phonon, if the user has requested that information, which may be used to visualize or analyze phonon trajectories after the simulation finishes.

`Phonon::Propagate()` is called by the outer loop in **`Model::RunSimulation()`**, (*model.cpp*), which will loop N times, where N is the number of phonons the user wishes to simulate. With each iteration, **`Model::RunSimulation()`** will initialize one phonon, consisting of a randomly chosen take-off angle (TOA) and polarization state from the event source via a call to **`GenerateEventPhonon()`**, (*events.cpp*), which is responsible for choosing these parameters according to probability distributions that model the chosen source event (e.g., according the the moment tensor elements supplied by the user). Once the phonon is initialized, it is propagated by **`Phonon::Propagate()`**.

The **`Phonon::Propagate()`** loop itself is best documented by the extensive commentary in the source code itself, but a basic overview is as follows. With each iteration of the loop, we begin with the phonon at its current location, polarization, and orientation in the current model cell. We first check whether the phonon's time-to-live (TTL) has been exceed. If so, we notify the event reporter, and exit the loop. Control returns to **`Model::RunSimulation()`**. If not, the we compute a path, which may be straight or curved depending on the type of model cell being used, to the bounding surface of the current model cell. The length of this path is kept in a variable. Next, we randomly select a scattering path length according to a distribution appropriate for the scattering regime in effect in the current cell. If the scattering length is shorter than the path length to boundary of the cell, then we advance the phonon by the scattering

length, trigger a scattering event, and return the the start of the loop. If the scattering length is longer than the path to the boundary, then we advance the phonon to the boundary, and proceed to test a number of conditions that will determine whether the phonon is to transmit into the adjoining cell, or whether it is to reflect back into the current cell. It is also possible for conversions between P and S polarization to occur at this stage due to reflection or refraction dynamics. At this stage, it is also possible that the cell boundary is covered by a virtual seismometer at this location, and if so the interaction is recorded. Another possibility is that there is no adjoining cell (a model boundary) and, if it is not a reflection surface, then the phonon will exit the model and the propagation loop will end, returning to the outer loop. Once the appropriate action is determined, the phonon's orientation, polarization state, and the model cell in which it is currently considered to reside will be updated, the event reporter will be notified, and we return to the start of the loop to compute the next piecewise segment of the phonon's complete trajectory.

Chapter 3

Radiative3D: Usage

3.1 Basic operations

RADIATIVE3D is a scriptable command line software tool compiled from C++ source that implements a radiative transport algorithm to simulate the transport of energy from arbitrary source events through three-dimensional Earth models covering local and regional distance scales. RADIATIVE3D is developed and tested in a Linux workstation environment, but utilizes no OS-specific features or libraries, and thus should compile on other architectures as well, including Macintosh OS X and Microsoft Windows. RADIATIVE3D takes as input an Earth model, a description of a source event, and a set of parameters controlling particulars of the simulation sequence and specifications of the desired output. It produces as output a set of virtual seismic envelope traces, or a stream of phonon activity records detailing the complete random-walk trajectories of every phonon simulated, or both. The output can then be visualized or otherwise analyzed with a variety of output analysis tools that we have developed to work with RADIATIVE3D output thus far.

Although a specific software license has yet to be chosen, RADIATIVE3D is intended to be a free and open-source software software tool. At present, the source code can

be obtained from the authors. In the future, a web site will be dedicated to making available the latest versions of the software.

As software, by nature, is a continually evolving product, the descriptions and tutorials in this chapter run the risk of being out-of-date. Thus, as a general matter, the reader is to be referred to the latest online documentation for any changes that may affect the information presented here. However, if the reader wishes to follow these tutorials unaltered, a snapshot of the source code at the time of this document can be browsed interactively at this url: `https://rainbow.phys.uconn.edu/geophysics/trac/browser/Radiative3D/tags/dissertation`. The source code is stored on our servers in a Subversion(TM) repository, and a local "working copy" of the code can be obtained with the following terminal command, or an equivalent:

```
$ svn checkout \
>     https://rainbow.phys.uconn.edu/svn/Radiative3D/tags/dissertation \
>     Radiative3D_diss
```

which will create a folder called *Radiative3D_diss* and put all source code files inside. We can then enter the source directory and compile the code as follows:

```
$ cd Radiative3D_diss
$ make
```

All information and tutorials that follow are assumed to be with reference to this version of the code.

3.1.1 Running the software

A complete user manual for RADIATIVE3D exists on our wiki and can be found at: `https://rainbow.phys.uconn.edu/geowiki/Radiative3D_Manual_Page`. An overview of the software will be presented below, but for complete and up-to-date usage instructions, please visit the manual page.

The software compiles into an executable called *main*. The arguments provided to

main specify the particulars of the desired simulation run, the sources to use for input data, and the locations to put output data. The code runs non-interactively with the terminal (never reads from ***stdin***), and exits upon completion or error. While interpreting parameters and initializing the simulation, the code outputs various log messages and/or descriptions of the simulation environment to ***stdout***, for diagnostic, introspection, or record-keeping purposes. (The user may wish to capture ***stdout*** for this purpose.) During simulation, a progress counter is printed to ***stderr***.

Program invocation looks as follows, except generally with many more arguments specified:

`./main -N 2000 -F 5.0 -E EQ`.

This will simulate 2,000 phonons at a frequency of 5.0 Hz in a built-in test model using a basic strike-slip earthquake as the source event. No output files will be produced (an array of seismometers was not requested). This should complete very quickly, and will print a banner and various log messages to the terminal, the first several lines of which will look very similar to this:

```
**
**  Radiative3D - A code for radiative transport in 3D Earth models
**
**  (c) 2016 Christopher J. Sanborn and the
**           Solid Earth Geophysics Team
**           at the University of Connecticut, Storrs, CT.
**           http://rainbow.phys.uconn.edu/geophysics/wiki
**
**  BUILD STATS:  Revision number: tetra@956M (svn)
**                Floating-point representation: 64-bit
**
**
TOA_Degree: 7                     (default)
Frequency: 5
Number of Phonons: 2000
[...]
```

Additionally, after initialization and commencement of the simulation, a progress indicator will print out that will look like so:

```
@@ __BEGINNING_SIMULATION__
0% of 2000 have been cast.
10% of 2000 have been cast.
20% of 2000 have been cast.
30% of 2000 have been cast.
40% of 2000 have been cast.
50% of 2000 have been cast.
60% of 2000 have been cast.
70% of 2000 have been cast.
80% of 2000 have been cast.
90% of 2000 have been cast.
100% of 2000 have been cast.
@@ __SIMULATION_COMPLETE__
```

In general, however, because of the large number of parameters that one may wish to specify, the user will not run the main executable directly, but will encapsulate it within a script. This process will be described below.

What comprises a "simulation run"?

A "simulation run" is a simulation of N phonons simulated at a single precise frequency F in a particular specified Earth model, with a particular source event, along with zero or more virtual seismometers, often arranged in arrays, specified at various locations throughout the model. The products of a simulation run are a set of zero or more "seis" files containing envelope traces for each individual seismometer, and optionally a "walk" file detailing every change-of-trajectory for every phonon simulated. The latter can be used to visualize the bulk transport of energy through the Earth model. The former can be used to produce envelopes at a single receiver location or travel time curves detailing the ground signal recorded along an array.

Because simulations are single-frequency, the process of producing broadband simulations involves combining simulation runs conducted at various discrete frequencies covering a spectrum of interest. This is discussed further in section 3.2.1, "Waveform output".

Do-scripts

Coordinating the large number of command line arguments needed to carefully design experiments that are well-organized, documented, and repeatable, as well as collecting, organizing, and post-processing or analyzing output files, can be cumbersome. As such, a natural approach is to write shell scripts that define the parameters of interest, construct command line arguments from them, and coordinate the running of the code and collection of output. We call these *do-scripts*, and have included a few examples in our code repository.

The scripts we have written do the following:

1. Define variables to represent the parameters most likely to change from one run to another, and establish default values for those parameters infrequently changed, to ensure consistency.

2. Create a time-stamped output directory in which to aggregate all output and log files. Place a copy of do-script in this directory as a record of the run that is being conducted. Check build-status of the executable and status of the version-control system to record the exact version of the source code that is being run (so that repeat experiments can be conducted with the same code revision). Begin a log file that records timestamps of each step of the process, so that a record exists of how long the simulation took and on what machines the simulation ran. Also, copy various scripts to be used in post-processing into the output directory to be used in the post-processing stage.

3. Run the simulation, with all necessary parameters passed as command line arguments. Record the full command line into the log file, and redirect ***stdout*** to *outdir/stdout.txt* while also mirroring to the terminal, so that a record exists of the simulation run's terminal output.

4. Post-process data (if needed) and run all desired graphics and visualization scripts. In this step, the output data files are used to produce envelopes, travel time curves, videos, or other types of visualizations or analysis.

Two example do-scripts in our source repository include *do-crustpinch.sh* and *do-crustpinch-vids.sh*. Both scripts conduct a simulation run in a crustal pinch model. The former will cast a large number of phonons and produce output that includes envelopes and travel time curves for a set of seismometer arrays. The latter will cast a smaller number of phonons and produce video files showing their propagation throughout the model. Parameters affecting frequency, event focal mechanism, and model-specific parameters such as pinch dimensions, etc., can all be adjusted by editing the script files. In fact, a typical workflow to set up and run a two-condition experiment might look as follows:

```
$ cp do-crustpinch.sh do-exp01cond01.sh  # Experiment 1 Condition 1
$ cp do-crustpinch.sh do-exp01cond02.sh  # Experiment 1 Condition 2
$ emacs do-exp01cond01.sh                # Tweak params for cond 1
$ emacs do-exp01cond02.sh                # Tweak params for cond 2
$ ./do-exp01cond01.sh exp01cond01        # Run condition 1
$ ./do-exp01cond01.sh exp01cond01        # Run condition 2
```

After running both do-scripts, output directories will exists inside a subdirectory named data. Note that when the do-scripts were run, they were provided an optional parameter that served as an identifier for the run. This identifier becomes part of the name of the output directory, to facilitate organization of a large number of simulation results. E.g., listing the data directory might show:

```
$ ls -lh data
total 24k
drwxrwxr-x 2 12K Jun 18 21:51 20160618-215145-exp01cond01-R3D
drwxrwxr-x 2 12K Jun 18 22:06 20160618-220608-exp01cond02-R3D
```

Inspecting the contents of the two output directories will reveal all the envelopes,

travel time curves, data files, log files, and script files produced by and relevant to each simulation run.

3.1.2 Earth Models

RADIATIVE3D is written to support a plurality of modeling approaches, based on the geometric strategy most suited to a given problem. Earth models in RADIATIVE3D are cellular, meaning a model is composed of a collection of adjoining model cells each spanning a specified volume of space and defining the material properties within that space.

Currently, two cell geometries are supported: layers and tetrahedra. Within the source code, the layer cell type is referred to as "cylinder" cells. This is because the cells are taken to have an axial radius defining a bounding surface to keep the cells finite in size. A "cylinder" model is then a layered stack of cylinder cells, much like a stack of pancakes, and serves to define a layered Earth model. One notable difference between traditional "1-D" layered models and the layered models in RADIATIVE3D is that the planar interfaces between layers in RADIATIVE3D can have arbitrary surface normals, meaning the boundary between layers can be inclined, allowing for some very simple lateral variations in the depth profiles to be modeled. Material properties are uniform throughout the cylinder cells, and the interfaces between them become material discontinuities, resulting in refraction and possibly reflection/transmission handling of rays crossing the interfaces.

The tetrahedral modeling strategy, on the other hand, tessellates volumetric space into adjoining tetrahedral subunits. Tetrahedra are a natural tessellation unit, as they support smoothly varying material properties. In RADIATIVE3D, we allow certain material properties (P and S seismic velocities and density) to follow linear gradients. A first-order (linear varying) function in three-dimensional space can be uniquely spec-

	Variable	Description	Gradients Supported?
Elastic Background	ρ	Density	**Yes**
	α	P wave velocity	**Yes**
	β	S wave velocity	**Yes**
	Q_P	Intrinsic attenuation quality factor, P waves	No
	Q_S	Intrinsic attenuation quality factor, S waves	No
Heterogeneity Spectrum	ν	Ratio of density perturbation to velocity perturbation	No
	ε	Velocity perturbation amplitude	No
	a	Length spectrum auto-correllation corner	No
	κ	Von Kármán parameter	No

Table 3.1: Material properties defined by model cells. RADIATIVE3D tracks nine distinct material properties in each model cell. The material properties divide categorically into those defining a slowly-varying or uniform elastic background, and those characterizing a small-scale random perturbation field superimposed on top of the background.

ified by prescribing values at four non-coplanar points in the space. The four corners of a tetrahedron serve as these four points, uniquely specifying the material properties for the region inside the tetrahedron. A mesh of adjoining tetrahedra that share corner nodes allows for the material properties to be continuous[1] throughout the entirety of the Earth model. Should the user wish to explicitly model a discontinuous interface, a mechanism exists to allow a sheet of nodes to be dual-valued, such that tetrahedra on one side of the interface will use one value and those on the other side will use the other value, and reflection/transmission handling will occur for rays crossing the interface. These features allow a high level of fidelity in the Earth modeling process, inclusive of velocity gradients as well as sharp interfaces, even with relatively sparse modeling meshes.

3.1.2.1 Material properties

RADIATIVE3D tracks nine distinct material properties throughout the Earth model. Each material property is either spatially constant or linearly varying within a given

[1] Values will be continuous, first derivatives will be piecewise-constant.

model cell. The material properties can be categorized into two separate groups. The first group characterizes the uniform or slowly-varying background elastic properties of the medium, and the second group characterizes a heterogeneity spectrum assumed to represent small scale perturbations to the background elastic properties. The heterogeneity spectrum controls the stochastic scattering behavior in the phonon propagation loop (described in subsection 2.2.3).

The elastic properties include: density (ρ), P-wave velocity (α), S-wave velocity (β), and two intrinsic attenuation quality factors ("Q"), specifiable as Q_P and Q_S, or as Q_κ and Q_μ. Density and velocity are allowed to have linear gradients within a model cell. The quality factors are treated as uniform within a cell.

The heterogeneity spectrum parameters are represented in this work by the variables ν, ϵ, a, and κ, and are described in detail in subsection 2.1.6. What will be said about them here is they do not specify the perturbation field in detail, but rather characterize it statistically based on an assumed spectrum of perturbation scale lengths parameterized by these four variables. The scattering engine produces appropriate stochastic behavior based on the spectrum. The variables ν, ϵ, a, and κ are assumed to be spatially uniform within a given model cell.

3.1.2.2 Model description grids

Users of RADIATIVE3D do not specify the Earth model directly, insofar as the user is not responsible for specifying the individual model cells. Instead, the user describes the model by inputting a *model description grid*. Note that the term *model description grid* is deliberate and precise, and is meant to be conceptually distinct from the *simulation grids* used by other wavefront simulation algorithms[2]. In particular, the spacing and

[2]Such as Finite Difference algorithms, where time-step and space-step requirements are determined by the frequency and wavelengths of the signals we wish to model. RADIATIVE3D, by contrast, is based on ray tracing, which does not require a simulation grid.

arrangement of nodes in a simulation grid are determined by the needs of the simulation engine, which generally requires a very fine grid to represent the spatial and time derivatives of the signal being simulated. A model description grid, on the other hand, is specified according to the needs of the modeler, and the grid density only needs to be fine enough to capture the structural features of interest. The ability of the model cells to represent velocity gradients allows for significant savings in terms of grid density, as stair-steps are not needed to approximate gradients. As a matter of brevity, the term *model mesh* will sometimes be used in this work and in the RADIATIVE3D source code as a synonym for model description grid.

A model description grid, in RADIATIVE3D, is a lattice of points, or node locations, at which known or hypothesized material properties are specified. Thus the user is only responsible for specifying properties at those known locations. The model construction routines in the RADIATIVE3D source code are responsible for appropriately constructing model cells to "fill" the space mapped out by the model description grid. Thus the user need not know the details of how volumetric space is tessellated into tetrahedra, for example.

At present, RADIATIVE3D supports two grid formats, one which supports the description of layered models based on the cylinder cell type, and one which supports the description of more intricate 3D models based on the tetrahedral cell type. In the future, support for GeoTess is planned. GeoTess (Ballard et al., 2012) is an Earth modeling format defined and maintained by Sandia National Laboratories.

3.1.2.3 Curvature and the Earth-Coordinate Subsystem

Internally, RADIATIVE3D represents models in a Cartesian coordinate system with no particular geographical reference frame to establish meaningful directions such as "Up," "Down," "East," or "West," etc. Users, however, will likely prefer to ex-

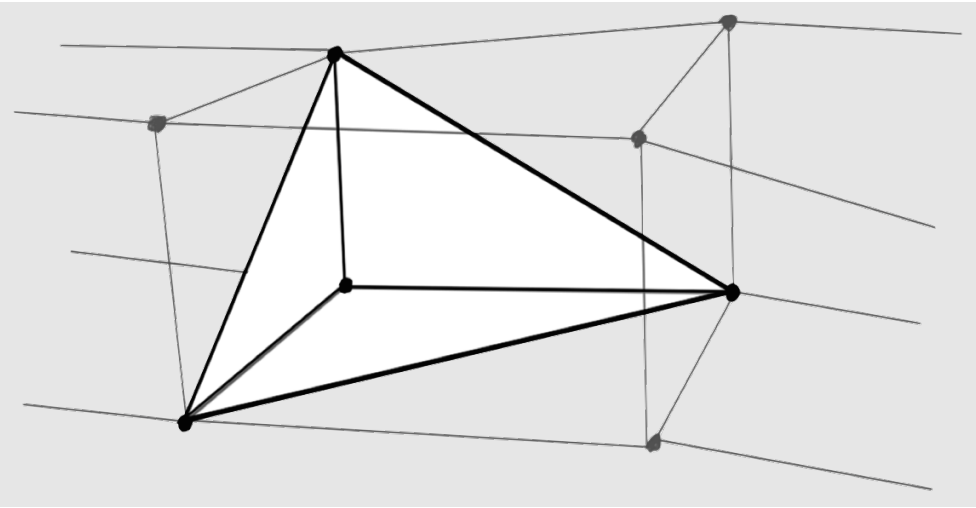

Figure 3.1: Tetrahedral model cell in Warped Cartesian Grid (WCG) node lattice. Eight adjacent grid nodes define a cuboidal subunit of the WCG. Each cuboidal subunit is tessellated into five tetrahedral cells, filling the space. One such tetrahedral cell is shown highlighted here.

press Earth models in geographically meaningful coordinate systems, and allow RADIATIVE3D to perform the appropriate conversion to the internal coordinate system. To enable this, RADIATIVE3D implements an Earth Coordinate Subsystem (ECS) to handle mapping between three coordinate contexts: *internal*, *grid*, and *output*. The user may choose from a variety of supported coordinate systems and mapping modes for grid input and data output, and the ECS handles conversion to/from the internal representation.

The curvature mapping feature of the ECS allows an easy way for the modeler to selectively choose whether or not to include Earth curvature in their models, without having to explicitly include it in their grid files. For example, when specifying node locations for an Earth model using a Warped Cartesian Grid, the user might choose to express locations in Latitude, Longitude, and Elevation (LLE). The ECS can then be directed to map surfaces of constant elevation onto planar surfaces in internal model space (in which case Earth curvature is suppressed), or onto concentric spherical surfaces (in which case Earth curvature is modeled). A third mapping mode exists in

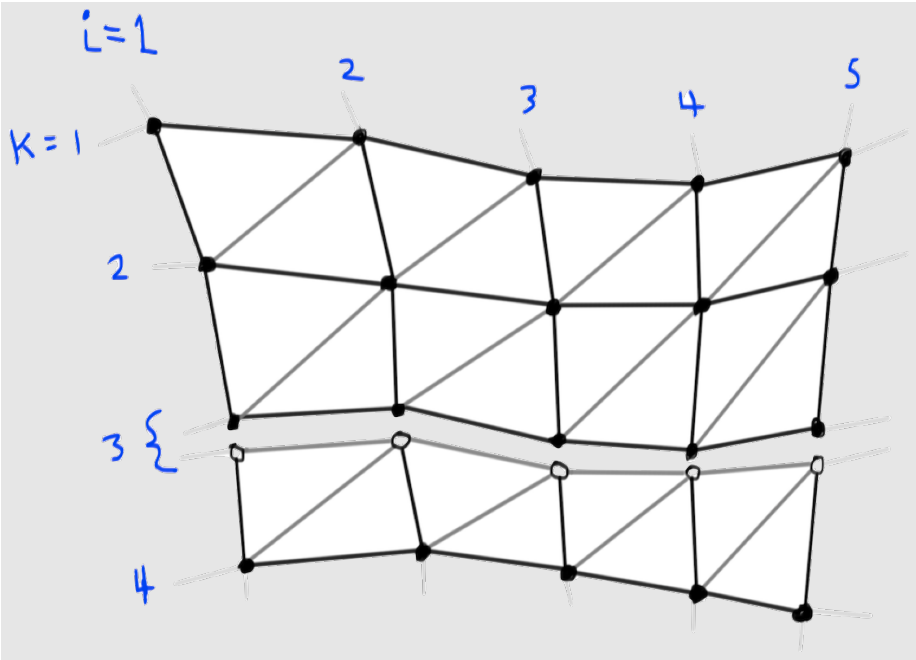

Figure 3.2: Warped Cartesian Grid (WCG) with tetrahedral tessellation, represented schematically in two dimensions. Earth model material properties are specified on the node locations. The model cells composing the Earth model then interpolate the material properties within the cells. For properties that support gradients (density, P and S seismic velocities), the gradient is determined by the values on the four corner nodes of each tetrahedron. For properties that do not support gradients, the value is taken from the node with the smallest index within each cuboidal subunit of the WCG. Because adjacent tetrahedra share corner nodes, properties that support gradients are continuous across cell boundaries. If a sharp discontinuity is desired, a "sheet" of nodes can be designated to have two distinct sets of values, establishing different regimes for the cells above vs. below the sheet.

which surfaces of constant elevation map to planes, but their depth is adjusted according to an Earth Flattening Transformation (EFT). This option is useful for models built on the stacked-layer cell type, in which the layer interfaces are necessarily planer and cannot represent curved surfaces directly. In the case of EFT mapping, the ECS also adjusts seismic velocities, and potentially other material properties, according to the particular transformation being used. For more on Earth Flattening transformations, Aki and Richards (1980) has a discussion in "Box 9.9".

The ECS also allows aspects of the simulation that need to be geographically-aware to operate. For example, a virtual seismometer needs to know which direction repre-

Code	Desc.	Flat	Curved	EFT
ENU	*East, North, Up;* (km, km, km)	Supported	Planned	Supported
RAE	*Range, Azimuth, Elevation;* (km, deg., km)	Supported	Supported	Supported
LLE	*Lat., Lon., Elevation;* (deg., deg., km)	Planned	Planned	Planned

Table 3.2: Supported coordinate systems and curvature mappings for model description grids in RADIATIVE3D. Modelers may describe Earth models in the coordinate system of their choice, and then choose the manner in which Earth curvature should be handled when translating the model into RADIATIVE3D's internal coordinates. A "flat" mapping means that lattice points of equal elevation in the model grid will map to flat planes in the internal coordinate space. A "curved" mapping means that lattice points of equal elevation will map to concentric spherical surfaces in the internal coordinate system. The "EFT" is a flat mapping that applies an "Earth flattening transformation," which makes adjustments to depth and seismic velocity to artificially simulate the effects of Earth curvature. This is useful for models based on cylinder ("pancake") model cells, as in these models the cells are separated by planar interfaces which cannot be curved. For both curved and EFT mappings, the Earth radius is an adjustable parameter, allowing, e.g., Lunar or Martian curvatures to be modeled.

sents its z-axis. In a curved-surface Earth model, the geographic "up" direction (in the internal coordinate system) is location-dependent. The ECS can compute this direction for the seismometer object based on its knowledge of the user's choice of mapping mode. Relational reference directions are also computed by the ECS. For example, a seismometer whose axes are to be aligned as radial, transverse, and z, (RTZ) with respect to a source event, will have those directions computed by the ECS.

Taken altogether, the ECS allows modelers to describe their models in the coordinate system most appropriate for the particular problem at hand, and preserves applicability of RADIATIVE3D to both local and regional or modeling needs. The ECS is implemented in source code files *ecs.hpp* and *ecs.cpp*, which contain detailed commentary on usage and implementation.

3.1.2.4 Inputting Earth models

At the time of this writing, a model ingestor (code which reads a model description from a data file and constructs a model in memory in RADIATIVE3D's internal repre-

sentation) has not yet been written[3]. The simulation examples we have constructed use hard-coded models, which require a recompile if the model is significantly changed. (Some aspects of the hard-coded models are parameterized, though, and these parameters are accessible via command line arguments, lessening the need for recompiles in some circumstances.)

Hard-coded models are defined in a source file called *user.cpp*. (This file is designated for user-specific customizations, including hard-coded models.) As outlined in subsection 3.1.2.2, models are described via model description grids. RADIATIVE3D implements a grid-building API through the **`Grid`** class, defined in *grid.hpp* and *grid.cpp*. The **`Grid`** class makes available methods for defining the structure of the grid, for setting the locations of grid nodes, and for setting material attributes at each grid node. When RADIATIVE3D is directed to use a compiled-in model (this is currently the default and only supported behavior), the model constructor will call upon a method of the **`Grid`** class called **`Grid::ConstructGridManual()`** to define the grid that will be used to construct the Earth model in memory. Because **`ConstructGridManual()`** is a user-specific customization, this method (in contrast to the rest of the **`Grid`** class) is defined in *user.cpp*. The **`ConstructGridManual()`** method accepts one argument, which is an array of **`Real`**'s (a real number type) which can be used to parameterize elements of the hard-coded model. This array of reals is passed-in to the code via the `--model-compiled-args` command line argument. In practice, **`ConstructGridManual()`** is implemented as a dispatcher function, calling out to another function to define the grid. This is so that a variety of custom hard-coded models can be defined as separate functions in *user.cpp*, and the particular choice of model can then be selected via a one-line change in **`Grid::ConstructGridManual()`**.

[3]Support is planned for both a native modeling format as well as for reading models from GeoTess (Ballard et al., 2012) files.

Listing 3.1 Grid building in CrustPinchWCG(), user.cpp. Grid nodes are indexed in three indices and referenced via WNode(). Locations are set via SetLocation() using coordinates in the chosen mapping scheme. Material properties are set via SetAttributes(), with arguments specifying velocities, density, attenuation "Q", and heterogeneity spectrum.

```
// *** Code snippet from CrustPinchWCG() in user.cpp
// *** (near line 1260 in revision 956, modified for brevity)

gr.SetSize(nR,nAzis,nZ);      // Sets index bounds
gr.SetIndexBase(0);           // When addressing nodes, use base 0
gr.SetMapping(Grid::GC_RAE, Grid::GC_CURVED); // Coordinate mapping

for (Index iaz = 0; iaz < nAzis; iaz++) {

  for (Index iz = 0; iz < nZ; iz++) {

    Real azi  = Azis[iaz];              // Azimuth value
    Real azin = Azis[nAzis-iaz-1];      // picked in reverse order
    Real azicr  = AzisCR[iaz];          // Azi's for close-range
    Real azicrn = AzisCR[nAzis-iaz-1];  // Close range reverse order

    gr.WNode( 0,iaz,iz).SetLocation( -120,  azin,  ZBase[iz] );
    gr.WNode( 1,iaz,iz).SetLocation(  -60, azicrn, ZBase[iz] );
    gr.WNode( 2,iaz,iz).SetLocation(   60,  azicr, ZBase[iz] );
    gr.WNode( 3,iaz,iz).SetLocation(  120,   azi,  ZBase[iz] );
    gr.WNode( 4,iaz,iz).SetLocation(  220,   azi,  ZBase[iz] );
    // ... (some lines omitted)
    gr.WNode(12,iaz,iz).SetLocation(  890,   azi,  ZBase[iz] );
    gr.WNode(13,iaz,iz).SetLocation( 1020,   azi,  ZBase[iz] );

  }

  for (Index ir=0; ir<nR; ir++) { // Attributes vary only in depth index

    gr.WNode(ir,iaz,0).SetAttributes(VpVs(4.50,2.60), 2.20, QSe, HSSe);
    gr.WNode(ir,iaz,1).SetAttributes(VpVs(4.52,2.61), 2.21, QSe, HSSe);
    gr.WNode(ir,iaz,1).SetAttributes(VpVs(6.20,3.58), 2.80, QCr, HSCr);
    gr.WNode(ir,iaz,2).SetAttributes(VpVs(6.24,3.60), 2.82, QCr, HSCr);
    gr.WNode(ir,iaz,2).SetAttributes(VpVs(7.70,4.44), 3.39, QMo, HSMo);
    gr.WNode(ir,iaz,3).SetAttributes(VpVs(8.000,4.46),3.40, QMa, HSMa);
    gr.WNode(ir,iaz,4).SetAttributes(VpVs(8.040,4.48),3.50, QMa, HSMa);
    gr.WNode(ir,iaz,4).SetAttributes(VpVs(8.045,4.49),3.50, QMa, HSMa);
    gr.WNode(ir,iaz,5).SetAttributes(VpVs(8.051,4.50),3.43, QMa, HSMa);
    gr.WNode(ir,iaz,6).SetAttributes(VpVs(8.301,4.52),3.32, QMa, HSMa);
    gr.WNode(ir,iaz,7).SetAttributes(VpVs(8.848,4.78),3.46, QMa, HSMa);

  }

}
```

To get a sense of how to use the API to construct a model description grid, the reader may wish to peruse function **`CrustPinchWCG()`** in *user.cpp*. (This is the function which defines the crustal pinch models used in Chapter 5 of this dissertation.) The first 120 lines or so of this function are dedicated to interpreting the arguments passed in from the command line and parameterizing the geometry of the model. The remainder of the function is dedicated to building the array of grid nodes. (See Listing 3.1 for a snippet.) The grid scheme used in this function is a warped cartesian arrangement, in which the grid nodes are indexed in three indices. We are building an azimuthally-symmetric model in this example, and so we have chosen to map the indices to range, azimuth, and depth, (in that order).[4] The grid itself is instantiated as an "object" (in C++ parlance) and is given the identifier **`gr`** in the code. The grid is essentially a collection grid "nodes", which are objects of class **`GridNode`** (see *grid.hpp* for specifics). A writeable reference to each **`GridNode`** object is returned via a method of the **`Grid`** class called **`WNode()`** where the arguments are the three indices identifying the desired node. Before we can set the desired locations and attributes of each node, we first dimension the grid via a call to **`gr.SetSize()`** (line 4 in Listing 3.1). Next we set mapping attributes in line 6 wherein we tell the grid API that we will use range, azimuth, and elevation (RAE) as our coordinate system, and that we want level contours to follow Earth curvature (**`GC_CURVED`** , see subsection 3.1.2.3).

Next, we loop over the node indices to set locations and material properties. Locations are set for each node via calls to **`SetLocation()`** , where the arguments are a generic triple which will be interpreted (due to our selection of **`GC_RAE`** mapping) as range (km), azimuth (degrees), and elevation (km above surface reference level).

[4]Index order, and the physical meaning ascribed to it, generally doesn't matter, and is essentially a user choice. However, material discontinuities spanning a sharp interface will be assumed by the model-building code to be discontinuous in the direction of the third index. Since material discontinuities of geographical importance (e.g. the Mohorovičić discontinuity) are horizontally oriented, the user will in general want to use the third index as a depth index, with increasing index number mapping to deeper locations.

The inner loop is unrolled in lines 17 through 24 over the range index, so that the range values are explicitly coded, whereas the azimuth and elevation values are parameterized. Next, in lines 30 through 40, we set material properties for each node via calls to **`SetAttributes()`**. Here, we unroll over the depth index, since the material properties are a function of depth, but are uniform over range and azimuth. **`SetAttributes()`** takes four objects as arguments. The first is an object of class **`Velocity`** coding the P and S seismic velocities at the location of the grid node. The second argument is an object of class **`Density`**. The third is of class **`Q`** and codes the P and S intrinsic attenuation factors, and the last argument is of class **`HetSpec`** and characterizes the heterogeneity spectrum in four parameters: *nu*, *epsilon*, *a*, and *kappa* (see subsection 3.1.2.1). (The **`Velocity`**, **`Density`**, **`Q`**, and **`HetSpec`** classes enforce a type-locking mechanism for physical dimensions and are defined and explained further in source file *elastic.hpp*.) Lastly, take note that in lines 31 and 32, as well as lines 33 and 34, and 36 and 37, that the **`SetAttributes()`** method is called twice for the same depth index. These successive calls establish a discontinuity in material properties when crossing the interface defined by that depth index. When interpolating material properties between grid nodes, the first call to **`SetAttributes()`** determines the values that will be used for points located "just above" the interface, and the second call determines the values used for locations "just below" the interface.

For a depiction of the model described by the **`CrustPinchWCG()`** function, see Figure 5.1 in Chapter 5.

3.1.3 Visualizing output

Visualization tools have been written for the two primary types of output that RADIATIVE3D produces: (1) seismic trace data, which reports seismic signals recorded at the surface, and (2) trajectory random-walk data, which reports the

motions of phonons throughout the body of the Earth model. Trace data from a single virtual seismometer can be visualized as three-axis envelope traces, showing signal amplitude as a function of time at a single location in the Earth model. Trace data from a set of many virtual seismometers having some sequential relationship to one another (e.g. a linear array) can be visualized as a travel time curve, where signal amplitude maps to image density and is plotted as a function of both time and distance. This allows the visual identification of particular seismic phases, based on velocities or other visible characteristics in the time-and-distance domain. Trajectory random walk data, on the other hand, can be used to produce time series or videos showing the propagation of thousands or millions of phonons as they move through the model. With sufficient phonon density, this enables us to see the evolution of wave fronts as they interact with the various features of the Earth model.

3.1.3.1 Envelopes

Visualizations are produced by scripts written in the GNU Octave programming language (Eaton et al.), which is an open-source implementation of the Matlab language. Envelope plots are produced via the script *vis/seisplot/seisplot.m*, which defines a function for reading the trace data from the seis-file output of RADIATIVE3D and producing the appropriate plot. An example envelope plot is shown in Figure 3.3. Once a simulation has completed, seismometer output is deposited into individual files in a specified output directory. For each file that we wish to plot, we call the **`seisplot()`** script from within Octave as follows:

```
$ cp vis/seisplot/*.m outdir/  # Copy seisplot scripts
$ cd outdir
$ ls
seis_000.octv  seis_001.octv  seis_002.octv ...
$ octave
GNU Octave, version 3.6.3
Copyright (C) 2012 John W. Eaton and others.
> seisplot("seis_002.octv");
> print("Envelope_002.png", "-r160");
```

This will produce an envelope plot in *Envelope_002.png* with a resolution of 160 dpi (a total image width of 800 px).

The user will generally not have to manually produce every envelope. The process will typically be automated in the do-script, as can be seen in the example do-script, *do-crustpinch.sh*.

3.1.3.2 Travel time curves

Travel time curves are produced by the **`arrayimage()`** function defined in *vis/seisplot/arrayimage.m* (a GNU Octave script). An example travel time curve is shown in Figure 3.4. Travel time curves combine traces from an array of seismometers, and the trace data from these several seismometer files is first combined into a single data structure via the **`array()`** function in *vis/seisplot/array.m*. From the output directory in which the *seis* files (*seis_nnn.octv*) reside, the following illustrates the process of producing the figures:

```
$ ls
array.m        arrayimage.m   ...    ...     seis_000.octv
seis_001.octv  seis_002.octv  seis_003.octv  seis_004.octv  ...
$ octave
GNU Octave, version 3.6.3
Copyright (C) 2012 John W. Eaton and others.
> AR = array("seis_%03d.octv",0,159); # Read seis_000 to seis_159
> NORMCURVE = arrayimage(AR, [1 1 1], 2.0, [0 400]);
>           # First pass gets normalization curve...
> NORMCURVE = normcurve_fitpowerlaw(NORMCURVE,10,160);
>           # Smooth normalization curve, power-law assumption.
> arrayimage(AR, [1 1 1], 2.0, [0 400], NORMCURVE, 8.0);
>           # Plot TT curve with desired normalization.
> annotate_regions(ROI); # Annotate regions (optional).
> annotate_array();      # Annotate phases (optional).
> print("Traveltime_Array0.png", "-r200");
>           # Produce PNG at 200 dpi.
```

The **arrayimage()** function, as called above, will plot the summed energy from all three channels (second argument, `[1 1 1]`, directs this), on an amplitude scale (square-root of energy, indicated by third argument of "`2.0`"), over a time window of `0`-to-`400` seconds, using **NORMCURVE** as a normalization curve, and setting the amplitude axis (color axis) limit to `8.0`.

Signal normalization is a question that deserves some consideration. Obviously, the further one gets from the event source, the less signal intensity that will reach the surface. If the entire travel time plot were plotted with a uniform normalization factor, image density would cluster in the near-ranges, and phase structure would be difficult to resolve. One obvious way to address this, (and the strategy that is implemented by default if a normalization curve is not supplied to the **arrayimage()** function), would be to normalize each and every seismometer independently, so as to fit the signal into the desired color-axis range at all distance ranges. This allows structure to be resolvable at all distance ranges. However, it tends to mask range-dependent effects on the intensity of the signal, because signals at all ranges are compressed into the

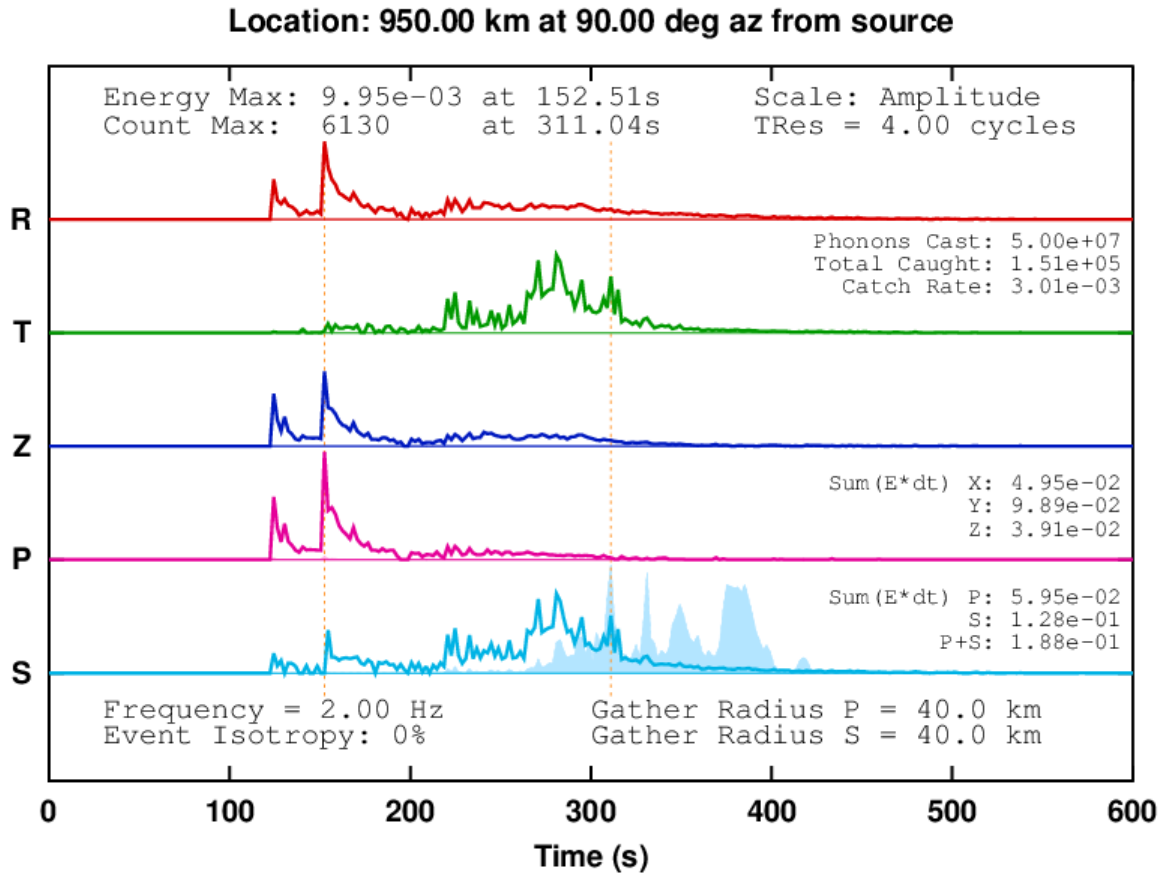

Figure 3.3: Example envelope waveform. Five channels are shown from a single seismometer. The top three are the traditional directional decomposition, here radial, transverse, and z. The bottom two decompose the signal based on polarization state (P or S) of the incoming wave energy. The P and S traces show a second series (shaded) indicating phonon capture rate, which omits effects of intrinsic attenuation and serves a purely diagnostic purpose. Vertical pick markers indicate energy maximum and phonon capture maximum. Other annotations include simulation frequency, gather radii, temporal resolution (bin width) relative to cycle period, time-integrated energy, and statistics comparing the number of phonons simulated to the number captured by the seismometer. The scale of the traces are "amplitude," indicating that the quantities plotted are the square root of the energy flux quantities output by RADIATIVE3D, which are further explained in Section 3.2.1.

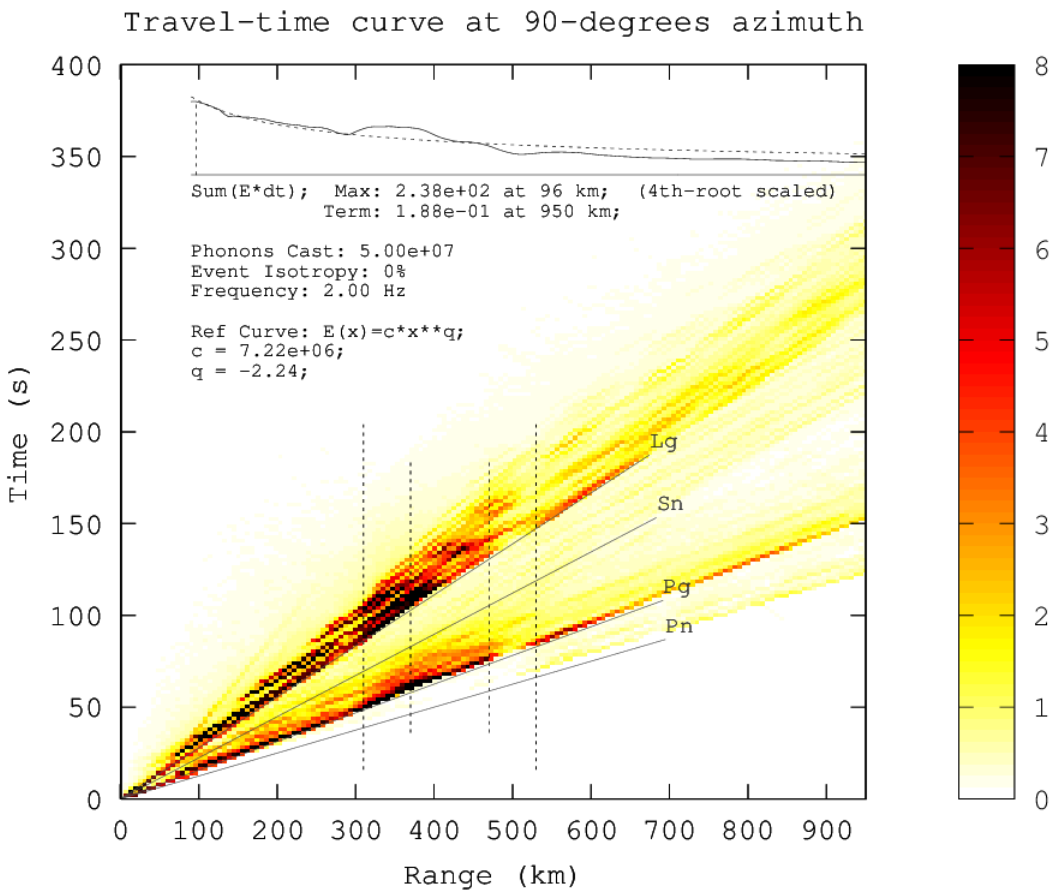

Figure 3.4: Example travel time curve. These plot energy flux amplitude (square root of energy flux signal, see subsection 3.2.1) as a fraction of a distance-dependent reference curve, in this example determined by a power law fit to a baseline simulation. The reference curve serves to establish an "expected" peak amplitude against which to plot relative amplitudes in the specific case. (In this example, the baseline condition has a uniform layered crust structure, whereas the specific (presented) case has a pinched crust in the region between 310 km and 530 km range (demarcated by vertical lines). The reduced image density beyond 530 km indicates the attenuation/disruption due to the structural feature.) The reference curve (dashed line) along with time-integrated energy of the current plot (solid line) are shown as overlays at the top of the plot. They are plotted on a 4th-root scale to accommodate compressed vertical space.

same visible color range. This could mask a "shadow zone," for example, or other interesting effects.

A more ideal way to address signal normalization is to compute a range-dependent normalization curve that establishes our *expectation* of intensity at each range, and to plot signal amplitude relative to that expectation. The **`NORMCURVE`** structure that we create encodes the time-integrated energy (area-under-the-curve of the energy traces) for each seismometer as a function of range from source event. This function can reveal a complex relationship between signal intensity at the surface and range from source. To make this relationship more visible in the travel time plots, we first smooth this function by assuming that there will be a general fall-off of intensity with range, and so we compute a power-law fit to **`NORMCURVE`** in order to define an ideal (expectation) normalization curve. We then normalize against this curve in the second pass of the **`arrayimage()`** function.

Note that while this allows for much more information to be visibly apparent in the travel time curves for any single simulation run, this approach can be especially useful when the normalization curve from one simulation run is used in the travel time curve production of another simulation run. For example, one might use the normalization curve measured from a baseline condition to plot the travel time curve of a test condition in which some aspect of model structure has been modified. If these modifications result in an intensity deficit or surplus in a particular range window, this effect will become visible in the travel time curve. If the reader inspects the scripting of travel time curve production in *do-crustpinch.sh*, he or she will notice that the script checks for the presence of a file containing a baseline normalization curve, and will use that curve if present.

As with the envelope plots, the production of travel time curves is usually automated within the do-script, as seen in *do-crustpinch.sh*.

3.1.3.3 Other visualizations

The normalization curves discussed in the previous subsection are interesting in their own right, because they reveal complexities in the relationship between signal reaching the surface and distance from the source event. As such, it can be instructive to plot the (un-smoothed) normalization curves from multiple experimental conditions against each other for comparison. We call these plots "energy plots", and they are produced with the script in *vis/seisplot/normcurve_compare.m*. Examples of these plots can be seen in Figures 5.8 and 5.9 in Chapter 5.

3.1.3.4 Videos

A handful of GNU Octave scripts for producing videos exist in the *vis/scattervid/* directory. The videos show the propagation of phonons plotted on a backdrop showing model structure, and, with sufficient phonon density, can illustrate the evolution of wavefronts throughout the model. A do-script for producing videos of the crust pinch models exists in *do-crustpinch-vids.sh* in the top level directory. The video scripts depend on FFmpeg (http://www.ffmpeg.org) to convert a cache of still frames into a playable video, and the user will want to make sure this is installed.

3.2 Interpreting output

3.2.1 Waveform output

For each virtual seismometer in a simulation run, a file is generated on completion containing metadata and waveform traces. The files are named according to the pattern *seis_nnn.octv*, where *nnn* in an incrementing integer value. The suffix .octv indicates that the data is in a structured plaintext format readable by GNU Octave (Eaton et al.),

an interactive programming language similar to MATLAB, which we use for analysis and visualizations.

The metadata in each file include (1) the location of the seismometer, (2) the orientation of each axis, (3) a text code indicating the axis scheme (ENU for east, north, up; RTZ for radial, transverse, z; etc.), (4) the gather radius of the seismometer, (5), the recording time window of the traces, (6) the number of temporal divisions, or time bins, that make up a trace, and (7) the frequency of the simulation run, which can be thought of as the dominant frequency of the passband of the seismometer. Additionally, the seismometer file records the location and moment tensor of the source event. Although the source information is also output elsewhere, its presence in the seismometer files facilitates annotation of visual analyses, such as indicating the range from source on an envelope plot or travel time curve, for example. The location and directional quantities are processed through the Earth Coordinate Subsystem (ECS, see subsection 3.1.2.3), and thus are expressed in a coordinate system of the user's choice. The seismometer files are written by a member function of the **`Seismometer`** class called **`OutputOctaveText()`** , which is defined in *dataout.cpp*, and which serves as the definitive reference on the format and encoding of the output file.

The waveform traces in each file are series of non-negative numbers that represent intensity of radiative flux intercepted by the seismometer as a function of time, apportioned over several recording channels according to a number of apportionment schemes. Two apportionment schemes are currently utilized, and produce a total of five channels in the output file. The first apportionment scheme, responsible for three channels, is based on direction of ground motion, and apportions intensity over the three directional axes of the seismometer. The second scheme, responsible for two channels, apportions according to polarization state, yielding a P channel and an S channel. The apportionment is additive, meaning that summation across the three

directional channels yields the total intensity, as does summing across the P and S channels.

The traces contain no phase information, and so cannot be used to construct full waveforms, but are instead used to construct envelopes. The radiative flux is a flux of phonons carrying a quantity proportional to energy (see below) that attenuates according to an intrinsic attenuation model describing thermal energy loss as the phonon propagates through the Earth model. Thus the radiative flux intensity is proportional to an energy intensity incident on the 2-D manifold that acts as the collection surface for the seismometer.[5] The energy intercepted by the collection manifold is scaled by the area of the manifold[6] and the temporal width of the time bins so that quantities are comparable between seismometers with different gather radii and between simulation runs that might use different time bin widths.

Thus, the specific quantity reported by RADIATIVE3D as a "trace" can be stated as such: a channel-apportioned attenuated phonon count per unit gather area per unit time. The dimensions of this quantity are phonons per area per time. The physical interpretation of this is dependent on a user choice of what "one phonon" is taken to represent. In the simplest case, the user may wish to interpret a single phonon as simply carrying a quanta of elastic energy. The physical dimensions of the trace are then energy per area per time, or energy intensity. However, in a more general sense, the user may wish to consider that the simulation runs at a single frequency, and therefore represents only a portion of the energy spectrum of a source event. The

[5]Because phonons are point particles, they cannot be captured by a seismometer described only by a single point locus. Instead we treat seismometers as a surface manifold, usually identical with the model surface or with some interface within the model, though truncated by a fixed *gather radius* to establish a finite size and locality of the seismometer. This truncated manifold then acts as the collection surface for the seismometer.

[6]In the current version of the code, the area of the manifold is treated heuristically as πR^2 of the gather radius R of the seismometer, which assumes that the collection surface is planar and that the nominal seismometer location is embedded in the plane. If instead the manifold has curvature or topography, or if the nominal locus is significantly above or below the manifold, then the computed gather area may become inaccurate.

construction of a broadband envelope would then consist of a weighted summation of simulation results over several frequencies, according to a spectral decomposition of the source-time function. In this case, a "phonon" may be considered as an energy quantity per unit frequency, making the trace dimensions energy per area per time per frequency. A further consideration is that the simulation algorithm in RADIATIVE3D assumes that all phonons are emitted from the source instantaneously at time $t = 0$. A real source event, however, will have some finite duration. If the energy spectrum of the source event is known as a function of time, (and if the duration is not so brief as to be for practical purposes instantaneous), then the user may wish to convolve the set of single frequency traces with the time dependence of each frequency band, thus simulating the finite duration of the source event. In this case, a "phonon" may be considered as a quantity of energy per unit frequency per unit time in the source-time function. This makes the dimensions of the trace energy per area per time-squared per frequency.

Additional traces

In addition to the flux traces, the seismometer files also include two integer-valued "count" traces in which the numbers are non-negative integers representing the number of phonons caught in each time bin. One such trace counts P phonons and the other counts S phonons. These count traces serve primarily a diagnostic purpose, as there is no way to predict a real-world seismic signal from them, since phonon count alone ignores effects of intrinsic attenuation, which must be accounted for in order to get an energy signal.

3.2.2 Signal relation to ground motion

The signal currently output by RADIATIVE3D for seismic traces is proportional to the area density of energy incident on an interface per unit time, as discussed above. When the square root of this signal is plotted, the result is an amplitude-like signal that we present as envelope traces in our envelope plots. An analyst working with RADIATIVE3D output, however, may be more interested in a ground motion signal, in analogy to the ground-motion velocity signal output by many real-world seismometers. At the present time, there is no direct conversion process between the energy flux signal output by RADIATIVE3D and ground motion, though planned improvements to the software will allow this as an alternate selectable output quantity. The reason for the lack of convertibility is because ground motion in a volume element is related to the energy density in that volume element, but the quantity reported by RADIATIVE3D is the energy interacting with the surface of the volume element, coming from an aggregation of phonons arriving with differing propagation velocities (for P and S phonons) and at differing incidence angles, making impossible an after-the-fact conversion between area energy flux rate and volume energy density (each phonon would have a different conversion factor). The solution to this is to do the conversion inside the simulation as the phonon interaction is recorded and to output either an energy density signal or a ground motion signal directly from RADIATIVE3D for visualization and analysis rather than the energy flux signal as is currently done. A detailed discussion of the computation of ground motion from phonon incidence, including free-surface corrections resulting from mode conversions of the surface-reflected signal, appear in Chapter 2 section 2.1.5.

Chapter 4

Coda and Scattering Experiments

Radiative transport modeling can combine the effects of both large-scale (deterministic) and the small scale (statistical) structure on the coda envelopes of high frequency regional seismograms. We describe a computer code to implement radiative transport modeling that propagates packets of seismic body wave energy along ray paths through large-scale deterministic 3-D structure, including the effects of velocity gradients, intrinsic attenuation, source radiation pattern, and multiple scattering by layer boundaries and small scale heterogeneities specified by a heterogeneity spectrum. The spatial distribution of these energy packets can be displayed as time snapshots to aid in the understanding of regional phase propagation or displayed as a coda envelope by summing at receiver bins. These techniques are applied to earthquakes and explosions recorded in the Lop Nor, China region to model observed narrow band passed seismic codas in the 1 to 4 Hz band. We predict that source discriminants in this region based on P/Lg amplitude ratios will best separate earthquake and explosion populations at frequencies 2 Hz and higher.

4.1 Introduction

4.1.1 The importance and limitations of very high frequency seismogram modeling

Efficient modeling of high-frequency regional seismograms is important to both the assessment of earthquake hazards and to nuclear treaty verification. Earthquake damage correlates most strongly with ground motion in the 0.5 to 10 Hz frequency band (Trifunac and Brady, 1975). The spectrum of an earthquake seismogram in the 2 to 6 Hz band can discriminate it from that of an explosion or quarry blast better than either its estimated source mechanism or source depth (Walter et al., 1995, 2007; Allmann et al., 2008).

Given the importance of high frequencies to hazards estimation and seismic monitoring, it would be desirable to model high frequency regional seismograms with enough computational efficiency that many structural and source models could be routinely tested and compared against observations within several hours or less. Unfortunately, even with advances in parallel computation and increased access to large clusters of processors, numerical modeling in three-dimensional Earth models rarely exceeds ranges of several hundred wavelengths for computing times less than one day. At 5 Hz this range is typically less than 100–200 km, which is valuable to predictions of earthquake strong ground motion, but limited in value to nuclear verification where monitoring stations may be 1000 km or further from regions of interest in Eurasia. Even if the computational inefficiency can be overcome, as frequency increases it becomes increasingly difficult to obtain perfect knowledge of small-scale structure needed to predict a seismogram of an earthquake or an explosion wiggle for wiggle.

4.1.2 Limitations of empirical Green's functions and path calibrations

Several approaches are available for handling imperfect knowledge of Earth structure for high frequency coda modeling. Strong ground motion modeling often employs empirical Green's functions obtained from recordings of previous earthquakes in a region at similar ranges of interest to simulate the effects of scattering by unknown small-scale heterogeneity (Hartzell, 1978). Sophisticated interpolating (e.g., kriging, Fan et al., 2002) has been used predict the behavior of the amplitudes of regional seismic phases over unsampled new paths using the amplitudes of these phases recorded over other paths within a region. These techniques may address the effects of unknown small-scale (<10 km heterogeneity) if it is relatively uniform over a large region. Resolvable sharp gradients in Moho depth and deep sedimentary basins, however, can still strongly affect azimuthal variations in the character and detection of regional seismic phases (e.g., Cao and Muirhead, 1993; Sens-Schönfelder et al., 2009). These resolvable, deterministic, structures make simpler 1-D structural models, empirical Green's functions, and path interpolation unreliable tools for predicting waveform behavior.

4.1.3 An efficient method of incorporating multiple-scales of heterogeneity

To address this problem, this paper extends a radiative transport algorithm that combines ray theory to treat the effects of known large-scale structure together with the effects of multiple-scattering by perturbations of the large-scale structure. The following sections describe the implementation of the algorithm and its application to high-frequency regional seismograms in the vicinity of the Lop Nor, China test site.

4.2 Technical Approach

4.2.1 Radiative transport

The term *coda* for the envelope of complex arrivals following direct P and S waves at local and regional distances originated with work by Aki (1969), who recognized their origin to be due to multiple scattering by small-scale (relative to wavelength) heterogeneities in the crust and lithosphere (Aki and Chouet, 1975). The radiative transport algorithm models these coda envelopes by simulating the diffusive transport of elastic energy through processes of multiple scattering in a medium having random fluctuations in elastic properties. Its earliest and most extensive applications are to the propagation of electromagnetic waves, especially to the description of stellar images and scintillation (Chandrasekhar, 1960). Gusev and Abubakirov (1987) extended applications of radiative transport to elastic scattering using a Monte Carlo technique for tracking multiply scattered particles of elastic energy. Extensions to realistic Earth models followed in the work of Hoshiba (1997), who included particle interactions with layer boundaries, Yoshimoto (2000), who included effects of velocity gradients within layers, and Margerin et al. (2000), who elaborated treatment of S wave polarization. An early significant result of work with radiative transport is that multiple scattering often becomes the dominant mechanism controlling coda shapes at frequencies above 5 Hz on Earth, explaining a spindle-shaped, lunar-like, seismic coda observed in this frequency band (Wu, 1985). Hoshiba (1993) developed an analysis method now in common use for measuring the relative contributions of intrinsic vs. scattering attenuation from the shape of seismic codas. Comprehensive reviews of seismic radiative transport modeling include the text by Sato, Fehler, and Maeda (2012) and an AGU monograph chapter by Margerin (2005). Przybilla et al. (2009) have compared the method against finite-difference synthetics in 2-D, validating body wave coda predictions of the radiative

transport method.

Following Shearer and Earle (2008), an algorithm to implement radiative transport can be summarized in a few of simple steps:

1. Choose a heterogeneity power spectrum for the medium (Fig. 4.1). The heterogeneity power spectrum is the Fourier transform of the spatial autocorrelation of small-scale heterogeneity of seismic velocities and density.

2. From the heterogeneity spectrum, calculate the angle-dependent scattering coefficient, $g(\theta, \phi)$, which is the scattering power per unit volume at a deflection angle given by θ and ϕ. The g functions are calculated for P-to-P, P-to-S, S-to-S, and S-to-P scattering.

3. Average each g function for over all angles, forming, for example, $g_0 = 1/\ell_{\mathrm{P}}$, where path ℓ_{P} is the mean free path of a P wave.

4. Calculate a path length r to represent one segment of the random walk by assuming r is an exponentially distributed random number having a mean value ℓ_{P} for P waves and ℓ_{S} for S waves, respectively. I.e, compute $r_{\mathrm{P}} = -\ln(x)$, where x is a random number between 0 and 1.

5. Adjust ray tangent by choosing a scattering direction computed by sampling a probability density taken from the Born scattering coefficients $g(\theta, \phi)$ of the heterogeneity model (Sato et al., 2012), and continue computing the path of the scattered energy packet by iterating steps 3 and 4. Random numbers sampling the scattering radiation patterns also determine whether the scattering results in conversion into P or S, and determines S polarization. The evolution of S polarization along a path is handled by assigning S polarity as an angle in a local SV versus SH coordinate system (Shearer and Earle, 2004). This is an approximation that ignores the possibility of elliptical S polarization induced by SV interaction with

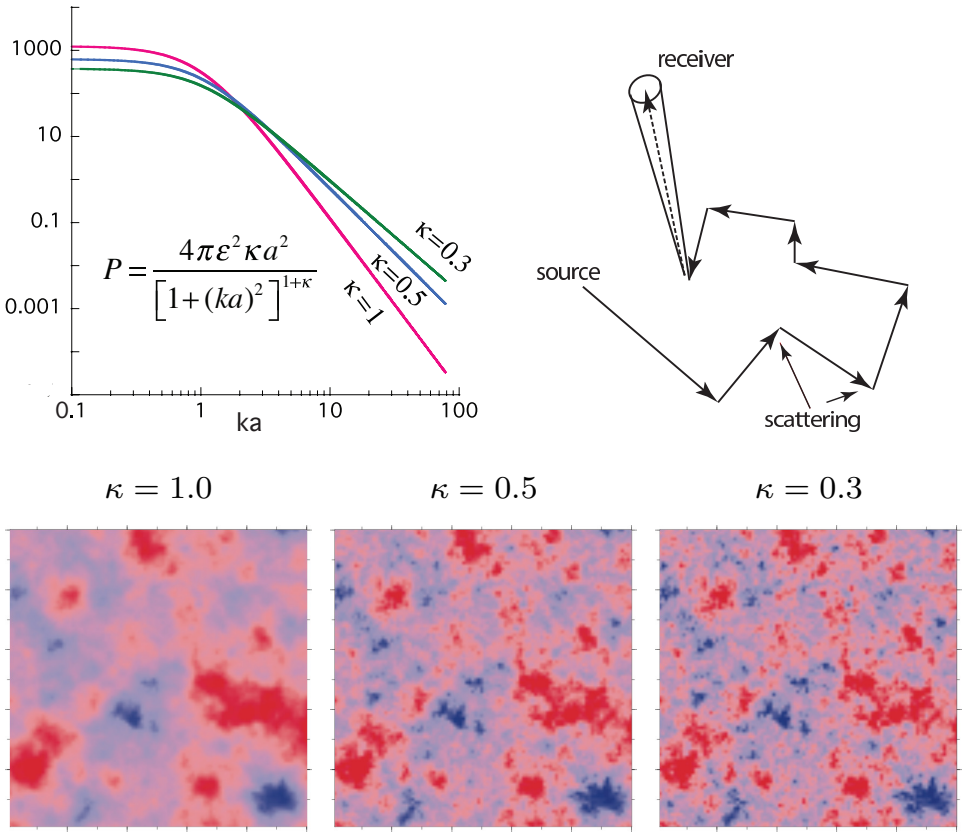

Figure 4.1: Top right: random walk in which deterministic ray paths conveying packets of elastic energy are interrupted by scattering events in a heterogeneous medium. Top left: 2-D von Kármán heterogeneity spectrum as a function of correlation wavenumber k; spectral power is flat up to $k_{\text{corner}} \sim 1/a$, after which smaller spatial scales decay with fall-off rate controlled by Hurst parameter κ. Bottom: example spatial realizations of heterogeneity spectra for various κ at a magnification level of ten scale lengths a.

interfaces, which can be remedied using the approaches of Margerin et al. (2000) and Bal and Moscoso (2000).

4.2.2 Advantages of radiative transport

The principle advantage of radiative transport is the ability to simulate the effects of small-scale structure without the need for model meshes that are dense enough to explicitly describe that structure. Instead, the model mesh describes only the large-scale, long-wavelength equivalent ($ka \gg 1$) background medium, against which small-scale

heterogeneities are assumed as a random perturbation field. The small-scale heterogeneities are described in the aggregate via a small number of statistical parameters, rather than describing the perturbation field explicitly in fine detail.

4.2.3 Construction of models

Earth models consist of a background deterministic component, consisting of first-order discontinuities with topography separating layers having 3-D variation of velocities and densities interpolated over a course grid, and a perturbed statistical component, specified by a heterogeneity spectrum parameterized by the power of velocity and density fluctuation and a small number of spectral shape parameters informing the functional dependence of the power spectrum on wavenumber (Figs. 4.1 and 4.2).

Since Frankel and Clayton's (1986) work demonstrating the effects of small-scale heterogeneity on the seismic wavefield, significant advances have occurred in statistical characterization and understanding of such heterogeneity. Goff et al. (1994) described a procedure by which models having the spatial statistics of polycrystalline or multi-modal assemblages of rocks can be generated. Work beginning with Levander et al. (1994) and Pullammanappallil et al. (1997) makes it possible to formulate statistical models for common sedimentary and metamorphic formations. Model statistics can be modified as needed to reproduce the three-component behavior of the coda of regional seismic phases. Strong emphasis is placed on correctly characterizing the statistics of small-scale heterogeneities in the upper, highly heterogeneous, 10 km of the earth, which may correlate with the depth to a brittle to ductile transition in the crust (Rachman and Chung, 2016). Small-scale statistics affect the partitioning of P and S energy on the three-components of motion by the effects of scattering near the source and receiver. These small-scale statistics can strongly affect the performance of discriminants tuned to differences in sources occurring at the depths of contained

nuclear tests.

Lateral variations in crustal thickness, basin depths, mountain roots, and lateral tectonic transitions also significantly affect the phases used for discrimination and detection. One example is the study by Pedersen et al. (1998), who explain anomalous Rayleigh to Love mode conversion from Lop Nor explosions by changes in crustal thickness at the boundary of the Tarim Basin and Tian Shan mountain belt. Moho topography and basin thickness can also strongly affect the propagation of Lg (Cormier and Anderson, 2004). The scale of these types of lateral structural variations is often large enough to be resolvable by local and regional reflection and refraction experiments, gravity and magnetic data, regionalization by surficial geology, and global surface wave inversions. Hence, we refer to these types of structures as deterministic. The types of data used to infer deterministic structure are collected at widely different spatial scales, presenting a challenge to the parameterization of a three-dimensional model appropriate for a region surrounding a particular seismic station. The parameterization should be flexible enough to be specified at high resolution where data is available and at lower resolution where it is not. Resolution should be high to describe features important to regional wave propagation, such as Moho and basin topography, but can be lower near interfaces having smaller velocity contrasts and lower with increasing depth in the mantle, where heterogeneity power decreases.

4.3 Software package

4.3.1 Implementation and relation to existing codes

Our code RADIATIVE3D is a tool for seismic radiative transport modeling with flexible Earth model and moment-tensor source input. The simulation engine includes deter-

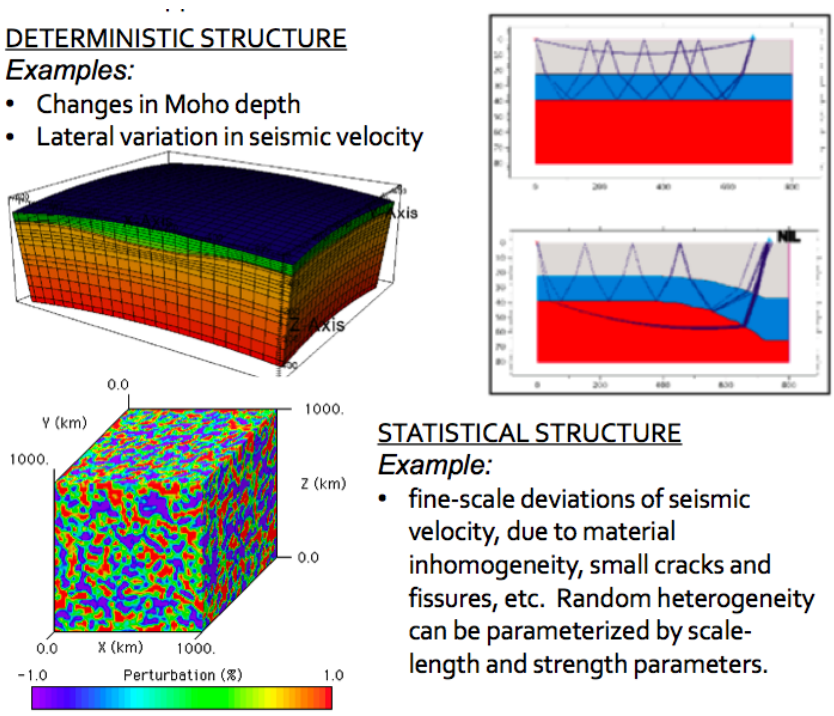

Figure 4.2: Top: examples of known (deterministic) large-scale heterogeneity and its effects on S and Lg waves (multiple critically reflected S waves at the Moho). Bottom: example of a realization of 3-D small-scale (statistically described) heterogeneity.

ministic ray tracing for longitudinal and shear propagation modes in linear velocity gradients, stochastic scattering controlled by heterogeneity parameters, reflection and transmission handling at sharp boundaries, and attenuation modeling from internal friction. Visualization and post-processing tools have been created to produce seismic envelopes, travel-time curves, and three-dimensional body-wave visualizations of energy propagation from RADIATIVE3D output. RADIATIVE3D is made available to the scientific community as a free and open-source software product. RADIATIVE3D is a new code that takes major inspiration from two prior codes, namely Raytrace3D (Menke, 2005) and PSPhonon Shearer and Earle (2004). Raytrace3D solves ray propagation in 3-D velocity models, and PSPhonon performs radiative transport, including scattering, in 1-D layered-Earth models. Our code performs both tasks in a full 3-D model.

In our implementation, elastic energy is considered to originate from a source event at a fixed location and time. Energy is then propagated as a discrete packet or bundle, which we refer to as a phonon (in analogy to the particle representation of light as a stream of photons). A phonon's path through an Earth model is determined by a combination of ray theory to handle the deterministic propagation through the composite medium background structure (large scale structure, capturing broad variations in elastic properties), and by scattering theory, which is the stochastic handling of scattering due to small-scale heterogeneities, assumed as perturbations to the background structure. A scattering event is, in essence, an interruption and randomization of a particle's otherwise deterministic progress. With a sufficient number of phonons emitted from the source event, a picture of the energy transport throughout the model begins to emerge. Records of the phonon travel paths can be used either in bulk or via selection criteria to visualize this energy transport. In bulk, the data can be used to produce movies or still-frames of the evolving wavefront throughout the three-dimensional model. Via selection criteria, just those phonons that, for example, interact with the surface within a specified gather radius of a hypothetical seismometer can be collected and used to produce seismic waveforms of surface movement at the given location. With a sufficient quantity of virtual seismometers, travel-time curves can also be produced.

4.3.2 Visualizing output

RADIATIVE3D produces output suitable for visualization with external tools. The output capabilities fall into two major categories: (1) event reporting, and (2) seismic energy binning. Event reporting means reporting the progress of individual phonons in a play-by-play manner. Examples of events in this context include: generation, scattering, crossing a model boundary, free-surface or discontinuity interface reflection and

transmission, etc., or simply reporting the position of each phonon at regular time intervals. When these events are analyzed in post-processing, detailed pictures of energy propagation can be constructed. One of the first visualization tools developed was a GNU Octave script to produce videos illustrating P and S energy propagation in the Earth model.

4.3.2.1 Wavefront and coda evolution

Figure 4.3 shows energy propagation visualized as a time series plot of phonon locations in a model cross section. Individual wavefronts, and the coda developing behind them, can be easily discerned in these plots. Red dots represent P phonons, blue dots represent S phonons. Reflection and refraction occurs at interfaces between model layers at which velocities are discontinuous. Conversions between P and S polarization are driven by both scattering and reflection/transmission events. A sequence of still frames showing small increments of simulation time can be assembled into videos showing wavefront and coda evolution. Producing event logs with sufficient detail to show clear wavefront evolution requires on the order of a few thousands or a few tens of thousands of phonons, and are produced in approximately ten minutes of CPU time on Intel i7 or comparable workstations.

4.3.2.2 Seismometer output

The other form of output which can be analyzed for quantification or visualization is binned seismic energy. RADIATIVE3D allows for the placement of virtual seismometers along any surface designated as a collection surface. Whenever a phonon interacts with a collection surface within a specified gather radius of a seismometer, the energy of that phonon is recorded by the seismometer, decomposed into three Cartesian energy axes, and binned into time windows. At the end of simulation, these energy bins

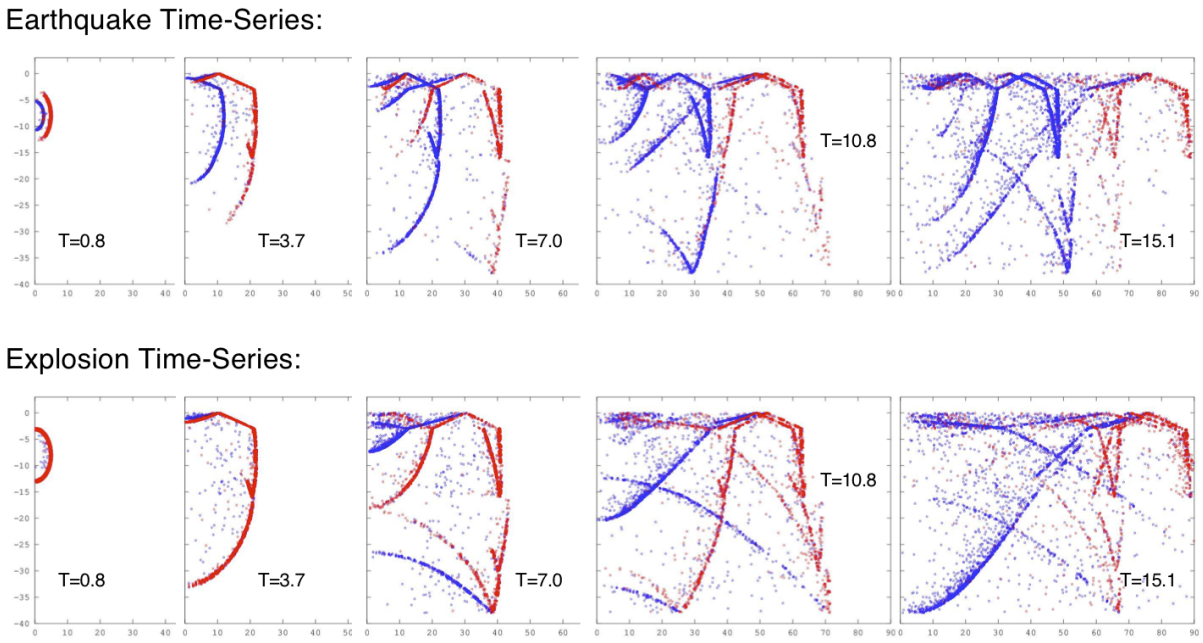

Figure 4.3: Energy propagation visualized as a time series plot of phonon locations in a model cross section. Note the initial absence of the S wavefronts (blue) in the explosion time-series and its progressive development with time due to multiple scattering and interaction with the free surface.

are output and can be interpreted as seismic energy traces, suitable for making envelope plots. Figure 4.4 shows seismic envelope plots produced by the RADIATIVE3D code. The traces represent amplitude of the 2.0 Hz signal arriving at a virtual seismometer approximately 800 km from a hypothesized earthquake source (left) and explosion source (right) synthesized in a 3-D model of the Lop Nor, China region having a simple deterministic structure and trial statistical structure. The quantity presented as "amplitude" is the square root of accumulated energy flux in each time bin, having been decomposed into directional components based on the direction of particle motion of the incident ray, accounting for polarization mode and angle. Accumulated energy flux is the sum of the path attenuated energy carried by phonons interacting with the gather surface within the time bin divided by the gather area and the time bin width. Each phonon is assumed to depart from the event source with unit energy. Attenuation based on scattering or geometric spreading need not be considered, as both

these factors already control the likelihood of interaction with the gather surface. A unique feature of the phonon method is that the instantaneous polarization state of the phonon is known at the time of interaction with the surface, and this allows us to present two additional signal channels showing the decomposition of energy based on instantaneous P or S polarization state. Note that the polarization state decomposition does not cleanly separate the Pg and Lg arrivals. This is due to mode conversion occurring at the interface of the crust with a thin sediments layer at the surface of the model. The P and S amplitude channels denote the instantaneous state, not the propagation mode of the bulk of the phonon's travel history. We set the depth of the explosion event to 2.0 km below the surface, and the depth of the earthquake event to 6.0 km below the surface, with a focal mechanism of the 2003-03-13 earthquake given by Selby et al. (2005).

Traces from multiple seismometers arranged in a linear array can be combined to make travel-time curves. Figure 4.5 shows the travel-time curves from the earthquake and explosion simulations that were presented in Fig. 4.4, row (a). Each curve combines output from 160 virtual seismometers linearly spaced from the source to the maximum range at 800 km. Image density is proportional to the amplitude signal described above. A range-varying normalization curve is applied to the amplitudes so that the seismic phases remain distinct at all ranges. Thus, the image density is not proportional to absolute amplitude, but is relative to the normalization point. These plots allow the identification of seismic phases based on group velocity and time offset.

Discretization of take-off angle (TOA) for phonons generated at the event source implies that care must be taken in choosing an appropriate gather radius for seismometers at long range. In the absence of the randomizing effect of scattering, coarsely-chosen angular increments can result in unreachable zones at range. The gather radius should be chosen large enough to sufficiently average a surface area that can be reached by at

least a small number of TOAs, while still maintaining the desired degree of localization in the signal output. Increasing the TOA density can also fulfill this purpose, but comes at a performance cost of searching larger arrays when probabilistically choosing the TOA for each new phonon, as the directionality of the event source is treated through weighting the probability of each discrete angle. An appropriate balance between TOA density and gather radius will allow stable signal output with a manageable number of phonons sprayed from the event source. For the frequency bands and ranges presented here, stability (where increasing the number of phonons sprayed does not appreciable change the shape of the simulated coda) was achieved with 140 million phonons per simulation, with gather radii of 20 to 40 km at 800 km range. Take off angles were discretized into approximately 5.2 million discrete angles representing nearly equal solid-angular increments chosen via a triangular tessellation procedure. Single-threaded computation time on Intel i7 and comparable desktop workstations in our lab took between 4 to 7 hours per simulation. Earthquake simulations generally take longer than explosion simulations, due to the greatly increased rate of scattering that occurs in the more strongly excited Lg wavefront.

4.4 Example Application

4.4.1 Lop Nor Region: Deterministic model and data

We focused our modeling efforts on the Lop Nor, China region (Fig. 4.6) because it is one of few regions in which nuclear tests and earthquake waveforms are well recorded at accessible global seismic stations and networks. Sykes and Nettles (2009) found that more than half of the earthquakes in the Reviewed Event Bulletin (REB) of the International Monitoring System (IMS) occurred within 100 km of six Lop Nor test sites

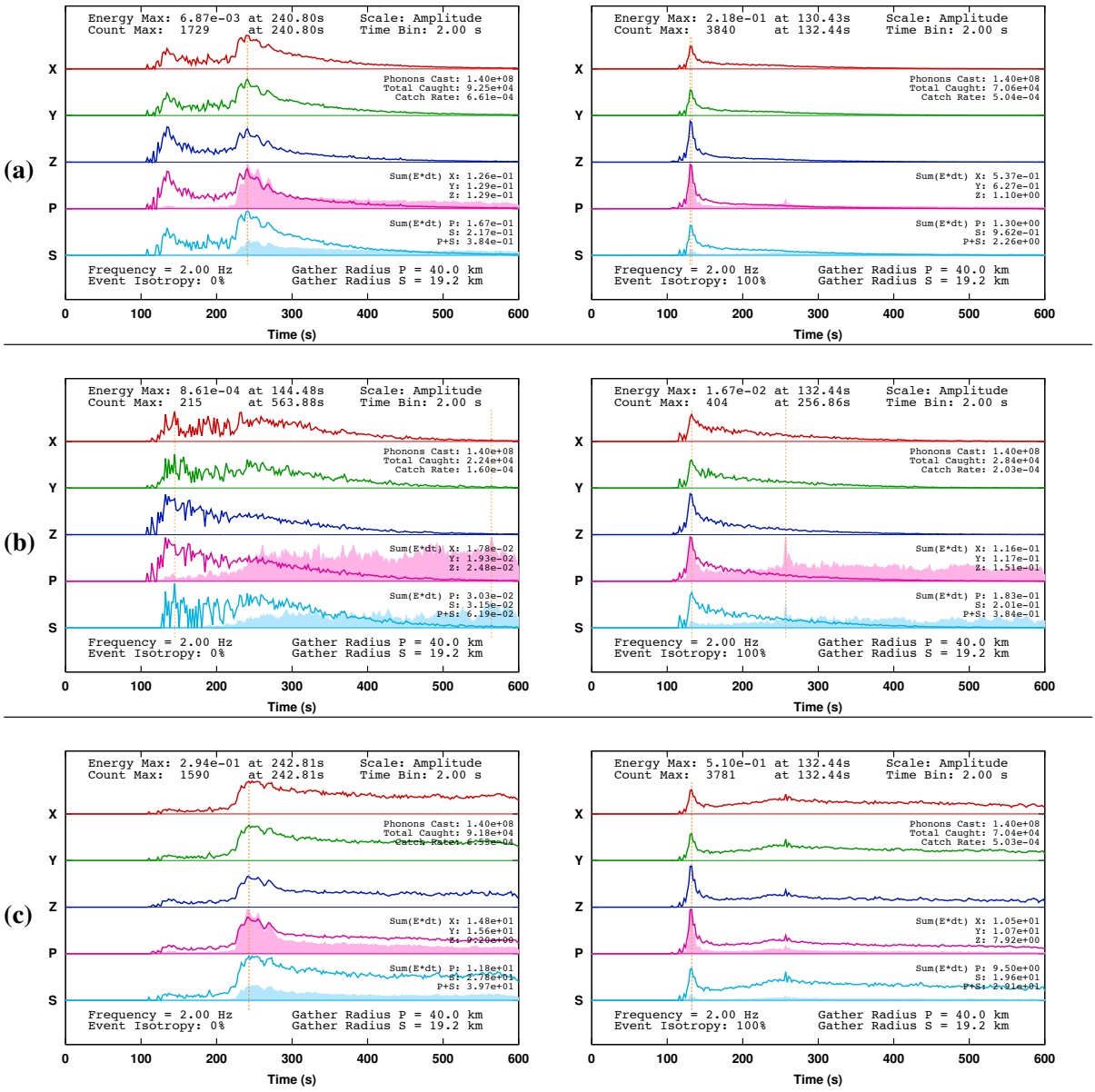

Figure 4.4: Envelopes produced by RADIATIVE3D for a shallow-focus earthquake (left) and explosion (right) as recorded by a virtual seismometer at 799 km range along the Lop Nor to MAK path in our Lop Nor model. Traces are shown for components of motion NS (Y), EW (X), and vertical (Z). Additional channels P and S denote instantaneous polarization mode of phonons arriving at the receiver. Trace amplitudes are proportional to the square root of the per-area per-time energy flux rate, decomposed by directional channel (X, Y, Z) or by polarization state (P, S). Shaded area under P and S curves represents raw phonon capture count, which neglects intrinsic attenuation effects and is not square-rooted, and serves a primarily diagnostic purpose. Annotations appear on each plot indicating parameters controlling the simulation and statistics describing the output. Vertical dotted red lines give the location in time of the channel-summed energy maximum and the phonon capture maximum, which overlap in some envelopes. The maxima values and time coordinates are also listed at the top of each figure. The bottom left corner of the figure includes the frequency of the run (in this case 2 Hz) and the isotropy of the moment tensor representation of the source (0% indicates earthquakes, 100% indicates explosions). Phonon statistics on the right side of the figure include the total number of phonons cast during the simulation (140 million), the total phonons caught at the location, and the catch rate. Also listed on the right side is the sum of the energy captured, under the assumption that each phonon departs the event source with unit energy. The total energy across all channels is indicated as P+S. The time bin width in the above simulations is 2.0 seconds, indicated in the upper right corner, or 4 cycles at 2.0 Hz. Row **(a)**: reference synthetics chosen as a baseline of comparison for experiments varying heterogeneity parameters. (See section 4.) Row **(b)**: velocity perturbation ϵ increased from 4% to 8%. Row **(c)**: synthetics with effects in intrinsic attenuation disabled.

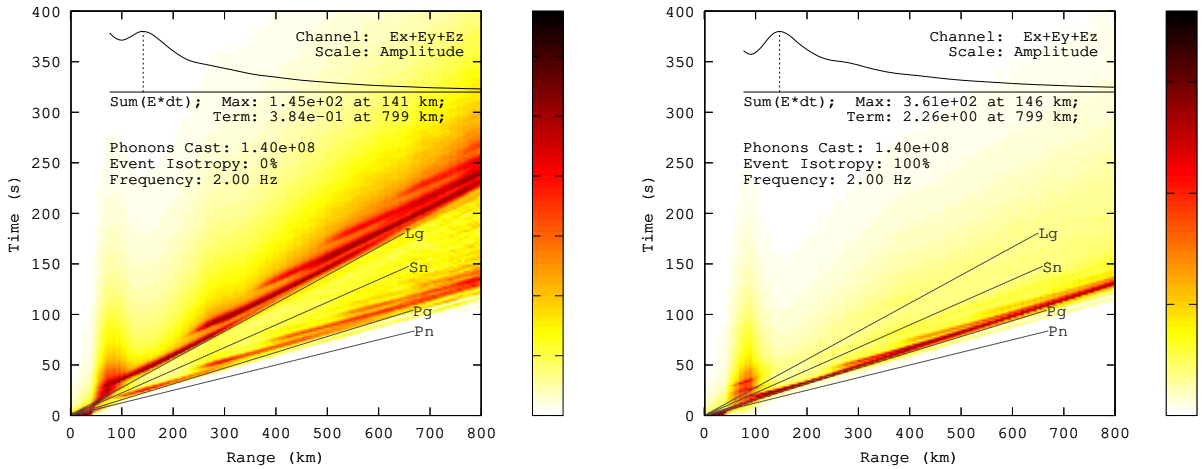

Figure 4.5: Travel time curves produced by RADIATIVE3D for shallow focus earthquake (left) and explosion (right), corresponding to the envelopes in row (a) of Fig. 4.4. Image density is proportional to the square root of energy flux arriving on all three axes, thus depicting an amplitude-like signal. A range-varying normalization curve is applied to the amplitudes so that the seismic phases remain distinct at all ranges. The normalization point is the midpoint between the average value and the peak value of the envelope at each distance range, and provides for good visual separation of phases. An overlay plot shows the time-integrated energy flux plotted on a square-root scale against range to show the overall amplitude decay with distance, omitting the very near range. Annotations identify the maximum of this integrated energy value and the value at the terminal range. Additionally, as with the envelope plots, the number of phonons cast, the frequency of the simulation, and isotropy of the event source are noted. Phase markers denoting the group velocities of the four regional phases are also shown for reference.

from 2000 through 2008. Los Alamos National Lab (LANL) has also constructed maps of regional wave propagation efficiencies in this region (Phillips et al., 1999). Lop Nor is located near the southeastern side of the Tian Shan, a region of moderate earthquake activity and contemporary horizontal compressive stress in the earth's crust, which can be an important factor in inducing tectonic release from underground nuclear tests in this region.

The Chinese station WMQ (Urumqi) is about 250 km (2.15°) from Lop Nor. Stations MAK and WUS are about 760 km (6.85°) from Lop Nor. For the earthquake and explosion data we use seismograms from events downloaded from IRIS-DMC.

Figure 4.7 shows some waveform examples from the Lop Nor region. The data

come from an explosion at the Lop Nor site as recorded at station MAK at great circle distance 6.85° and an earthquake in the same area recorded at both MAK and WUS. WUS is approximately at the same distance from Lop Nor as MAK but at a different azimuth. Figure 4.7 shows data band passed between 1-2 Hz and between 6-8 Hz for each recording. Not only are there differences between the earthquake and explosion data at MAK, there are also differences between the earthquake traces at MAK and WUS in the time windows commonly used to measure Pn/Lg and Pg/Lg amplitude ratios.

Using known elevations of Lop Nor and seismic stations MAK and WUS, along with Moho depths from the Cornell Moho model (`http://atlas.geo.cornell.edu/geoid/imagegrid.html`) and layer profiles from CRUST 2.0 (Laske et al., 2011) at those same locations, we located and oriented a set of five crust layers (sediments, upper, middle, and lower crust, and top layer of the mantle). Additionally, we defined an additional 16 mantle layers from AK-135-F (Kennett et al., 1995) and regionalized perturbations (Gudmundsson and Sambridge, 1998) to a depth of 859 km. These layers served as an initial deterministic background model (Fig. 4.8) in which to run synthetics.

4.4.2 Statistical model

To determine our statistical model for the Lop Nor region, we first performed a series of experiments to examine the sensitivity of regional phases to the shape of the heterogeneity spectrum. Results of these experiments are displayed as coda envelopes by component of motion and by the sum of the relative contributing phonon states (P or S) at receiver (Fig. 4.4). Spectral shape parameters were varied for a von Kármán spectrum. The advantage of this spectrum is that it can incorporate a more realistic medium behavior over a broad band of wavenumbers, reproducing a fractal-type behavior be-

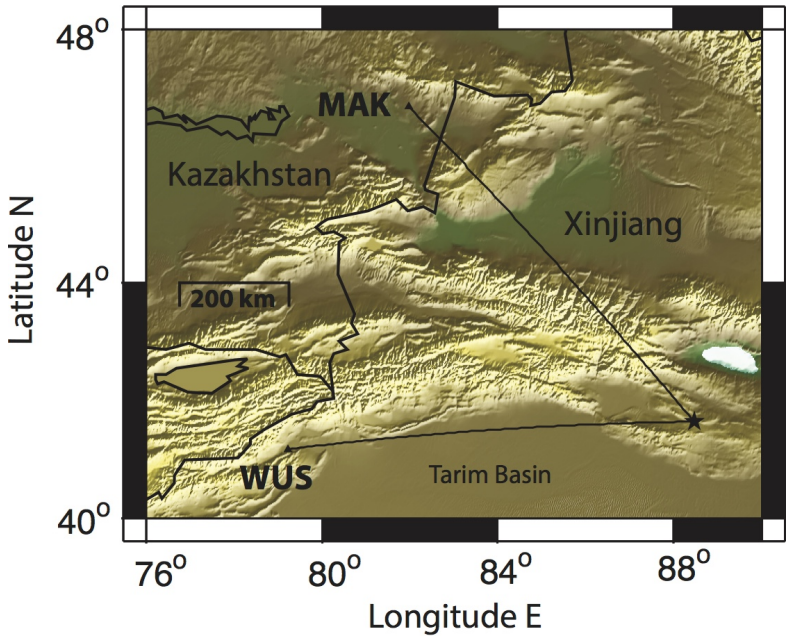

Figure 4.6: Lop Nor test site and paths to regional seismic stations MAK and WUS on which we have concentrated modeling tests.

yond a corner wavenumber (Margerin and Nolet, 2003). The parameters varied are: the fractional fluctuation ϵ of seismic wave velocities; a parameter ν controlling the density perturbation as a factor multiplying the P velocity fluctuation; a scale length a that controls the wave number corner; and a von Kármán Hurst order number κ that controls the slope of the power spectrum after its corner. Following Sato et al. (2012), who simplified formulas for scattering radiation patterns by assuming ϵ is identical for P and S waves, we take $\epsilon = \frac{\Delta V_{\mathrm{P}}}{V_{\mathrm{P}}} = \frac{\Delta V_{\mathrm{S}}}{V_{\mathrm{S}}}$, equivalent to assuming $d \ln V_{\mathrm{S}} / d \ln V_{\mathrm{P}} = 1$. Experimental verifications of this assumption are few. From a local array above the Tonga subduction zone, Koper et al. (1999) estimated $d \ln V_{\mathrm{S}} / d \ln V_{\mathrm{P}}$ to be in the range 1.1 to 1.5 at scale lengths on the order of 10 to 100 km. In the lower mantle at larger scale lengths (~1000 km), $d \ln V_{\mathrm{S}} / d \ln V_{\mathrm{P}}$ has been estimated to be > 2.5 (Romanowicz, 2001).

The sensitivity of regional phase codas to heterogeneity parameters can be understood by examining the behavior of the mean free path (MFP) and the dipole projection

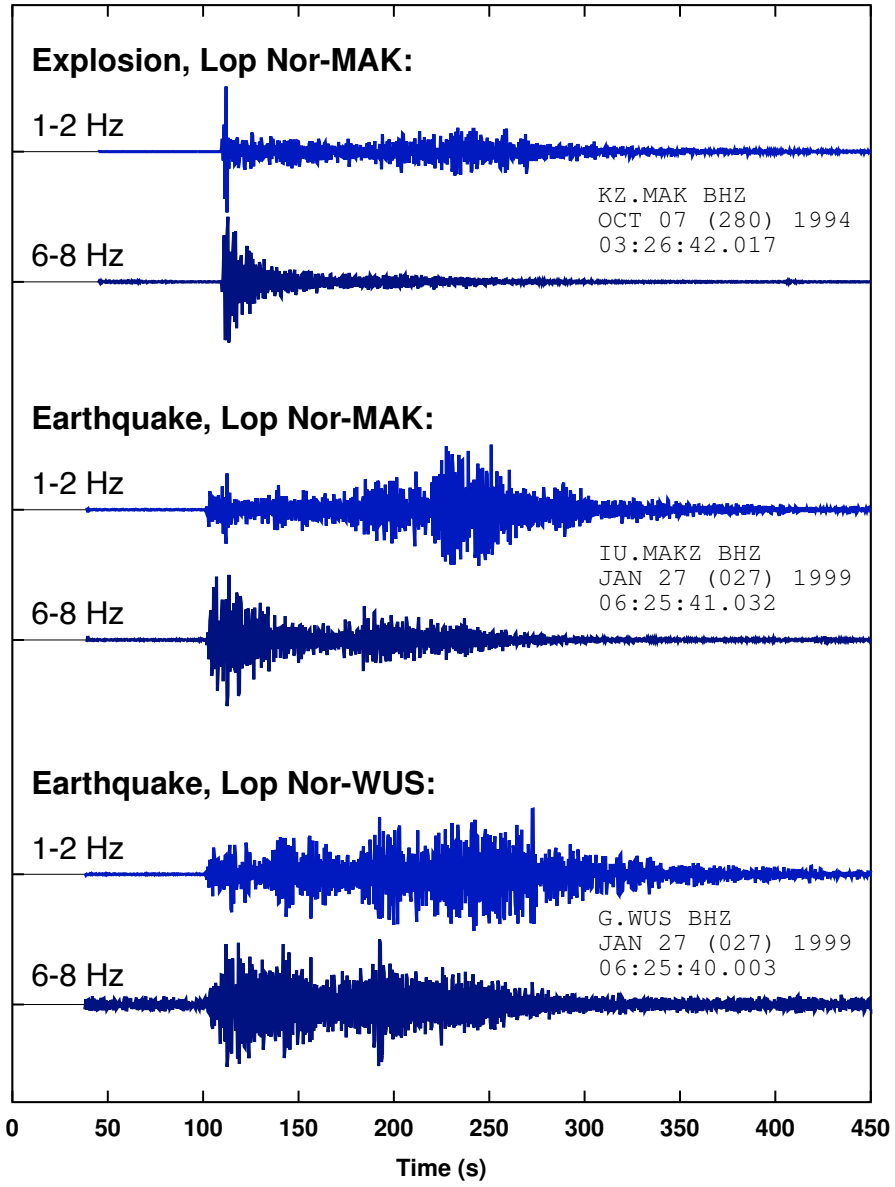

Figure 4.7: Vertical component band-passed data recorded at stations WUS and MAK in the Lop Nor region.

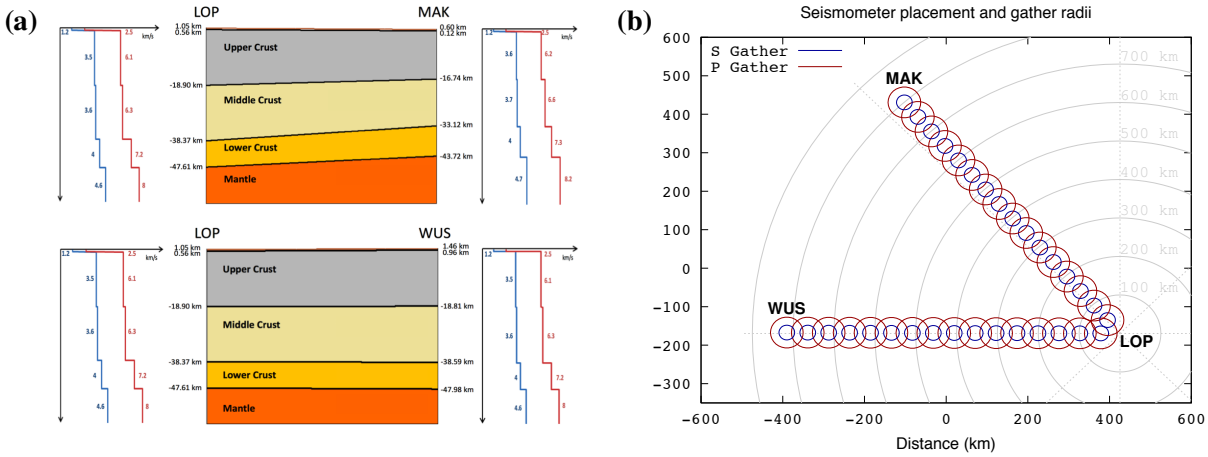

Figure 4.8: (a) Simplified Lop Nor Earth model composed of layers of uniform background velocity separated by planar tilted interfaces oriented to match depth profiles at Lop Nor, station MAK, and station WUS. A thin sediment layer (0.5 km) is included and sits on top of three crust layers extending to a depth of ~ 45 km, and 16 mantle layers down to a depth of 859 km. (b) Map view showing relative locations of Lop Nor, MAK, and WUS in model coordinates and two virtual seismometer arrays represented by gather-radius circles. Each array consists of 160 evenly spaced seismometers of which every tenth one is shown. Results presented here will focus on the LOP to MAK path.

(DP), while varying a single parameter and holding the others constant. The MFP and DP calculations provide an easy way to understand the general effects of the parameters. The MFP reports how far a phonon will travel, on average, before it encounters a scattering event. Longer MFPs mean less scattering. The dipole projection is simply the mean cosine of the angular deflection of a phonon path after a scattering event. It varies from -1 to 1. A value of 1 means it is 100% likely to continue in its forward direction, and a value of -1 means it is 100% likely to be totally scattered backwards. Intermediate values indicate wide deflection angles and/or a balance of forward and back-scattering.

In Figure 4.9, the effects of varying each parameter on MFP are read on the left side y-axis as solid lines, and the effects on DP are read on the right side y-axis as dashed lines. The parameter being varied is plotted on the x-axis. The red lines show the effect of scattering on the P-wave phonons, and the blue lines show S-wave phonons.

	ν	ϵ	a	κ	Q_{S}
Sediments	0.8	0.01	0.25 km	0.2	50
Crust	0.8	0.04	0.2 km	0.3	1000
Mantle	0.8	0.008	0.2 km	0.5	300

Table 4.1: Reference heterogeneity parameters used for synthetic comparisons in the simplified Lop Nor Earth model.

For each parameter, synthetic envelopes are computed at 2 Hz and presented in the following subsections to assess the impact of each individual parameter. Comparison is made to a common reference synthetic, shown in row (a) of Fig 4.4, with parameters given in Table 4.1. Q_{P} is assumed to greater than Q_{S} by a factor of approximately $9/4$, consistent with an assumption of viscoelastic attenuation purely in shear and a Poisson's ratio of $1/4$ (Anderson, 1989).

4.4.2.1 Magnitude of velocity fluctuation ϵ

The dashed lines in Figure 4.9(a) reflect a constant S-wave dipole projection of 0.48 and a constant P-wave dipole projection of 0.18. For sufficiently small fluctuations and small scale length, varying ϵ has essentially no effect on the scattered phonon's preferred direction of travel after scattering because the magnitude of ϵ does not affect the shape of the scattering radiation pattern at a scattering event. On the other hand, there is an apparent inverse quadratic decrease in the MFP for both P and S phonons for this range of increasing velocity perturbation. We should expect to see increased coda production for both S and P waves in the synthetic envelopes with increased ϵ.

Fig. 4.10 compares synthetic z-component envelopes at 2.0 Hz for crustal ϵ values of 0%, 4%, and 8% for an earthquake simulation and 4% and 8% for an explosion simulation. Fig. 4.4(b) shows envelopes for all components at ϵ = 8% for the earthquake and explosion simulations, which can be compared against row (a) containing the ϵ = 4% reference simulations. For the earthquake, the maximum energy and maximum

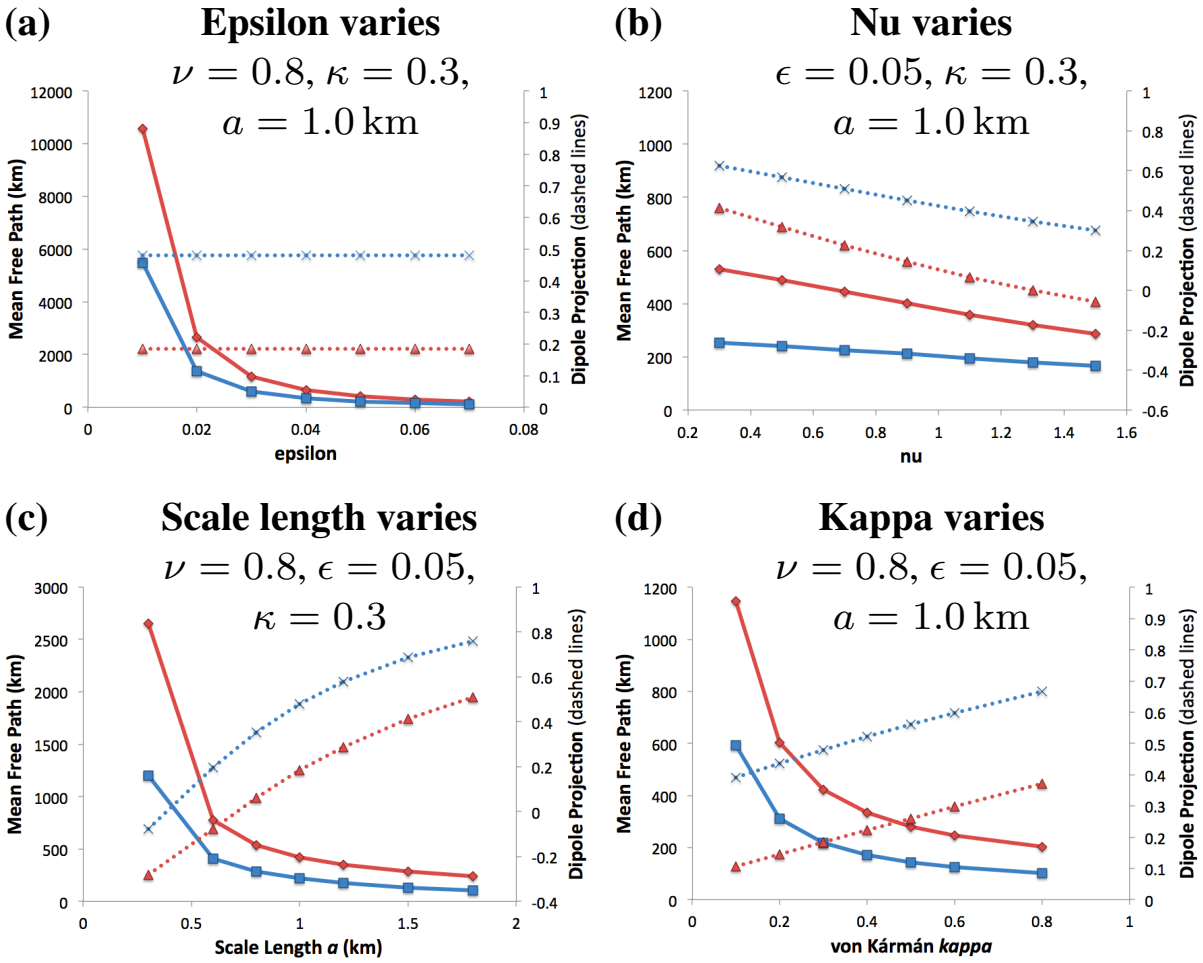

Figure 4.9: Effects of heterogeneity parameters ν, ϵ, a, and κ, on mean free path MFP (average distance between scattering events) and dipole projection DP (average cosine of deflection angle) for 1.0 Hz propagation in a background medium having P and S velocities $v_{\mathrm{P}} = 6.93\,\mathrm{km/s}$ and $v_{\mathrm{S}} = 4.00\,\mathrm{km/s}$. The DP value serves as a measure of scattering directionality, with positive values indicating dominant forward scattering, negative values dominant back-scattering. Fixed parameter values are selected in the neighborhood of values used for the studies in this paper. Blue series indicates trends for S propagation and red for P propagation.

phonon count in the reference occur at the time of the Lg phase (~ 241 s). For the explosion, the maximum energy and maximum phonon count in the reference occur within the P coda (~ 130 s). We see a number of effects in the seismic envelopes caused by the change in the heterogeneity parameter, including change in total energy and phonons arriving at the receiver, change in maximum energy, onset of P and Lg phases, shape of the direct phase arrival, and the coda following the direct arrival.

The combined results of the MFP/DP plots and synthetic envelopes show that with higher velocity perturbations, the phonons have smaller mean free paths, thus encountering more scattering events. As velocity fluctuations increase, the arrival time of the maximum energy shifts from the Lg arrival window to the P arrival window.

The scattering caused by the increase in the velocity perturbation produces a marked redistribution in energy, stretching it out over a longer period of time. This is represented by a slower decay of coda envelopes, the broadening of the pulses, and a pronounced delay in the phonon arrivals (shaded areas in the P and S channels, Fig. 4.4) These results reflect the increased production of scattered P and S energy as well as conversions between and P and S energy, particularly for the explosion. Without scattering, almost all of the explosion energy is in the P arrival. With the scattering, in addition to coda energy following the P-arrival, there is significant energy arriving at the time we would expect to see Lg. This delayed energy, however, is reflected in a slower coda envelope decay following the P phases, which cannot easily be mistaken for the typical Lg coda envelope observed from earthquakes.

4.4.2.2 Magnitude of Density Perturbation ν

The density perturbation ν is a multiplier of the velocity perturbation: $\frac{\Delta\rho}{\rho} = \nu\frac{\Delta V_{\mathrm{P}}}{V_{\mathrm{P}}}$. Figure 4.9(b) shows the effects of density perturbations from 0.3 to 1.5 on MFP and DP. Shearer and Earle (2008) take $\nu = 0.8$ for small-scale heterogeneity (1-10 km). For

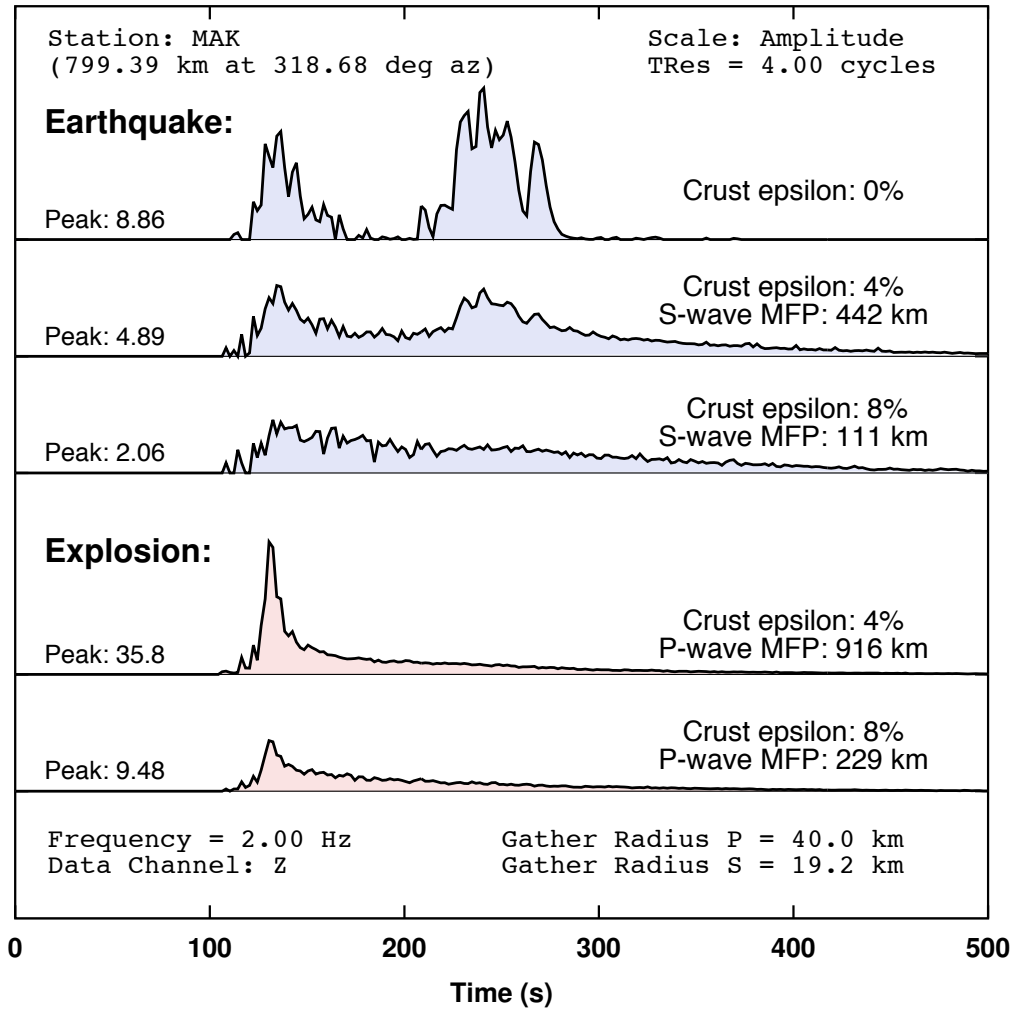

Figure 4.10: Effects of velocity perturbation ϵ on earthquake and explosion z-component coda envelopes. The peak amplitude value is noted for each trace, as is the ϵ value used in the crust layers and the resulting mean free paths in the middle crust layer for each case.

large-scale (>1000 km) structure in the mantle, geodynamicists take ν on the order of 0.2 or less because large values cannot be sustained by buoyancy (Forte and Woodward, 1997).

Higher values of ν produce a shorter mean free path. In contrast to the effect of increasing velocity variations, the effect of increasing density variations is a linear, rather than inverse quadratic, decrease in mean free path as density perturbation increases. The higher values of ν also lower the dipole projection, which means the phonons are scattered further away from the forward direction of travel. This suggests that ν variations will be important in controlling the attenuation of the peak amplitudes of regional phases defined from narrow windows of group velocity.

In the heterogeneity parameter neighborhood that we investigated, the backscattering effects on coda envelopes resulting from a doubling of ν from 0.8 to 1.6 were much less pronounced than the effects observed from our ϵ variations; hence, we do not show synthetic envelopes. Maximum energy occurs at the same time as the reference, and the maximum phonon count occurs only slightly later (~ 255 s). The P onset is sharper and of lower amplitude, but the effects on coda envelopes of plausible density perturbations are much weaker than those of plausible velocity perturbations. In general, the influence of density variations is to produce more scattered energy than for velocity variations alone. Nonetheless, the ability to adjust ν could be important in other seismic coda studies, such as those involving partial melt (Hong et al., 2004).

4.4.2.3 Scale length a

Figure 4.9(c) shows the effects of scale length variations from 0.5 to 12 km on MFP and DP. For the velocities and frequency (2 Hz) used in coda envelope simulations, the wavelength in the crust is 2 km for the S waves and 3.4 km for P waves.

Fig. 4.11 shows synthetic envelopes for a range of scale lengths and travel time

curves for a subset of lengths from 0.1 km to 12 km. These values were prescribed in the crust layers, and the results allowed us to examine the effects of the scale length being greater than or smaller than the wavelength. The mean free path decreases as the scale length increases, but the dipole projection asymptotically approaches 1 (forward scattering). Not surprisingly, the competition between these two effects results in the strongest coda production when the scale length is on the order of the wavelength. When the scale length is much smaller, there are too few scattering events to significantly affect waveform shape. When the scale length is much longer than the wavelength, scattering events become frequent, but are non-deflectionary, and cause only minimal time lags with reference to the un-scattered trajectories, resulting primarily in a smoothing of the waveform but not significant coda generation.

4.4.2.4 Hurst Parameter κ

The magnitude of the fluctuation power spectrum for a von Kármán medium is flat with wavenumber in the domain $ka \ll 1$, and decays as a negative power of wavenumber in the domain $ka \gg 1$. The Hurst parameter κ controls the decay rate at scales smaller than the corner scale a, in the $ka \gg 1$ domain. The von Kármán medium is characterized by heterogeneities that are "rougher" at small length scales than the Gaussian medium, in which the power spectrum decays much more rapidly, in the $ka \gg 1$ domain (Frankel and Clayton, 1986; Sato et al., 2012).

Figure 4.9(d) shows the effects of κ variations from 0.1 to 0.8 on MFP and DP. As κ increases, the MFP decreases, which causes scattering delays in the energy arrival. As the slope of the heterogeneity spectrum flattens below the corner wavenumber, the scattering is increasingly in the forward direction even though scattering events are more frequent. The effect of increased scattering at higher κ will have less effect on redistribution of energy and stretching of coda envelopes, but may have a stronger ef-

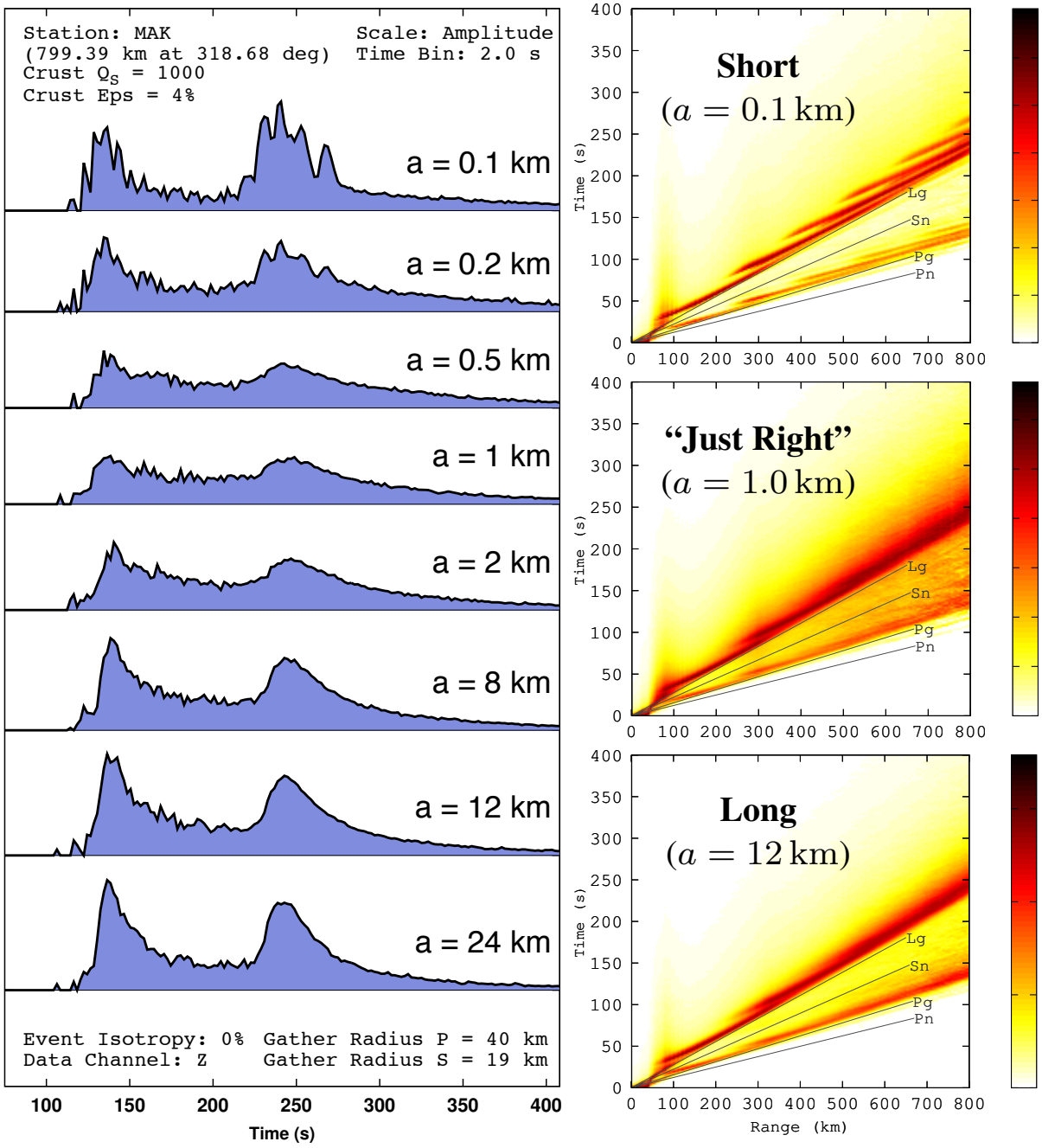

Figure 4.11: Simulated effects on earthquake seismograms of a von Kármán heterogeneity spectrum with varied scale length a applied in the crust layers (from just below sediment layer down to ~ 45 km depth). Note that the coda of individual multiple Moho-reflected S waves comprising Lg overlap as the scale length increases, and that coda production is optimized when the scale length is on the order of the wavelength.

fect on equilibrating energy on the three components of motion due to a more frequent sampling of heterogeneity radiation patterns that control polarization and wave type (P or S). The heterogeneity power, however, will decrease faster at wave numbers above the corner wave number for higher κ. We found the effect of κ variation to be minor in our experiments at distances beyond several hundred kilometers and at frequencies between 2 to 4 Hz. At shorter distances and higher frequencies, however, Saito et al. (2002) and Sato and Fehler (2016) have found strong sensitivity of coda shape to κ. Since visible effects of κ are not easily discernible in the distance ranges and frequencies we examined, we do not show synthetics for this experiment.

4.4.2.5 Intrinsic Q effects

RADIATIVE3D allows us to treat intrinsic viscoelastic attenuation separately from scattering to help determine their relative contributions to the total attenuation of peak coda amplitudes or to separate their contributions to measured coda-Q's. Figure 4.4(c) shows coda envelopes modeled in the absence of intrinsic attenuation, and can be compared against the reference envelopes in 4.4(a) that included Q values as specified in Table 4.1. For the earthquake, the 2 Hz total integrated energy without Q^{-1} included is about 100 times that of the reference envelope, and the peak energy value is about 50 times that of the reference. The phonon capture is about the same. The effect of Q^{-1} is to reduce the amount of energy in each phonon as a function of time traveled, but it does not reduce the number of phonons reaching the target. Perhaps more importantly the test also shows that not adding intrinsic attenuation results in the coda energy being unrealistically extended in time. Accurate models of intrinsic Q in the crust and just beneath the Moho are essential for proper modeling of Sn and Lg. In future work we will examine tradeoffs between scattering parameters and intrinsic attenuation and test the multiple lapse-time window analysis method (Fehler et al., 1992;

Hoshiba, 1993) for separating intrinsic attenuation from apparent scattering attenuation.

An interesting artifact appearing in the explosion coda of Fig. 4.4(c) is a small spike at about 255 s. On the basis of its measured slowness, travel-time, and polarization, we believe this spike originates from P to SV scattered phonons near the source that are then reflected from the 410 discontinuity. This S410S wave is a small-amplitude, pre-critical reflection at this range, but its amplitude increases with range beyond 500 km corresponding to incidence angles at which the SV to P transmitted wave is no longer excited beneath the 410 discontinuity. These pre-critically reflected phonons would normally be sufficiently attenuated so as not to contribute to the resulting envelope. In in the absence of attenuation these phonons can make visible smaller amplitude phases normally lost in the scattered coda.

4.4.3 Surface layer effects

A highly heterogeneous, strongly scattering, sediment layer may affect regional phase coda (Baumgardt, 2001), particularly for shallow emplaced explosions. Since detailed information on the velocities, thickness, and lateral variation of the sediment layer is not easily available for this region, we conducted some experiments on its possible effects. Fig. 4.12 shows synthetic envelopes exploring the effects of a 0.5 km thick sedimentary layer with deterministic and statistical properties given in Table 4.2. The first row of Fig. 4.12 shows synthetics very similar to the reference synthetics of Fig. 4.4(a), and includes the sedimentary layer. The only change from the reference model was an increase in sediment layer velocity perturbation ϵ from 1% to 4%, and a corresponding reduction in scattering MFP in this layer from 1818 km to 114 km for P waves and 627 km to 39 km for S waves. Although this is a large increase in the rate of scattering in this layer, the layer is thin and the effects on coda shape are subtle. In the second

Layer	v_P (km/s)	v_S (km/s)	density (g/cm^3)	Q_P	Q_S	ϵ	MFP_P (km)	MFP_S (km)
Sediments	2.50	1.20	2.10	163	50	0.04	114	39
Upper Crust	6.13	3.53	2.75	2262	1000	0.04	826	411

Table 4.2: Deterministic and statistical properties and resulting mean free paths of sediment and upper crust layers in the models exploring effects of the sediment layer on coda shape (Fig. 4.12). Heterogeneity parameters ν, a, and κ are unchanged from those listed in Table 4.1 for the reference synthetics.

row of coda envelopes in Fig. 4.12, the sediment layer has been inactivated by replacing its properties with those of the upper crust layer immediately below it, such that the upper crust in this model effectively extends to the surface. This eliminates both the additional scattering in this layer and the refraction, reflection, and P/S conversions that would occur at the crust–sediment interface.

For both the earthquake and the explosion, the most obvious effect of the low velocity sediment layer is on the P/Lg amplitude ratio. Although the differences between earthquake and explosion envelopes are strong in both cases, the effect of the sediment layer will be to slightly reduce the effectiveness of the P/Lg discriminant. There is an apparent tendency for the sediment scattering layer to equilibrate energy on all three components of motion (X, Y, Z).

4.4.4 Pn and Sn

High frequency Pn and Sn are traditionally thought of as head waves traveling just beneath the Moho discontinuity. Early attempts to model high frequency Pn and Sn as classical head waves failed because the amplitude of a classical head wave decays with frequency (ω) as $1/\omega$. These phases are now recognized as interference head waves (Červeny̌ and Ravindra, 1971). Interference head waves have a representation as series of body waves that are multiply reflected along the underside for either a Moho following Earth's curvature or for velocities that increase with depth beneath the Moho. Our

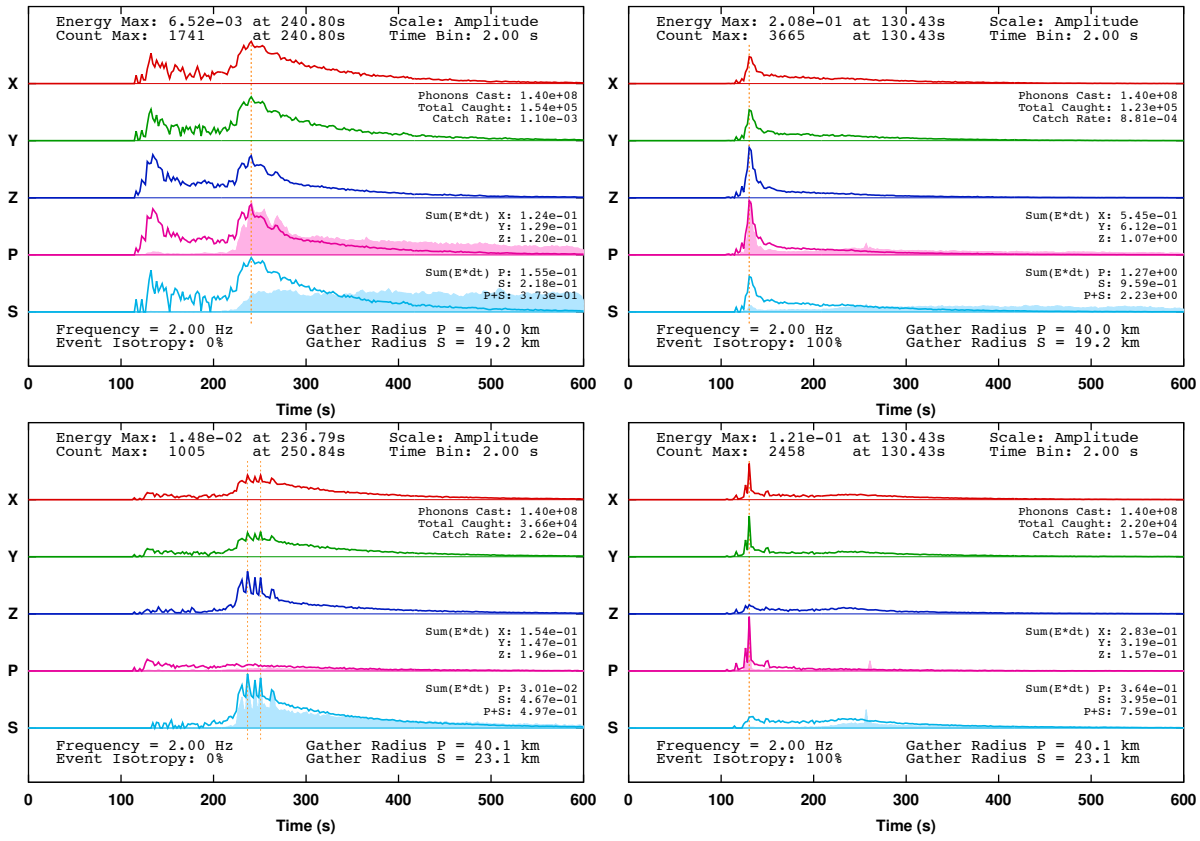

Figure 4.12: Synthetic envelopes for sediment layer effects. Top left: earthquake simulation with sediment layer included; top right: explosion with sediment layer; bottom left: earthquake without sediment layer; bottom right: explosion without sediment layer.

	ν	ϵ	a	κ	Q_S
Sediments	0.8	0.01	0.25 km	0.2	50
Crust	0.8	0.04	0.2 km	0.3	1000
Transition	0.8	0.008	0.2 km	0.5	2000
Mantle	0.8	0.008	0.2 km	0.5	300

Table 4.3: Heterogeneity and Q parameters for simulations in models involving a Moho transition region (Figs. 4.13–4.16).

initial experiments assumed a flat earth and homogeneous layers, separated by planar tilted interfaces. In these models energy does not return from the mantle except as scattered waves. With a series of stair-step discontinuities, we have simulated the effects of Earth curvature via an earth-flattening transformation and positive velocity gradients with decreasing radius (Fig. 4.13). These modifications allow Pn and Sn to return to the surface after being multiply reflected by and scattered beneath the Moho. Table 4.3 lists the values of the heterogeneity and Q parameters used in this model. These are similar to the reference parameters used in the heterogeneity parameter sensitivity study, but with the addition of a transition layer at the Moho. Envelopes were synthesized for the 2003-03-13 southern Xinjiang earthquake recorded at MAK for this Moho model. Fig. 4.14 shows the results of this experiment with scattering from the reference statistical model turned on and off. A sharp Pn arrival is visible in the coda. Sharp arrivals preceding Lg, which can be interpreted as Sn, are best visible in the envelopes having scattering turned off.

Fig. 4.15 compares the synthetic z-component envelope that includes scattering against the recorded earthquake. The approximate arrivals from the four regional phases are marked. There is good agreement in arrival time and relative amplitude for the Pn, Pg, and Lg phases. The Sn phase is much smaller in the synthetic compared to the data. We believe that reducing the intrinsic S attenuation may allow more of the Sn energy to show up for this phase.

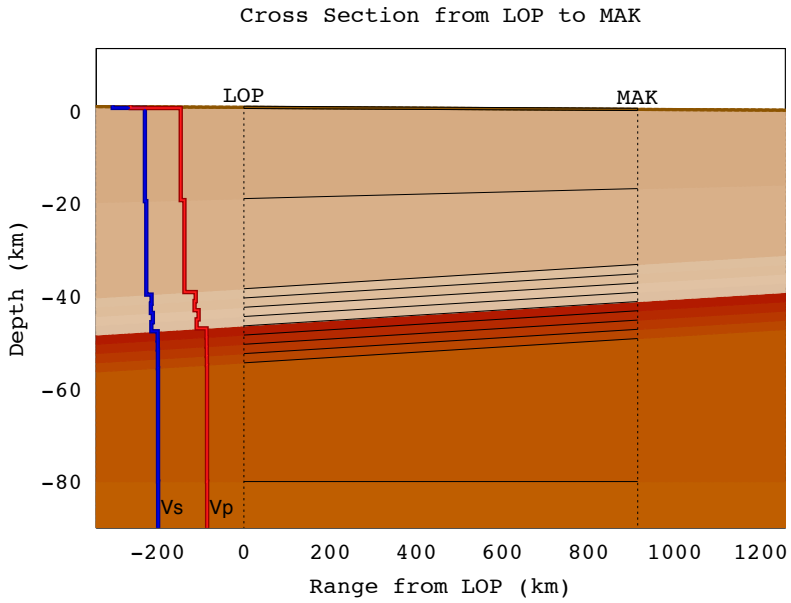

Figure 4.13: Earth model having a Moho transition region at the base of the crust and a very slight stair-step ramp at the top of the mantle for a path from a southern Xinjiang earthquake to station MAK. Depth dependences of P and S velocities are also shown. For simulations that included scattering, ϵ was 4% in the crust and 0.8% in the transition region and mantle. Simulations performed in this model had an earth-flattening transformation applied on input to the software to enhance effects of the stair-step gradients and mimic effects of Earth curvature. There is a thin (0.5 km) low velocity sedimentary layer at the top of the model.

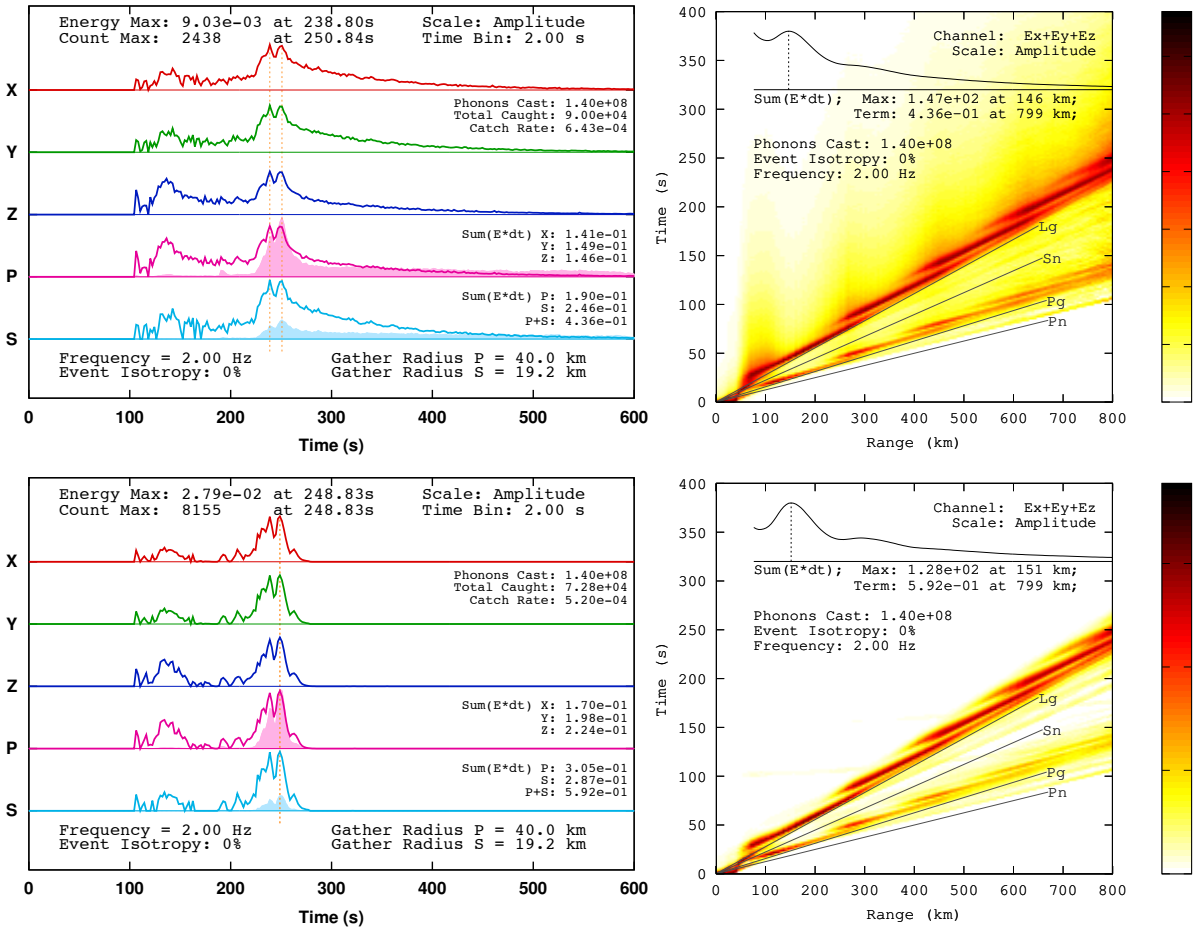

Figure 4.14: Top: Synthetic envelopes for the Moho transition model (Fig. 4.13) for the path to station MAK from a focal mechanism patterned after the 2003-03-13 southern Xinjiang earthquake (strike, dip, rake: 125°, 40°, 90°; depth 6 km) with scattering predicted from the heterogeneity parameters in Table 4.3. Bottom: synthetic envelopes for the same path with scattering turned off.

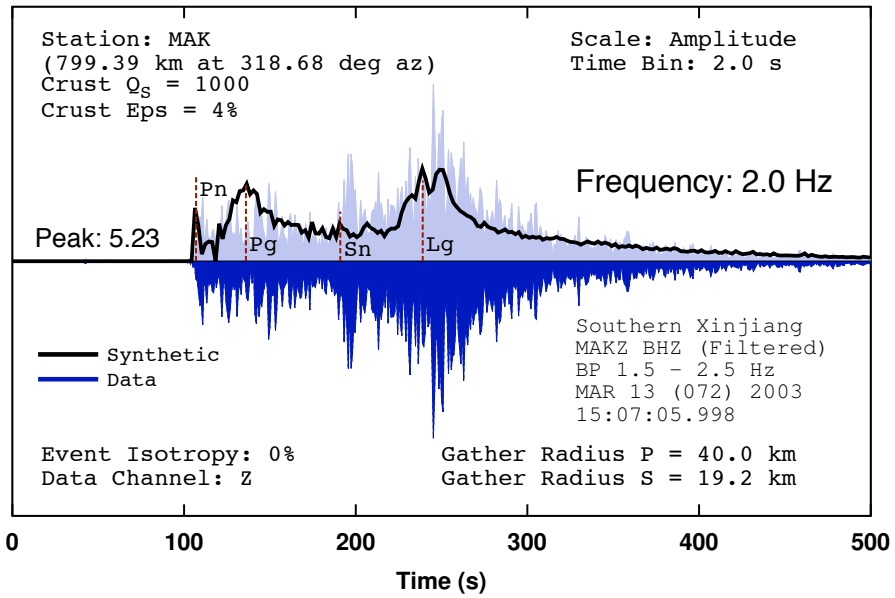

Figure 4.15: Comparison of data with a 2.0 Hz synthetic coda envelope for a model having a Moho transition layer. Data is band passed from 1.5 to 2.5 H, enveloped, and mirrored across the x axis. The approximate arrivals of the regional phases are marked.

4.4.5 Synthetics compared with data by frequency band

RADIATIVE3D is run at a single frequency and can create simulated seismogram envelopes at any frequency. This allows analysts to interpret the structural or source origin of frequency-specific effects on narrow band passed seismic traces.

There is now a substantial body of empirical evidence that regional P/S ratios provide poor discrimination below some frequency, typically about 2 to 3 Hz, and useful discrimination at higher frequencies (e.g., Fisk, 2006). Hence, in Figure 4.16 we compare computed envelopes against narrow band passed data at 2, 3, and 4 Hz.

The synthetic traces presented Fig. 4.16 do not include the effects of scattering (the velocity variation ϵ was set to 0%), and thus the only frequency-dependent effect simulated was that of intrinsic Q. Except for the more time-extended Lg coda in the data due to the effects of multiple scattering, we see a rough general agreement between the synthetics and the data in: (1) the apportionment of energy between the Pg and Pn window and the Lg windows, favoring Lg at 2.0 Hz to favoring Pg and Pn at 4.0 Hz;

and (2) the overall amplitude decay from the 2.0 Hz to 4.0 Hz bands. Our modeled Q value is close to the coda Q values (731 to 951) predicted by Martynov et al. (1999) in this frequency band from observations in the nearby Tian Shan region. The extent of the waveform agreement also suggests that in at least this specific region, frequency band, and range, that intrinsic attenuation is more important than multiple scattering in controlling the peak amplitude decay of coda envelopes. In experiments not shown, we added moderate scattering but kept the same Q value, and found that this agreement was lost above 2.0 Hz. These results simply support that reported crustal Q values and their frequency dependence must be carefully examined across a sufficiently broad band to determine a depth and frequency parameterization of intrinsic attenuation that accurately removes the effects of scattering.

4.4.6 Tectonic release: regional propagation effects

We investigated the effect on high frequency regional phase propagation of explosion sources associated with components of tectonic stress release. These experiments were inspired in part by the work of Bukchin et al. (2001). That study jointly inverted P wave first motions and teleseismic Love and Rayleigh wave spectra for unconstrained moment tensors of earthquakes and nuclear tests in the Lop Nor region. The amount of tectonic release of nuclear tests was expressed as an angle given by the inverse tangent of the ratio of the isotropic to non-isotropic moment tensor components. The experimental series incorporated moment tensors reported by Bukchin et al. for the Lop Nor 1996-06-08 nuclear tests, although the source location used was that of the southern Xinjiang 2003-03-13 earthquake. Envelopes were synthesized for paths to stations MAK and WUS.

For this series of experiments, we used the moment tensor decompositions of several explosion events published by Bukchin et al. as our starting points. Although they

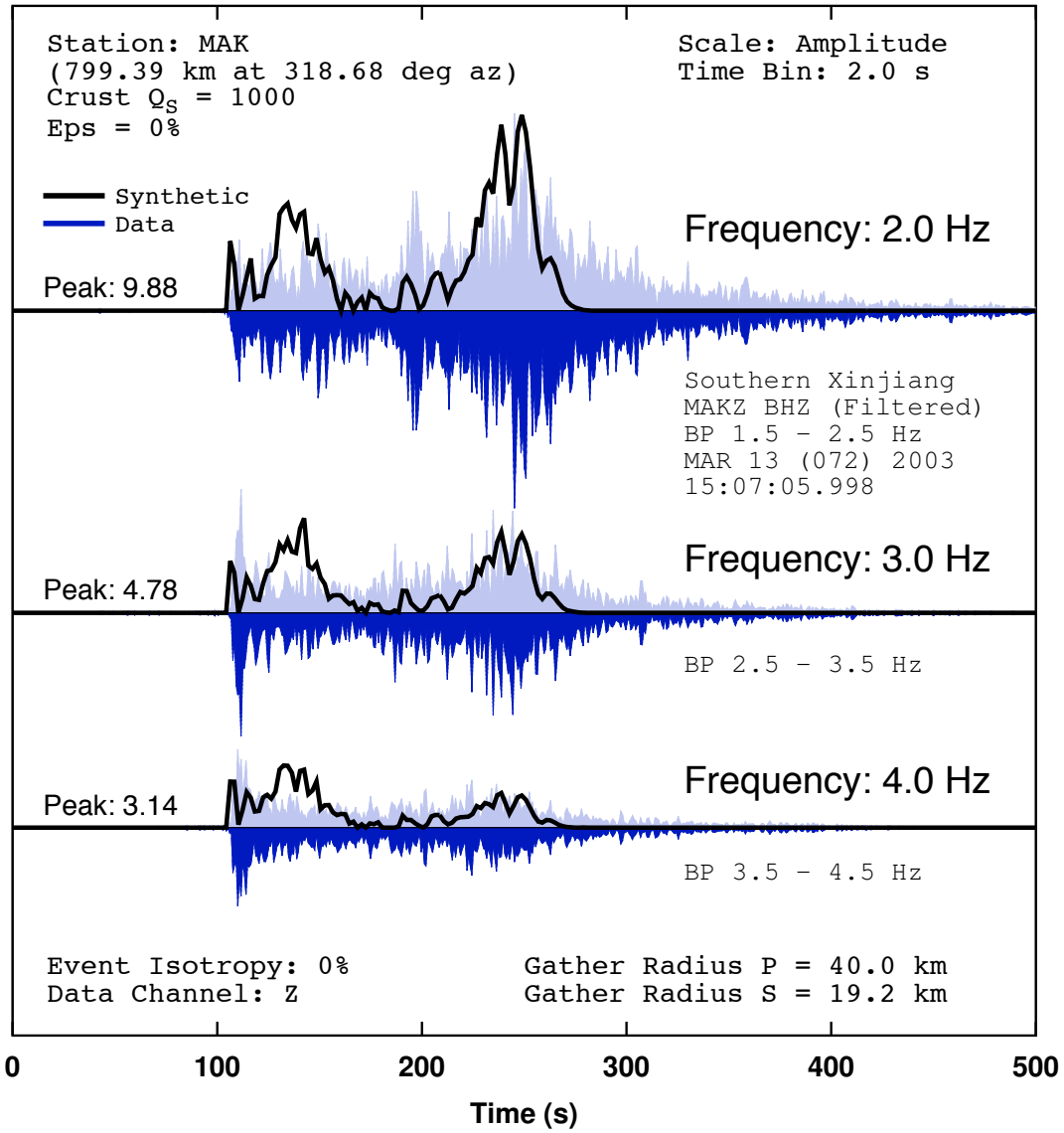

Figure 4.16: Synthetics compared against data recorded at station MAK for the 2003-03-13 earthquake for frequencies 2, 3, and 4 Hz. The relative changes in amplitude of the Pg and Lg phases produced by the synthetics agree quite well with the data.

treat the isotropic and deviatoric components as vertically separated, in these runs we treated them as co-located and coherent (meaning a single moment tensor specifies the entire source, as opposed to running the deviatoric and isotropic source radiation events separately and summing the synthetics.

Figure 4.17 shows an example of one of our event simulations compared to data recorded in several narrow band passed filters for 1 to 4 Hz. Note that the P/Lg ratio for the explosion with tectonic release is largest in the lowest frequency band of 1 Hz. This ratio, however, is also typical of that found for explosions without tectonic release at 1 Hz. This example is calculated using the source parameters of Bukchin et al. for an event that they determined to have the largest amount of tectonic release from teleseismic surface waves. In higher frequency bands, excitation of P coda is much larger than Lg, suggesting that event discrimination based on P/Lg ratios will not suffer in bands 2 Hz and higher. This behavior will be strongly affected by the intrinsic Q for shear waves in the crust. We have assumed a $Q_{\mathrm{P}} = 2300$ and $Q_{\mathrm{S}} = 1000$ in the crust. Even though the assumed Q_{S} is quite high, it is still low enough that any Lg trapped in the crust from the explosion is strongly attenuated at this distance range at frequencies 2 Hz and higher.

We finally note that our code does not include fundamental mode surface waves and our tests are for relatively long range (>100 km), and high frequency (>1 Hz). At this frequency and range surface waves are usually strongly scattered away by surface topography and near surface heterogeneity. Numerical simulations by Obermann et al. (2013) at ranges on the order of 10 km and have found that high frequency surface waves can provide valuable discrimination of source depth and possibly also of tectonic release.

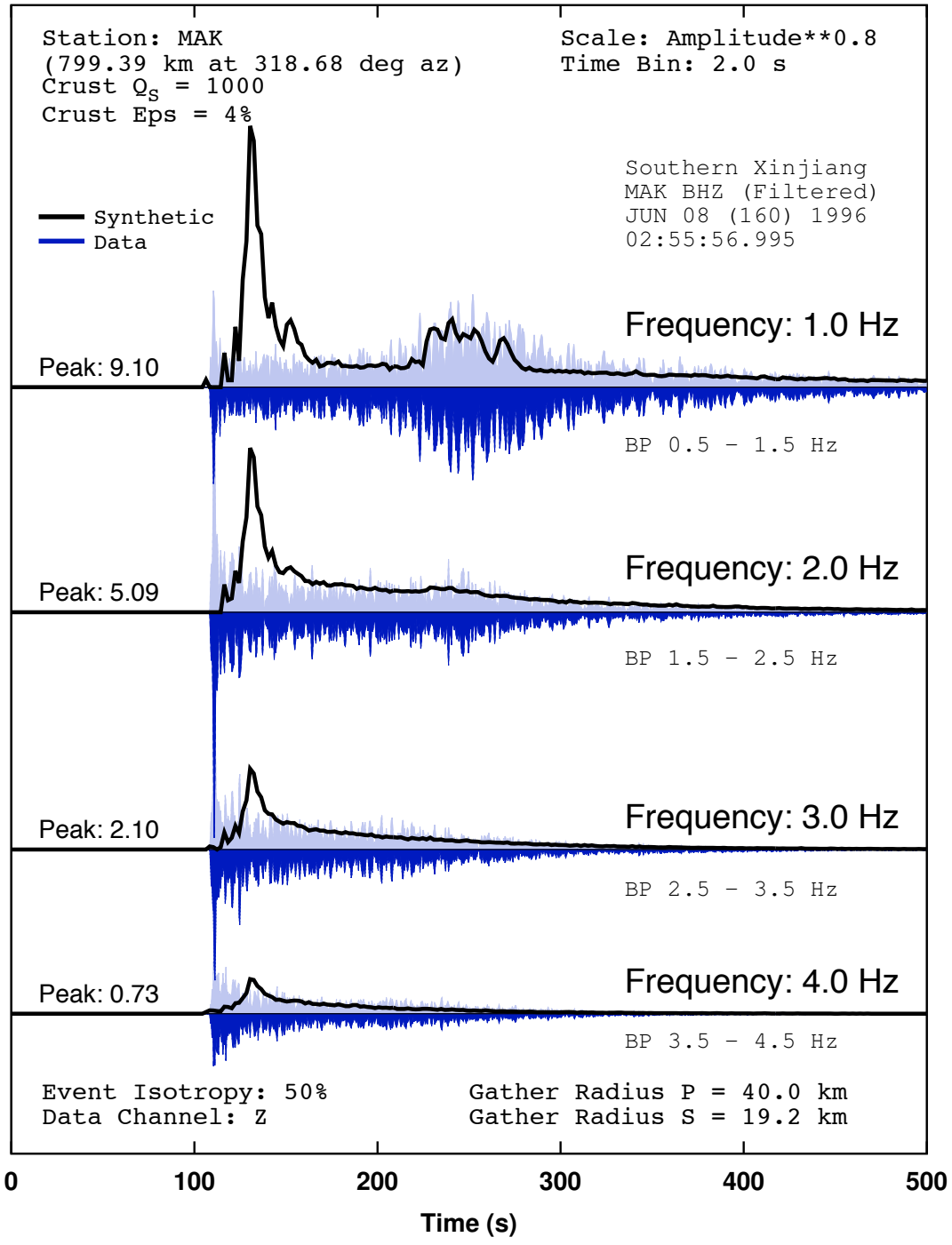

Figure 4.17: Synthetic envelopes for a Lop Nor nuclear test using the source mechanism with tectonic release determined from the surface wave study of Bukchin et al. (2001), compared with observed envelopes for the same test. Plotted amplitude is scaled to the 0.8th power to soften the wide dynamic peak range for graphical presentation.

4.5 Conclusions

We have developed a radiative transport code to shoot body wave rays through general deterministic 3-D structure, including the computation of quantities required to synthesize high frequency body wave coda generated by small-scale, statistically described heterogeneity. Representing the wavefield as a sum of multiply scattered P and S waves in 3-D, it includes reflection/transmission and P-S conversion by interfaces, effects on the amplitude and polarization of scattered re-radiated waves from statistically described small-scale heterogeneity, and intrinsic viscoelastic attenuation. Velocity gradients and earth curvature can be parameterized either by thin layers and an earth-flattening transformation or by specifying velocity models at vertices of space-filling tetrahedra.

Coda envelopes can be plotted in several styles: (1) as a function of time and component of motion at a single station, (2) as a function of distance and time to assist in travel-time picking and travel-time uncertainty estimates, or (3) as snapshots in time as a function of depth and range to understand the evolution of P and S energy and the homogenization of radiation pattern.

Source radiation patterns can be input in the form of generalized moment tensors, which can include tectonic release. The effect of source spectra shape on coda envelopes can be handled by varying the scalar moment for each frequency in simulations for individual narrow band passed simulation.

The availability of both explosion and earthquake waveforms, detailed maps of regional phase efficiency, and the existence of 3-D deterministic structural models derived from global stations and transportable arrays make the Lop Nor region an ideal region to implement our modeling technique. In this region we have completed modeling experiments that have tested the effects on regional coda of parameters specifying the heterogeneity spectrum, the effects of crustal and mantle intrinsic attenuation, the

effects of a thin sediment layer, the nature of the Moho transition, and the effects and detection of explosion triggered tectonic release. Tests varying the parameters specifying small-scale heterogeneity find that the strongest effects on regional codas occur when the scale length specifying the corner of a von Kármán spectrum are close to the dominant wavelength of a narrow band passed simulation. Pn and Sn amplitudes strongly depend on velocity gradients and structural complexity beneath the Moho. In narrow band simulations of coda envelopes, accurate estimates of the intensity of P and S velocity fluctuation, von Kármán scale length, and intrinsic Q in the crust are critical input to the modeling of Lg and the prediction of P/Lg ratios. Tectonic release detected from low frequency, teleseismic, surface waves minimally affects the high frequency (>2 Hz) regional coda in the Lop Nor region. Thus far, the most significant conclusion of all of these tests is that performance of discriminants based on P/Lg amplitude ratios is best at frequencies above 2 Hz from recordings at ranges less than 1000 km.

Chapter 5

Pinch and Bulge Structures

A straightforward structural scenario that can be modeled with the 3-D capabilities of RADIATIVE3D is that of a crust structure with a localized pinch or bulge region, or some other structural or material modification of the crust, at a fixed radius from the event source, such that seismic phases propagating through the crust must cross this region in order to reach receivers on the opposite side. Alternatively, the crust modification might be a region of abnormally high heterogeneity, producing a high scattering region, instead of a pinch or a bulge, or it may be a combination of scattering along with the pinch or bulge. At regional distances, these structures primarily affect the Pg and Lg phases. In this chapter, we study several models in which the seismic phases cross localized regions of crustal variation. The variation regions in this chapter are constructed as elongated bands, extending in an arc of fixed radius from the source, so that the phases must cross perpendicularly to the band. In particular, we look at: two models of a crustal pinch, one model of a bulge, one model of a high scattering region in which the layer thicknesses remain unchanged, and models that combine the effects of pinches or bulges with co-occurring high scattering. These models are compared against a baseline model in which the crust structure is laterally uniform throughout. The models are simple in design and serve to illustrate the broader capabilities of RADIATIVE3D.

5.1 Background

Regions of crustal thinning, e.g. transitions to oceanic crust, have been associated with a phenomenon known in the literature as Lg blockage (Mendi et al., 1997; Zhang and Lay, 1995). This refers to the severe attenuation or elimination of the Lg phase as recorded by receivers opposite the thinning structure from the event epicenter. The mechanism of Lg blockage may involve the geometric aspects of the thinning crust structure (Kennett, 1986), or it may involve scattering from heterogeneity within the pinched region, or both. In some cases, Lg blockage has been observed when propagating along a region of crustal thickening, e.g. the Pyrenees mountains, though this appears to be a much less uniformly observed phenomenon, favoring heterogeneity, rather than large scale geometric structure, as the explanation (Sens-Schönfelder et al., 2009). It is hoped that the studies presented here will shed some light on the phenomenon.

Prior computational studies of Lg blockage in 2-D cross-sectional crustal thinning models include Maupin (1989), Cao and Muirhead (1993), Gregersen and Vaccari (1993), Zhang and Lay (1995), and Mendi et al. (1997). A radiative transport study that examined localized heterogeneity (rather than crustal thinning) as an explanation for Lg blockage can be found in Sens-Schönfelder et al. (2009).

The North Sea Central Graben has been an oft-investigated path for Lg blockage investigation, and in this chapter we develop a model patterned after a path crossing this region and use it to simulate several structural variations.

5.2 Experimental setup: North Sea Crust Pinch Model

5.2.1 General modeling strategy

We constructed a model patterned after the path from Norwich, UK, to station BLS near the Blåsjø reservoir in southern Norway. Norwich, UK, is the approximate location of a magnitude (Mb) 4.8 event that occurred on February 15, 1994, for which data exists from station BLS. The path crosses the North Sea Central Graben, a crustal thinning region approximately midway along the path as it traverses the North Sea. Lg-blockage along this path has been the subject of study of several previous authors.

The prior computational studies referred to here utilized two-dimensional (range and depth) numerical simulations. In order to compare with these prior studies, we have chosen to make our model azimuthally symmetric, with the crust modification region (pinch or bulge) occupying a constant range from the source. This allows us to look at cross-sectional views of our model and results (projecting out azimuth) and to ignore the third dimension. Thus the model simulates normal incidence of the seismic phases as they cross the modification region, in analogy to the previous 2-D studies.

Another advantage of the azimuthally symmetric model design is that, for a hypothesized strike-slip earthquake source, we can capture and isolate particular propagation modes based on the azimuth selected for a linear array of virtual seismometers. This is because, whereas the model is azimuthally symmetric, the source is still three-dimensional, and if we model a strike-slip source mechanism, then the apportionment of radiated energy by polarization mode is a function of azimuth. For example, a seismometer array aligned with either the compressional or tensional principle axes of a strike-slip source will isolate a P-SV system of wave modes, whereas an azimuth intermediate between the compressional and tensional axes will isolate SH polarized waves, as these azimuths coincide with the null-planes for P-wave radiation. Note, however,

that for a strike-slip source, there are no null planes for S-wave radiation, and thus it is impossible to completely isolate P radiation. However, for this purpose we can simulate a pure isotropic explosion source. Thus it is possible to produce simulation results that illustrate the model effects on Pg in isolation from horizontally-polarized Lg, and vice-versa.

The gross structure of our model is fan-shaped, to catch outward-radiating wavefronts within an azimuthal span of 90°. This is wide enough to enclose both an expanding SH wavefront and an expanding P-SV system of wavefronts. The radiance maxima of these two systems have 45° between them, so the 90° angular spread of the model means both azimuths of interest are well within the model bounds. We emplace three linear arrays of virtual seismometers. One array catches SH, one catches P-SV, and a third is intermediate between them and catches a mixture of all modes. The model extends to a range of 1020 km from the source and to a depth of 360 km below the Earth's surface. A range of 1020 km is large enough that the Earth's curvature can affect timing and amplitudes. As such, we include Earth-like curvature in the design of our model. The general modeling strategy is illustrated in Figure 5.1. In all models except the baseline model, the wavefronts must cross a region of crustal variation (RCV), indicated by the brown band in the plan view (Figure 5.1: left), and shown as a pinch region in the side profile view (Figure 5.1: right). We consider RCVs in the form of crustal pinches, bulges, or regions of high scattering due to heterogeneity. The layers of the model follow Earth-like curvature, as can be seen on the side profile.

The event we simulate is alternately an earthquake or an explosion at a depth of 10 km. For the earthquake, we use strike, dip, and rake parameters of 22.5°, 90°, and 0° respectively. This is a strike-slip source oriented so that the compressional and tensional principle axes are parallel to the ground and the null axis is oriented vertically. With these parameters, the compressional principal axis extends outwards at an az-

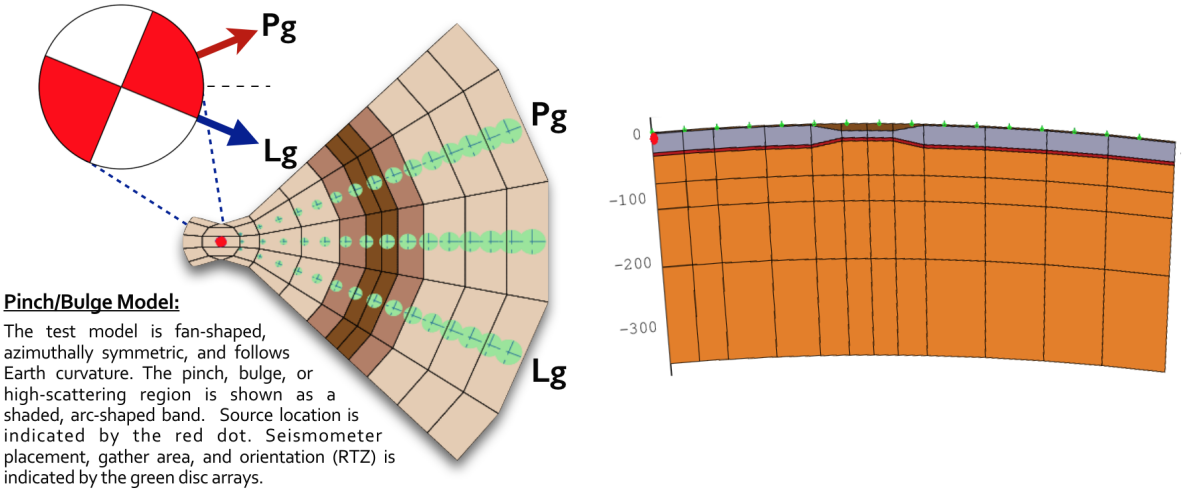

Figure 5.1: Modeling strategy: The models are fan shaped to accommodate expanding wavefronts radiating outward within a 90° azimuthal arc from the source, which is indicated by a red dot in the "handle" of the fan shape. In all models except the baseline model, the wavefronts must cross a region of crustal variation (RCV), indicated by the brown band in the plan view (left), and shown as a pinch region in the side profile view (right). We consider RCVs in the form of crustal pinches, bulges, or regions of high scattering due to heterogeneity. The layers of the model follow Earth-like curvature, as can be seen on the side profile. The model extends to a depth of 360 km and spans a range of 1020 km from the source event location.

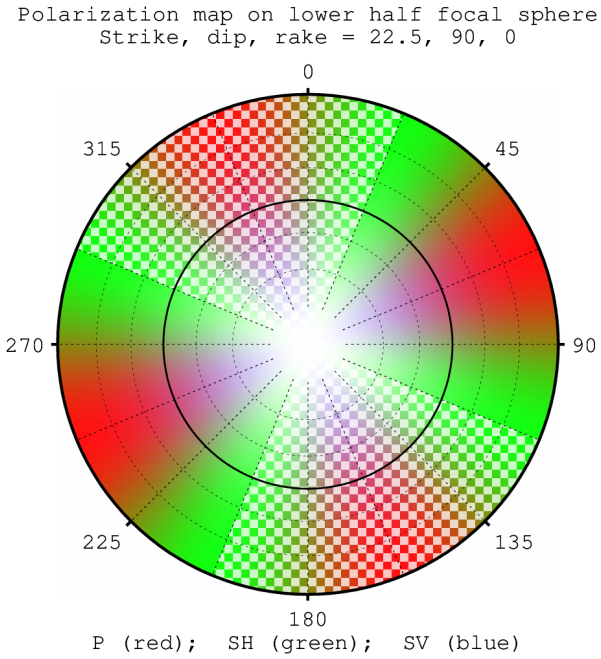

Figure 5.2: Polarization map of earthquake source event. The map shows the directional dependence of the radiated energy by polarization mode. The strike orientation of the event is chosen to align with the virtual seismometer arrays such that one array catches SH polarized energy, which predominantly manifests as the Lg phase, and another array catches P polarized energy along with a small contribution of SV, which predominantly manifests as the Pg phase.

imuth of 67.5° east of north, which becomes a favored direction for sampling the Pg phase. Offset 45° from that, at an azimuth of 112.5° east of north, is a maximum for SH. This becomes a favored direction for sampling Lg. The radiation pattern is illustrated in Figure 5.2. The strike orientation of the event is chosen to align with the virtual seismometer arrays such that one array catches SH polarized energy, which predominantly manifests as the Lg phase, and another array catches P polarized energy along with a small contribution of SV, which predominantly manifests as the Pg phase.

5.2.2 Models enumerated

For the purposes of investigating different crust and bulge structures, we enumerate a set of model identifiers based on the labeling pattern "NSCP*nn*", where *nn* is a numeric code, and the identifier can be read as "North Sea Crust Pinch model, variant *nn*". We may use NSCP00 to refer to an un-pinched, "flat" crustal model, which can serve as a baseline to observe effects of pinches and bulges, which we will label with numeric codes 01 and above.

All model variants consist of seven structural layers. These are: a sediments layer, a basalt layer representing the solid bulk of the crust, a thin Moho transition layer, and four layers spanning the upper mantle down to a depth of 360 km. The four mantle layers follow AK-135 (Kennett et al., 1995), and the three crust layers are loosely patterned after the crustal structure in the North Sea region. Within each layer, a velocity gradient is prescribed, such that velocity increases with depth, starting from some initial value, and ending at a final value, which may or may not be continuous with the next layer. Inter-layer velocity discontinuities are utilized between the sediments and the basalt layer, between the basalt and the Moho transition layer, and a slight discontinuity is prescribed in the mantle at a depth of 80 km, as indicated in AK-135.

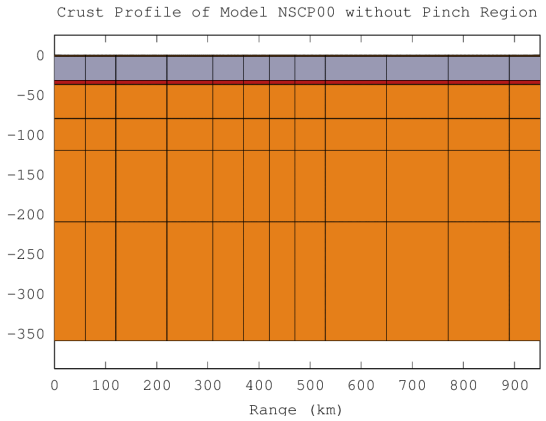

Baseline

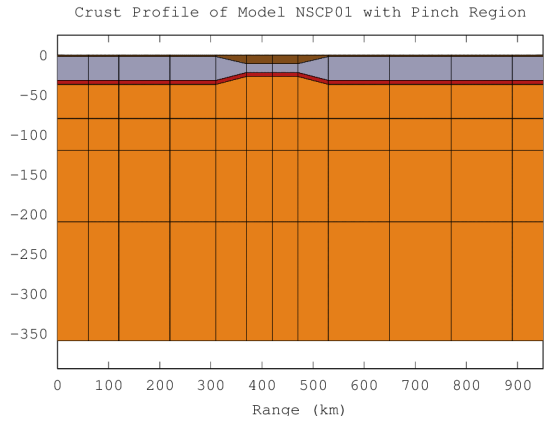

Pinch with overlay

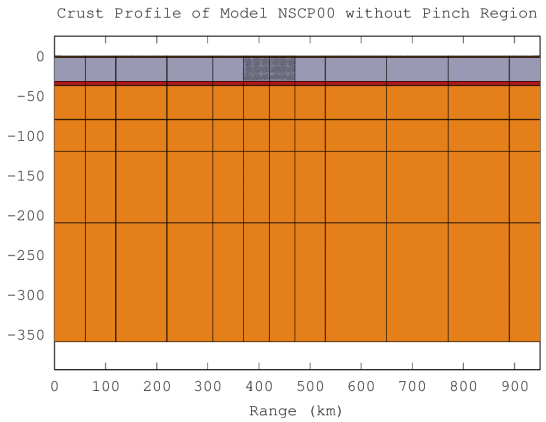

Scattering region

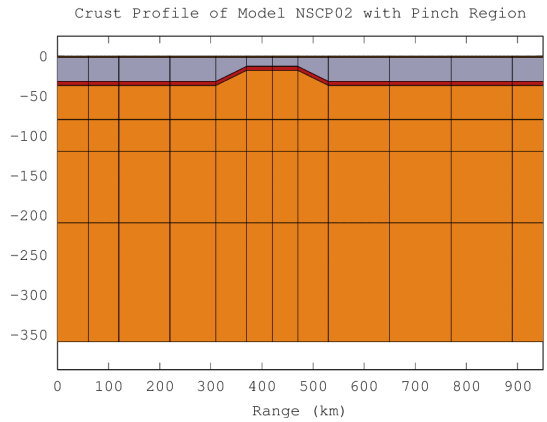

Pinch without overlay

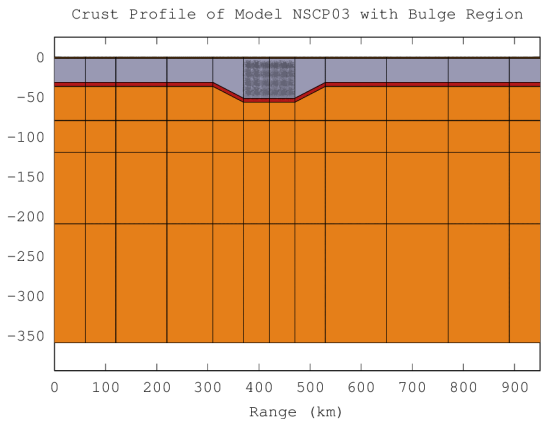

Bulge and scattering region

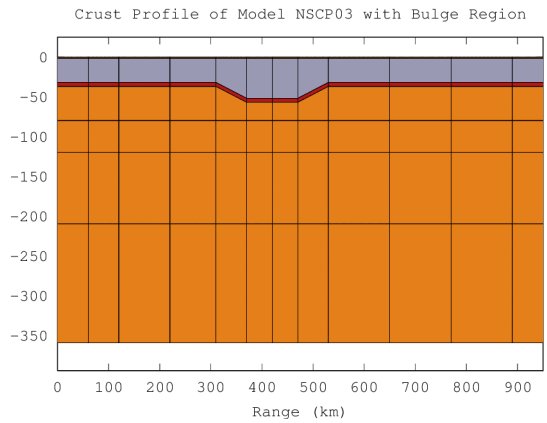

Bulge

Figure 5.3: Model Profiles. Six variations are illustrated here, including the baseline model, four models that perturb the layer structure within a localized region (pinches and bulges), and two that add a localized high-scattering region in the crust layer.

Layer	NSCP00	NSCP01	NSCP02	NSCP03
Sediments	2 km	11 km	2 km	2 km
Crust	30 km	11 km	11 km	50 km
Moho Transition	5 km	5 km	5 km	5 km
Mantle Upwell	0 km	10 km	19 km	-20 km

Table 5.1: Layer thicknesses in pinched/bulged regions of models NSCP00 through NSCP03.

Layer	density	v_{P}	v_{S}	Q_{P}	Q_{S}
Sediments	2.20	4.5 to 4.52	2.60 to 2.61	450	200
Crust	2.80	6.20 to 6.24	3.58 to 3.60	3374	1500
Moho Transition	3.39	7.70 to 8.00	4.44 to 4.46	3384	1500
Mantle Upwell	3.40	8.00 and up	4.46 and up	2172	900

Table 5.2: Deterministic properties by layer in the NSCP models. Densities are in $\mathrm{g/cm^3}$ and velocities are in $\mathrm{km/s}$. Ranges indicate velocity gradient from top to bottom of layer.

Layer	ν	ϵ (base)	ϵ (enhanced)	a	κ
Sediments	0.8	1%	1%	0.2 km	0.2
Crust	0.8	1%	10%	0.2 km	0.3
Moho Transition	0.8	1%	1%	0.2 km	0.4
Mantle Upwell	0.8	1%	1%	0.2 km	0.5

Table 5.3: Heterogeneity parameters by layer in NSCP models. Epsilon values are shown for both the baseline/background values and for the region of enhanced heterogeneity in models that feature an enhanced scattering region.

NSCP01: Graben zone with sedimentary overlay

Model variant NSCP01 includes a pinched region with a sedimentary overlay and a slight mantle upwelling. In the pinch region, the basalt layer tapers from an initial thickness of 30 km down to a final thickness of 11 km. The tapering is coupled with a broadening of the sediments layer from its initial thickness of 2 km to a final thickness of 11 km, creating a sedimentary basin, and an upwelling of the mantle layer of 10 km. (The Moho transition layer thickness is unchanged, however the layer migrates upwards to remain intermediate between the basalt and mantle layers.) In this configuration, the surface elevation remains fixed throughout the pinch region. The width of the fully pinched region is 100 km, and is bracketed on either side by taper regions of 60 km each, such that the complete width of the crust variation region is 220 km. The variation region begins at a range of 310 km from the source and concludes at 530 km. No changes are made to the velocities in variation region, only to the layer thicknesses. (The velocity gradients, however, are enhanced or diminished with the narrowing or broadening of the layers, so as to preserve the velocity values at the layer boundaries.)

NSCP02: Thin crust due to mantle upwelling

Model variant NSCP02 includes a similar pinch structure to NSCP01 (basalt layer tapering from 30 km down to 11 km). However, this model does not include a sedimentary overlay. (The sediments layer remains at a constant thickness of 2 km throughout the model.) Instead, the mantle upwelling is increased to 19 km. As in NSCP01, the surface elevation remains unchanged throughout the variation region.

NSCP03: Crust bulge protruding into mantle

NSCP03 is a crust bulge model. As in NSCP01 and NSCP02, we do not modify the elevation of the model surface, but instead allow the crust to bulge into the mantle.

In the variation region, we thicken the crust from its initial thickness of 30 km to a final thickness of 50 km. Keeping the sediments thickness, Moho transition thickness, and surface elevation unchanged, this translates to a 20 km intrusion into the mantle. As in models NSCP01 and NSCP02, the variation region begins at 310 km and spans 220 km, which includes 100 km fully-bulged span bracketed on either side by 60 km taper regions.

NSCP00+S: Scattering zone in place of pinch or bulge

NSCP00 is the structural baseline model, in which there are no changes in layer thickness in the crust variation region. NSCP00+S refers to the model used to test the effects of a high scattering region in place of a pinch or a bulge. For this model, we maintain the flat layer structure, but prescribe anomalously high heterogeneity in the basalt layer within the 100 km span beginning at a range of 370 km and concluding at a range of 470 km. This coincides with the fully-pinched or fully-bulged regions within models NSCP01 through NSCP03. There is no additional heterogeneity (above the background levels present throughout the model) in the regions correspond to the taper zones of the the pinch/bulge models. We also tested the addition of a high-heterogeneity region in the crust of the bulge model, which we refer to as NSCP03+S.

Profiles of all four models are plotted for comparison in Figure 5.3 and layer thicknesses and material properties are tabulated in Table 5.1 through Table 5.3.

5.3 Results

Simulation output presented here primarily takes the form of travel time curves and energy curves. Both are representations of the signals collected by single-azimuth linear arrays of virtual seismometers, thus giving information about the wavefronts propa-

gating along those azimuths.

The travel time curves are plots of energy amplitude observed at the surface as a function of range and time. Visual inspection of these plots allows easy identification of individual seismic phases and their relative strengths and temporal profiles. More information on the interpretation of these plots can be found in Sections 3.1.3, "Visualizing output" and 3.2, "Interpreting output," of this manuscript.

The energy curves illustrate time-integrated total energy recorded by the receivers as a function of range from the source. In this sense, they correspond to integrating out the time axis on the travel time plots while retaining the range axis. As with the travel time plots, these plots represent signal along a single azimuth as recorded by a single virtual seismometer array. The energy curves are one way to illustrate and quantify the effects of model structure on the outward propagating wavefronts. Towards this end, they are most useful when used with arrays that isolate a single seismic phase, such as Pg or Lg, as it enables us to observe the effects on those phases individually. The effects on individual phases are important to isolate because amplitude ratios such as Pg/Lg are useful for event type discrimination (e.g. earthquake vs. explosion).

5.3.1 Wavefront time series

The time-series plot in Figure 5.4 shows a profile view (range and depth) of phonons propagating through model NSCP01 as a function of time. This gives an indication of the bulk propagation characteristics of the wavefront propagation, and provides some context for interpreting the more quantitative travel time and energy curves. In the figure, blue dots represent S-polarized phonons and red dots represent P-polarized phonons.

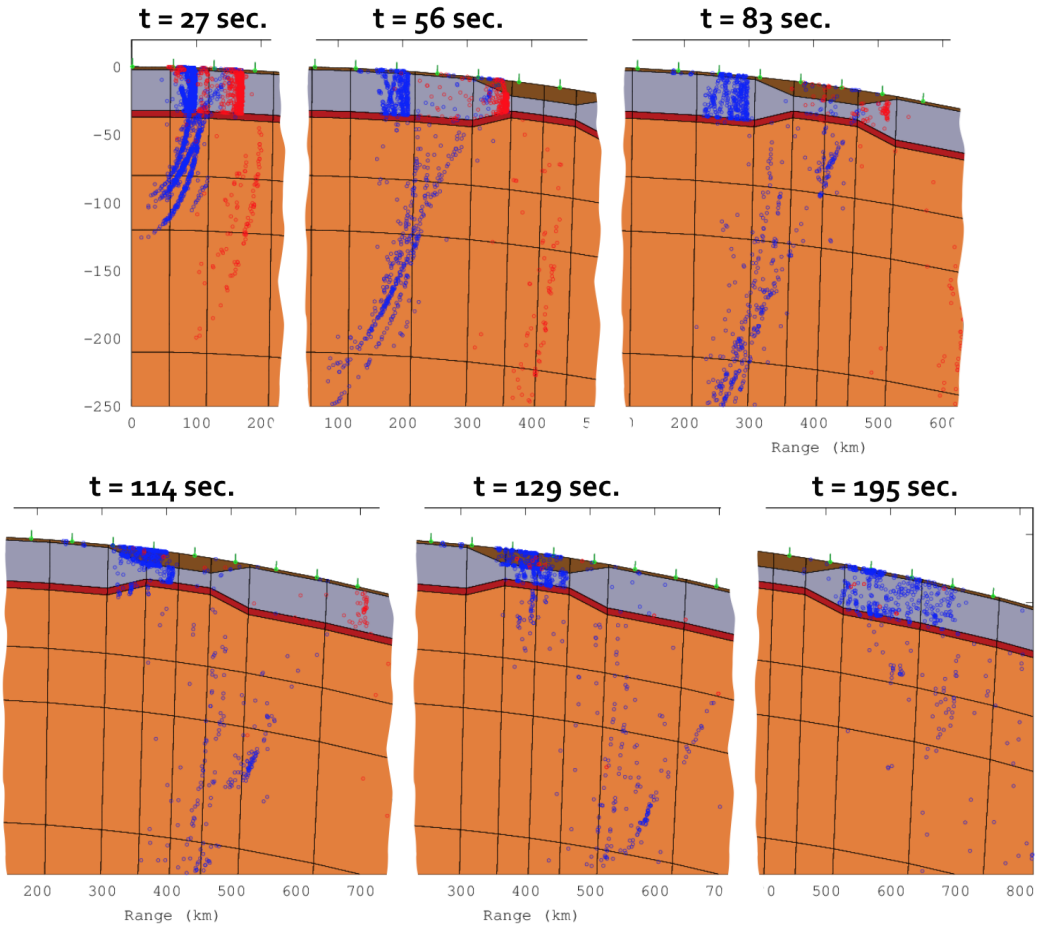

Figure 5.4: Earthquake time-series in model NSCP01. The time series shows phonon propagation through a crust pinch Earth model and illustrates how wave fronts evolve with time. Red markers represent P-phonons and blue markers represent S-phonons.

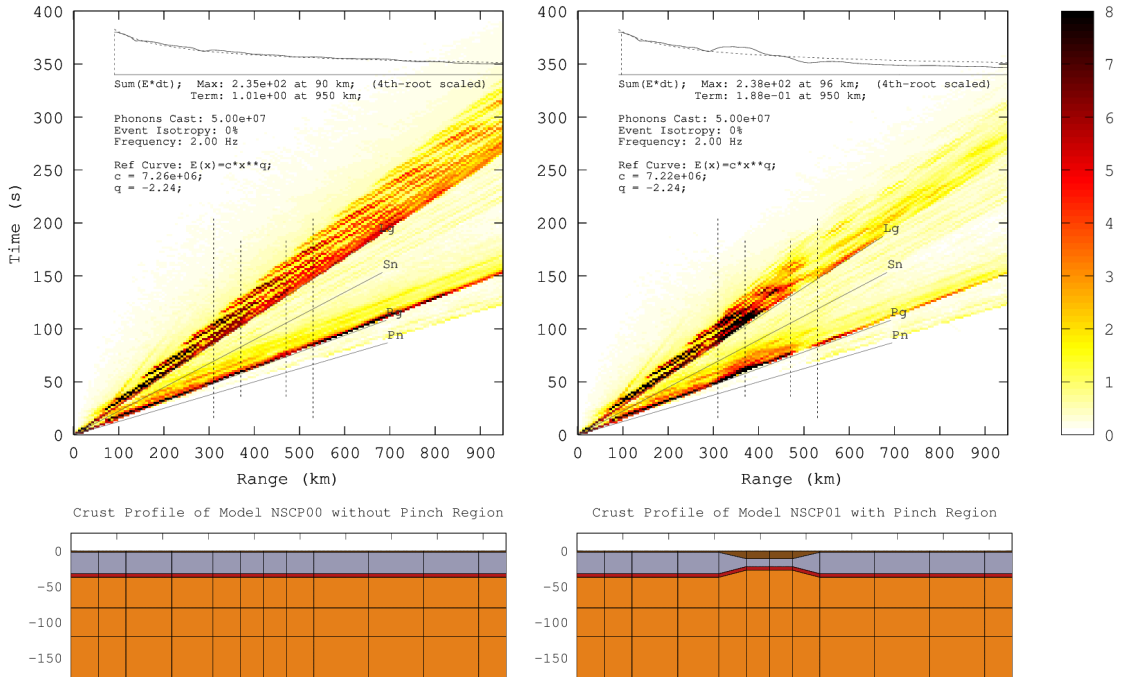

Baseline **Pinch with Overlay**

Figure 5.5: Travel time curves: Color density indicates energy amplitude (square-root of energy flux) as a fraction of a distance-dependent reference curve determined by a power-law fit to the baseline (non-pinched, non-scattering) test case. Reference curve (dashed line) and time-integrated energy (solid line) are shown as overlay plots, along with related statistics, on a 4th-root scale to accommodate compressed vertical space. (Energy curves are shown in greater detail on a logarithmic scale in the Energy Curves in figures 5.8 through 5.9.) Crust variation region is outlined by dashed vertical demarcation lines. Major regional phase velocities are indicated via velocity slope lines. In the example figures shown here, array azimuth is intermediate between the preferred azimuths for SH and P-SV radiation, such that Pg and Lg phases are both well represented in the images. Here we show the baseline case and the pinch with sedimentary overlay case. Subsequent figures show the full set of test cases along azimuths selected to isolate Pg and Lg phases, to facilitate separate analysis of Pg and Lg effects.

Effects on Lg: Pinch, Bulge, and Scattering Models Compared

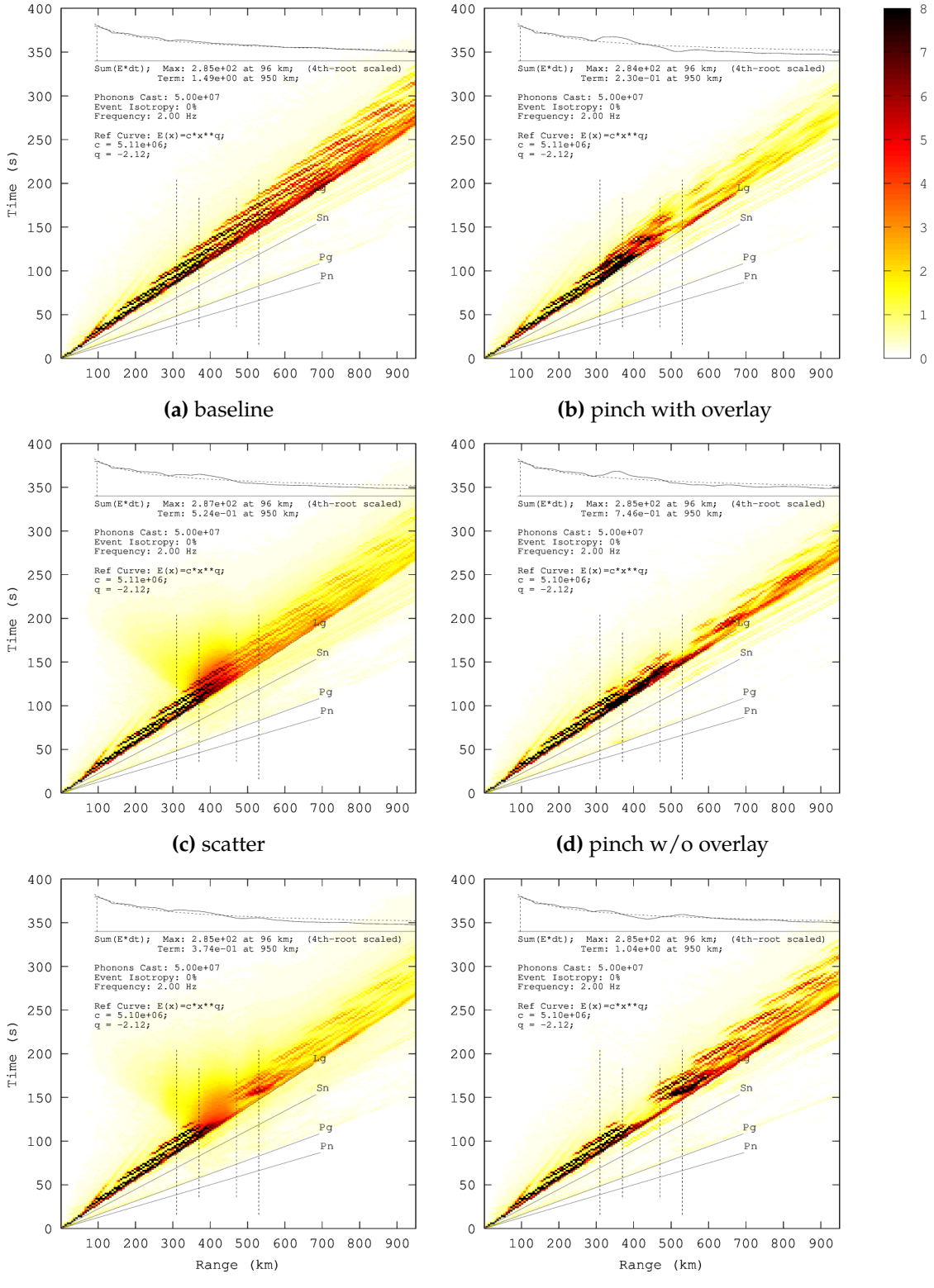

(a) baseline **(b)** pinch with overlay

(c) scatter **(d)** pinch w/o overlay

(e) bulge + scatter **(f)** bulge

Figure 5.6: Travel time curves, Lg effects. Shown here are travel time curves for several different model variants as recorded by an array at an azimuth which selects the SH-polarized Lg phase for our hypothetical strike-slip earthquake source.

Effects on Pg: Pinch, Bulge, and Scattering Models Compared

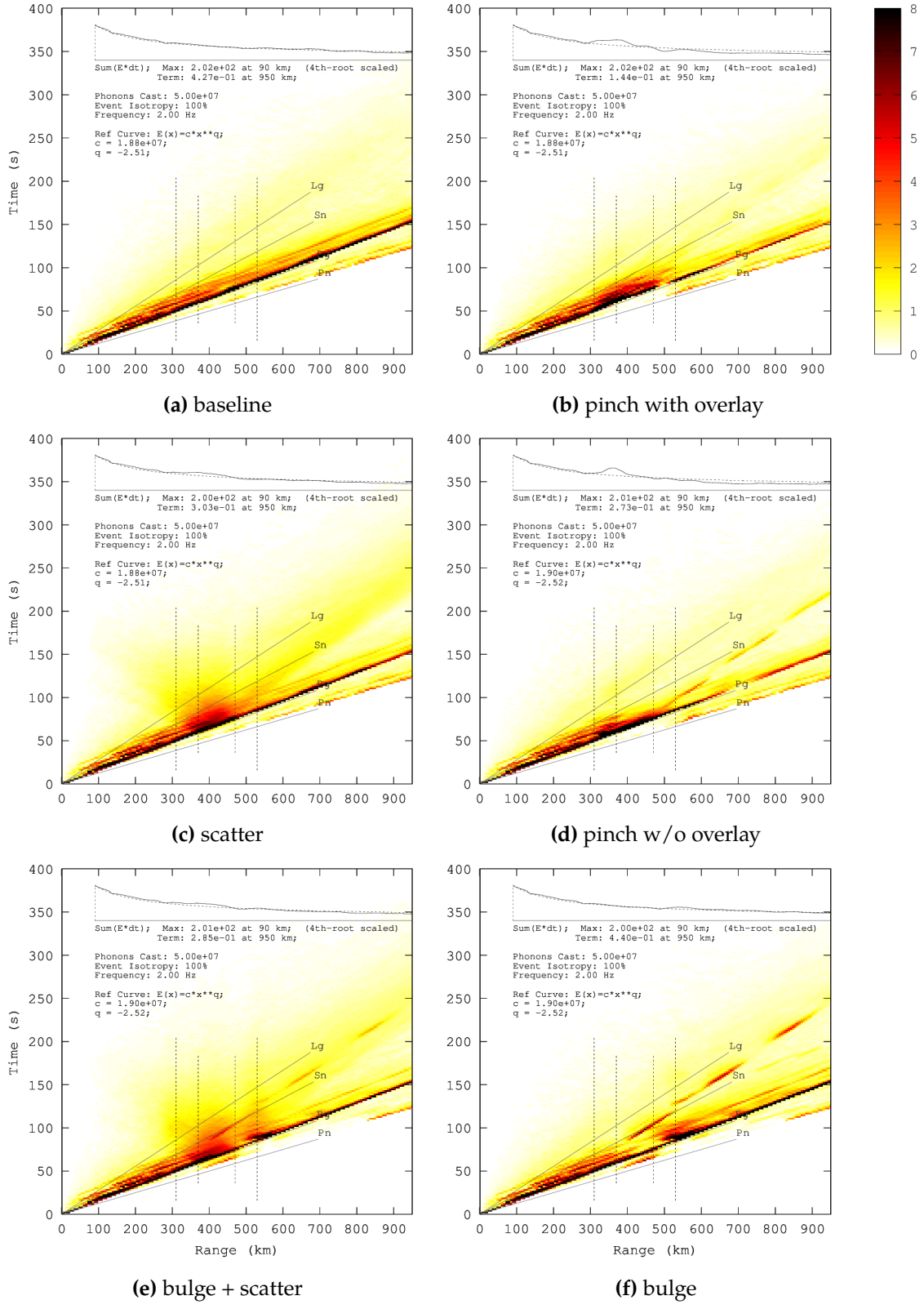

(a) baseline **(b)** pinch with overlay

(c) scatter **(d)** pinch w/o overlay

(e) bulge + scatter **(f)** bulge

Figure 5.7: Travel time curves, Pg effects. Shown here are travel time curves for several different model variants for a hypothetical explosion source, illustrating effects on the Pg phase.

Effects on Lg: Pinch, Bulge, and Scattering Models Compared

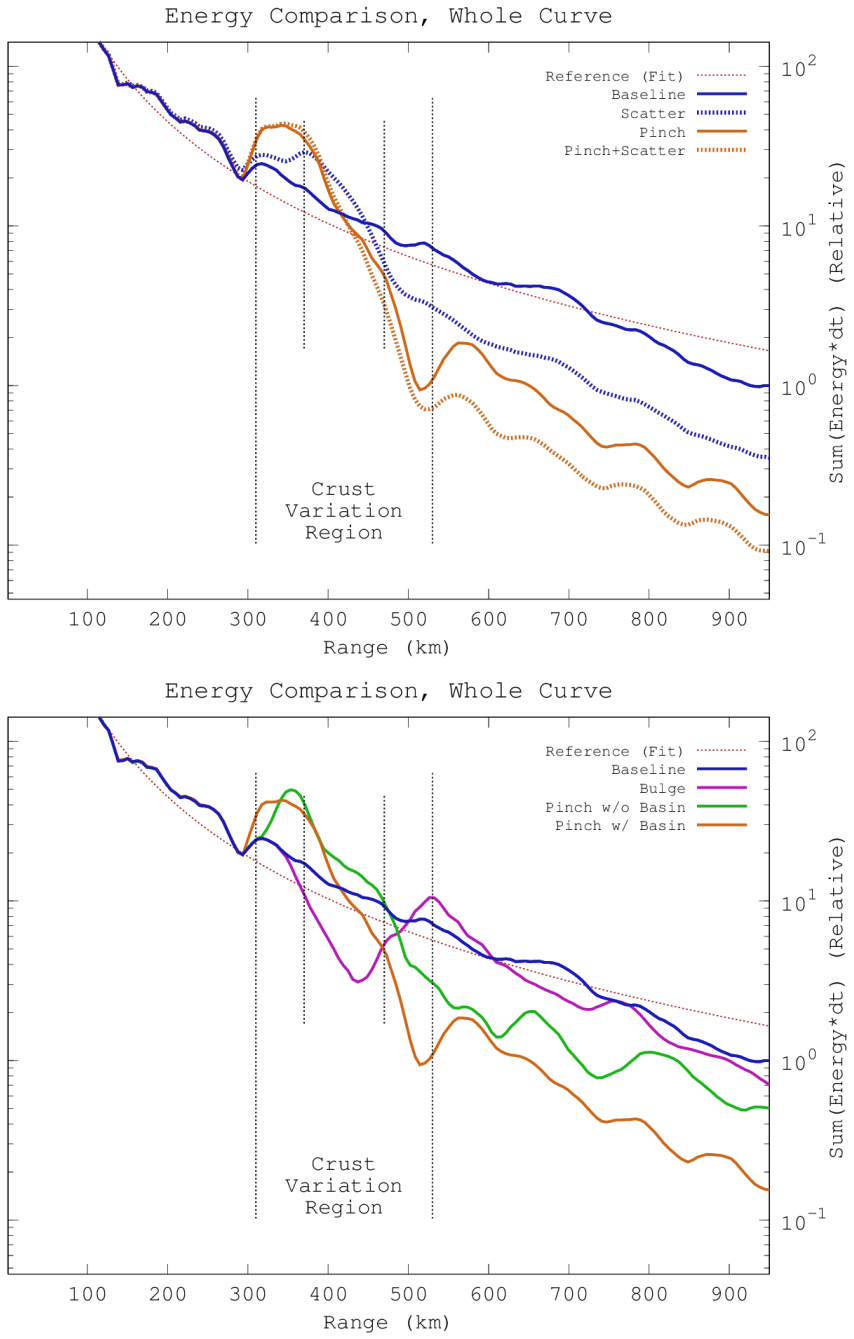

Figure 5.8: Energy curves, Lg effects. Presented here are energy curves showing time-integrated energy arriving at distances up to 950 km for an earthquake source and seismometer array aligned to isolate the SH-polarized Lg phase in various model scenarios including pinch structures, bulge structures, and regions of enhanced scattering.

Effects on Pg: Pinch, Bulge, and Scattering Models Compared

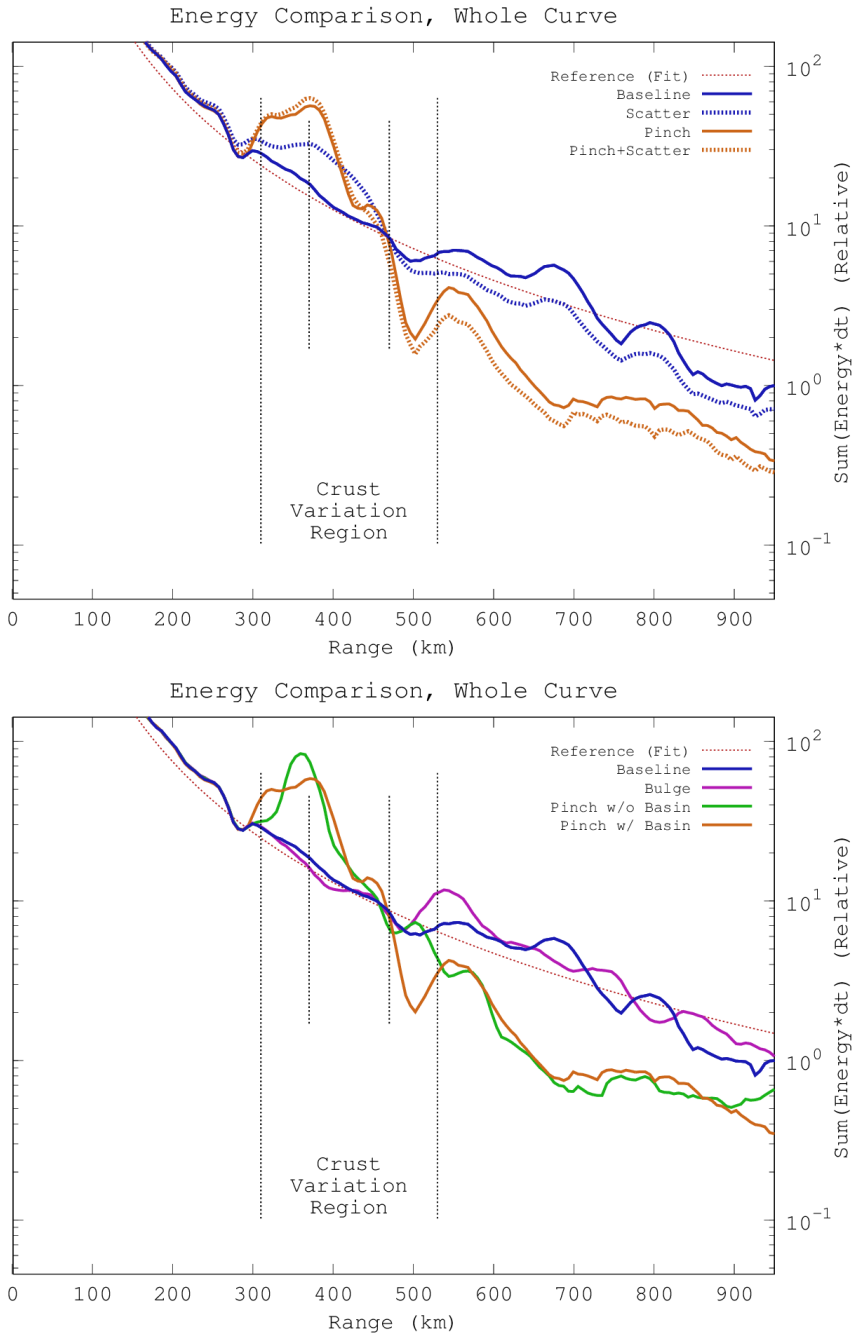

Figure 5.9: Energy curves, Pg effects. Presented here are energy curves showing time-integrated energy arriving at distances up to 950 km for an explosion source isolating the Pg phase in various model scenarios including pinch structures, bulge structures, and regions of enhanced scattering.

5.3.2 Travel time curves

Travel time curves are presented in figures 5.5 through 5.7. Figure 5.5 serves to illustrate the graphical features of the travel time curves and how to interpret them. Figures 5.6 and 5.7 present results for all model scenarios for analysis. The latter are organized into panels, separately showing effects of each model structure on the Pg and Lg phases, respectively. The Pg phase was isolated by simulating an isotropic (explosion) source, and the Lg phase was isolated by recording the azimuth of the double-couple source that maximizes SH polarization, which is a null axis for P polarization.

5.3.3 Energy curves

Energy curves are presented in Figure panel 5.8 for Lg results and Figure panel 5.9 for Pg results. The top subfigure in each panel illustrates scattering effects by comparing the two model scenarios in which we included enhanced scattering regions against the same model structures absent enhanced scattering. The bottom subfigures illustrate structural effects by comparing all four NSCP models against each other in the absence of enhanced scattering.

5.4 Discussion

5.4.1 Pinch vs. scattering effects on Lg

In this subsection we examine the results from models NSCP00 and NSCP01 and compare and contrast the ways in which they differ from the baseline model. The two types of crust variation being considered here are: zone of high scattering (NSCP00+S), and zone of pinched crust with an overlaid sedimentary basin (NSCP01). In the next sub-

section, we compare the the two pinch models (with and without sedimentary overlays) and the bulge model against each other.

First, consider subfigures (a), (b), and (c) of Figure 5.6. These show, respectively, the travel time plots along the azimuth favoring SH-polarized Lg for the baseline model (a), the pinch with sedimentary overlay model (b), and scattering-region model (c). This enables us to investigate the differing ways in which the crust pinch and scattering region disrupt the travel of the Lg phase through the variation region.

Both test cases (b) and (c) are associated with a reduction of energy at long range compared with the baseline case (a). This reduction can be made quantitative by inspecting the energy curve comparison in the top panel of Figure 5.8, which shows the time-integrated energy curves (surface energy flux rate as a function of distance from source event) for each of the three cases (baseline, pinch-with-overlay, scattering region) plus an additional case in which the pinched crust is also a high-scattering region, denoted as Pinch+Scatter in the graph. In that figure, we can see that case (b) (pinch) resulted in an energy reduction of approximately -8 dB at the terminal distance of 950 km. Similarly, case (c) (scattering) was associated with a reduction of approximately -3 dB at the same distance. The greatest attenuation was achieved by the mixed Pinch+Scatter condition, a reduction of approximately -11 dB, showing the more-or-less additive quality of the two attenuation mechanisms.

Although both the scattering region and the pinch-with-overlay test conditions resulted in significant attenuation on the far side of the variation region, there is a difference in the qualitative character of the attenuation, as can be seen again in the travel time plots of Figure 5.6. First, observe that in the baseline condition, the Lg phase is actually a superposition of many sub-phases resulting from multi-pathing as a result of the crust layer acting as an effective waveguide. This manifests in the plot as a striated grouping of many parallel phase curves propagating as a wave train within a broad

velocity window surrounding the nominal Lg phase velocity. The banding structure is very cleanly visible in our simulated baseline travel time plot due to several factors: (1) the relatively low background heterogeneity spectrum of the bulk model, which makes the layers of our model a very clean propagation medium, perhaps in contrast to real Earth structure, (2) the idealizations of the ray-theory method of propagation at the heart of the radiative transport method, which does not simulate diffraction effects that might serve to wash out or blur the banding structure in real Earth propagation, and (3) the precise regularity of the idealized, simplified and uniform layer structure of our model, which preserves the coherence of the many multi-paths due to the lack of fine lateral variations in the thicknesses of the layers or the bulk and shear moduli of the rock media. The result is an artificially clean-looking Lg wave train in the baseline travel time plot. However, this becomes useful in differentiating the disruption mechanisms of pinch vs. scattering variation regions.

In particular, we notice in the scattering case that the energy amplitude is significantly attenuated, but that the multi-path structure of the wave train and the width of the velocity window in which it arrives is largely unaffected. The scattering seems to result merely in a reduction of energy reaching the far side of the variation region, with little change in the character of the arriving signal. The mechanism of action here is almost certainly simple deflection of energy. The travel time plot would seem to indicate a measurable degree of lateral scattering and back-scattering, as indicated by two distinct graphical features, to be described in what follows. Lateral scattering would include a deflection of the propagating phonons either left or right (w.r.t their propagation direction) or up-or-down. As we are probing an SH-polarized Lg phase, we would expect the left-right scattering to dominate, although an up-down fraction would exist to a lesser extent. In either case, both are loss mechanisms. The left-right scattering will divert energy away from the probed azimuth, which repre-

sented one of the four amplitude magnitude directional maxima in the SH radiation pattern, and into the Pg azimuths where SH radiation is at a minimum. Thus more energy should be being scattered away from this azimuth than into this azimuth, and the result will be an overall attenuation. The fraction of phonons that get scattered into up or down directions, on the other hand, will be lost due to other methods. Those trending downwards may make it into the mantle, and thus be lost. Those trending upwards will reflect off the surface, and will then trend downwards. In the latter case, though, they will have interacted with the surface, and this should be visible. And indeed, in the distance range of about 340 km to about 460 km of Figure 5.6(c), the Lg phase manifests a visible halo, appearing as orange in the color scale used in the plot. I believe this may be the result of phonons being scattered into the surface before being reflected downwards and being lost. The second visible feature in the travel time plot is a reflected phase originating at the onset of the scattering region at 370 km, and extending backwards with an Lg-like retrograde velocity in the time window between 120 seconds and 200 seconds. The feature appears yellow on the plot and is faint, but visible. I believe that this represents back scattering.

The mechanisms are different for condition (b) (pinch-with-overlay), however. In this condition, no abnormally high scattering is occurring in the crust variation region. In contrast to condition (a), wherein the phase structure is attenuated but not significantly disrupted, in condition (b) the banded multi-path structure of the signal is severely disrupted in the variation region, and does not survive as a clear multi-path signal on the far side of the region. There is still a clear Lg phase, and the timing of the phase is similar (the energy still falls within a very similar velocity window), but the signal has become amorphous in character. This must be a result of a perturbation of the waveguide character of the crust layer in the crust variation region.

We can get some clue as to what is happening by again looking at the energy curves

in subfigure (a) (top panel) of Figure 5.8. The pinch-with-overlay condition is represented by the solid orange line, and the baseline condition by the solid blue line. The blue line follows a more-or-less uniform trend of decaying energy with increasing distance, as would be expected. The pinch line, however, experiences a major downward shift within the variation region, and resumes a more gradual decaying trend after the region. An interesting aspect of the trend inside the variation region is that it begins with an initial increase in the energy interacting with the surface that starts slightly anterior to the onset of tapering leading to the pinch region, reaches a maximum as the tapering approaches the fully pinched region, then trends sharply downwards throughout the pinched region, and finally recovers some energy in a narrow region near the conclusion of crustal re-broadening and the region immediately posterior to the variation region. These three phenomena: the sharp decline of energy within the variation region, the initial amplification of energy, and the final amplification (recovery) of energy, all need explaining. I will propose some possible explanations here, and in the next subsection will attempt to corroborate them by investigating different pinch and bulge structures.

The sharp decline of energy in the pinch region is most likely the result of phonon ray paths that transmit into the 11 km-thick sedimentary basin overlaying the pinch region, wherein they become trapped until they exit back into the crust on the posterior side of the variation region. The sediments layer is a low-velocity, high-attenuation (Q^{-1}) zone, with elevated scattering-inducing heterogeneity (even in the non-scattering-region models). As such, the energy content of each phonon will decay much more rapidly in the sediments layer than in the rest of the model. Because of the sharp velocity discontinuity between the sediments layer and the crust layer, down-trending phonons are very likely to reflect upwards, and multiple reflections between the surface and sediment-crust boundary mean that the sedimentary basin will be a

waveguide for a slowly-moving, multiply-reflected, highly-attenuating, Lg-like phase that will separate from the faster moving Lg phase still propagating through the narrowed crust.

Another loss mechanism would be phonons that transmit from the crust layer into the mantle as a result of the reduced angle-of-incidence (which would tend to increase the transmission coefficient) that would occur where the crust floor angles upwards to produce the tapering region.

The initial upswing in energy in the anterior tapering region is harder to explain, though two possible mechanisms may play a role. One is that the upward grading of the crust floor in the anterior tapering zone would bend rays reflecting off of it from a more glancing to a more directly upward trajectory towards the surface. Furthermore, as the ray transmits from the crust to the sediments layer, there is a decrease in velocity that would bend the ray towards the interface normal, which would be an additional adjustment towards upwards vertical propagation. These two bending events would have the effect of focusing the energy towards the surface, and might be enough to substantially increase the energy flux rate at the surface in that narrow region, before the attenuating effects of the sedimentary layer begin to dominate. The fact that the increase begins about 10 km *prior* to the onset of the tapering zone is puzzling, but may actually be a measurement artifact rather than a physical affect, as the virtual seismometers at 300 km range have a gather radius of 14 km, and thus are, in fact, sensitive to the leading edge of the crust variation region. Another mechanism that may explain the initial energy upswing is the possibility of rapid multiple-reflections between the surface and sharp velocity discontinuity between the sediments layer and the crust layer, in the tapering zone where the sediments layer is still thin enough that the attenuation affect has not yet taken over. In essence, the energy might be "rattling around" in the sedimentary basin layer, serving to amplify the surface signal in the

anterior regions, but ultimately succumbing to intrinsic attenuation as the sedimentary Lg fraction propagates towards the posterior region of the basin.

The energy recovery that happens at the very end of the crust variation region (upswing in the pinch series centered at about 540 km in Figure 5.8, top panel) is perhaps the hardest to explain, and what is offered here is very conjectural. Again, two specific mechanisms are proposed. Firstly, the rate of multiple-reflections, or "rattling," that occurs in the basin-shaped sedimentary layer, would increase as the sedimentary Lg fraction reached the tail end of the basin, due to the thinning of the layer back to its nominal thickness. This would increase the interaction of the phase with the surface, and is essentially the same mechanism as is proposed as a partial explanation of the upswing at the beginning of the basin. This effect would be expected to be observed in the region slightly before the conclusion of the crust variation region. However, it shouldn't contribute significantly beyond the conclusion of the region (at 530 km). The second mechanism may explain the remainder of the upswing, which occurs mostly beyond the conclusion of the variation region. Within the pinched-crust region, the Lg phase has separated into a slower-moving sedimentary Lg phase, trapped in the basin, and the faster moving crustal Lg, where the thinned crust is still acting like a waveguide at depth. The energy trapped in this waveguide is not interacting with the surface. However, when the crust re-broadens, the energy expands back into the full-width crust and regains the ability to interact with the surface in the same way as it did prior to the crust variation region. So in this sense, it may be that the at-depth crustal Lg, which is shielded from the surface while trapped in the pinch, is returned to the surface after the pinch, and this could be recorded as an increase in surface energy flux in the region posterior to the crust variation region. In fact, a possible visible indicator of this can be seen in the travel time plot (subfigure (b) of Figure 5.6) as an energy-dense temporally sharp phaselet almost exactly aligned with the Lg velocity line that

is present between 530 km and 680 km.

5.4.2 Pinch models compared

To go further with our attempts to explain the phenomenology of the pinch-with-overlay model, it is helpful to compare against other models of crustal thickness variation which differ structurally from the pinch-with-overlay model. To that end, we here compare models NSCP01, NSCP02, and NSCP03, which are, respectively, (1) the pinch-with-overlay model, (2) a pinch model with the same degree of crustal narrowing, but without the sedimentary overlay (the mantle upwelling is exaggerated to compensate), and (3) a crust bulge model, in which crustal thickness increases and protrudes into the mantle, in a manner similar to a mountain root. Still keeping our focus on Lg phenomenology, the results we will be looking at here appear in Figure 5.6, subfigures (b), (d), and (f), and in the bottom panel of Figure 5.8.

First, we will compare pinch results with and without sedimentary overlay. The qualitative differences in phase structure observed between subfigures (b) and (d) of Figure 5.6 are difficult to characterize, though they are visually distinct. It is easier to draw conclusions from the energy curves in Figure 5.8, bottom panel. In this figure, the pinch-with-overlay results are represented by the orange line, and the pinch-without-overlay results are represented by the green line. The first thing to notice is that the overall attenuation at the distal end of the model (950 km range) is less severe for the pinch-without-overlay model than for the pinch-with-overlay. In particular, we see that the pinch-without-overlay model experiences an energy reduction of approximately -3 dB with respect to the baseline model, compared with approx. -8 dB for the overlay model. This supports the notion that the sedimentary basin in NSCP01 is a major component of the loss mechanism in that model, accounting, perhaps, for as much as 5 dB of attenuation. The remainder of the attenuation must be explainable by other

mechanisms.

The second thing to notice in comparing the pinch models is that both pinch models show an initial upswing in surface energy flux in the anterior tapering wing of the crust variation region, and that both pinch models show a trend of decreasing energy throughout the remainder of the variation region, with the overlay model exhibiting the sharper downtrend, and the non-overlay model exhibiting a more gradual decrease in this region. Most interesting, though, is that whereas the overlay model exhibits a final upswing or recovery of energy at the completion of the crust variation region, the non-overlay model exhibits no such recovery, manifesting a smooth continuation from the posterior tapering wing of the variation region into the region beyond the crustal variation. In the preceding subsection, we proposed that "rattling" (rapid reverberation) in the very beginning and the tail end zone of the sedimentary basin played a role in the initial and final energy upswings. The absence of this reverberation in the model without the sedimentary overlay, and corresponding lack of final upswing in the energy curve, could be seen as support for the hypothesis that this plays a role in producing the upswing in the overlay model. However, a second mechanism to explain the final upswing in the overlay model was also proposed. This second mechanism was the division of the Lg phase into two sub-phases each following a different propagation modality: a sedimentary Lg propagating slowly through the sediment basin (while rapidly attenuating), and the deeper crust Lg propagating with normal velocity, but isolated from interaction with the surface, until reaching the end of the basin where it could again interact with the surface, explaining the final upswing. This mechanism would *also* be absent from the non-overlay model, since the thinned crust in that model is positioned at the top of the model, rather than being pushed down to deeper depths by the presence of the sedimentary basin. Thus there would be no sudden energy return event at the conclusion of the crust variation region to produce an

upswing of energy. Thus between both proposed mechanisms, we can say that both are likely contributing, though it is not clear without further investigation whether one mechanism is dominant, or whether both contribute significantly to the observed outcomes.

The upswing is present in both models at the beginning of the variation region, however. Here again, two mechanisms were proposed. The first was basin rattling, and the second was a focusing effect from the upward inclination of the crust floor, which would bend rays reflecting off of the floor from a more horizontal orientation to a more vertical orientation, intensifying their interaction with the surface in that region. Basin-rattling is not an option in the non-overlay model. (Although a similar increase in multiple reflections is likely in play. This will be discussed below.) This leaves the change in incidence angle as the most viable explanation. Note that because the incline of the crust floor in the taper zone is more extreme in the non-overlay model, the intensifying effect could be more extreme. Indeed, the peak (at approx. 350 km) of the non-overlay energy curve is slightly higher than that of the overlay energy curve. It also occurs at a slightly more distant range than in the overlay curve. This could be because both mechanisms (rattling and focusing) are occurring in the overlay model, but only focusing is occurring in the non-overlay model, and the basin-rattling mechanism might be more efficacious in the nearer range window.

The next thing to examine is what happens to the non-overlay energy curve within the fully-pinched central region of the crust variation region. As is the case with the overlay model, here we see a generally downwards trend. However, unlike the overlay model, the downward trend is both (1) not as steep as the overlay model and (2) the energy remains above the baseline curve until the very end of the fully pinched zone (the beginning of the posterior tapering wing). In fact, except for edge effects, the downward trend seems to parallel the baseline within the pinched zone. This may indicate

that no additional attenuation mechanism are in play beyond those also present in the baseline: namely geometric spreading and a certain amount of continual leakage into the mantle. The fact that the energy level rides above the baseline in this zone may be due to an increase in the rate of surface reflections on account of the shallower crust floor. This is similar to the rattling mechanism of the basin, only it is in basaltic rock media, not lossy sedimentary media. At the conclusion of the pinched region, as the crust begins to broaden back to baseline thickness, the energy level drops again.

Posterior to the crust variation region, the non-overlay energy curve remains below the baseline curve, but above the pinch-with-overlay curve. This indicates that while the pinch-without-overlay had an overall attenuating affect on the Lg phase, it was not nearly as efficient at blocking the Lg as the model with the sedimentary overlay was. This makes sense, since a significant amount of the Lg-blockage mechanism of the overlay model was attributed to the intrinsic attenuation acting on the fraction of the Lg wave that propagated through the sedimentary basin. The remainder of the attenuation was attributed to mantle leakage as the phase was incident on the anterior tapering wing of the crust modification region, and that mechanism is probably the dominant loss mechanism in the non-overlay model.

5.4.3 The bulge model

Lastly we turn our attention to the bulge model (NSCP03). The most striking thing to notice is that this is the least disruptive of all the crust variation models. The bulge model travel time results for Lg propagation appear in subfigure (f) of Figure 5.6. At long range, the phase timing, structure, and intensity are nearly identical to the baseline, except for a few small pockets of anomalous quiescence. The most striking difference occurs in the middle zone of the crust modification region, (the zone where the crust has expanded to its maximal thickness between the two tapering wings). Here,

there is a very sizable quiescence with almost a complete vanishing of energy interacting with the surface.

In the energy curve in Figure 5.8, the bulge result is represented by the plum-colored line in the bottom panel. This figure shows that in the regions beyond the variation region, the bulge result parallels the baseline very closely, and manifests only a very minimal attenuation of approximately -1 dB at the terminus of the plot. This tells us that the bulge structure was a very inefficient mechanism for Lg blockage. The majority of the energy propagates through the bulge, and retains the majority of its structural and timing characteristics as well.

Within the variation region, a very sharp dip, or notch, is seen in the energy curve. This corresponds with the quiescence zone in the travel time plot. The mechanism for this is not hard to understand. Since the Lg phase is composed of a wave train of several multiply-reflected wave fronts channeled between the surface and the crust floor, there is a substantial amount of interaction with the surface in the region anterior to the variation region. When the Lg phase enters the variation region and the crust thickness expands, the individual wavefronts, after reflecting off the surface, must bottom at a deeper depth before they can return to the surface. The extra time needed to bottom at the deeper depth creates a time window in which the energy is unavailable to interact with the surface. The length of the bulge region is such that when the energy returns to the surface, it has traversed the variation region and continues its original propagation modality.

This would seem to implicate the length of the bulge region as an important parameter in controlling the signal in the bulge region, and perhaps beyond. For example, if the bulge region were sufficiently lengthened, it would be possible for the Lg phase to bottom twice before traversing the region. This should then produce two quiescent zones in the bulge region on the travel time plot, with an active zone in between, and

correspondingly two notches in the energy curve.

It is interesting that the bulge model produced very little terminal-range attenuation, in contrast to the pinch models, especially since mantle leakage as the Lg phase was incident on the inclined crust floor was proposed as a significant attenuation mechanism. An inclined crust floor is not absent from the bulge model, but rather occurs at the end of the variation region rather than the beginning. The results in our model would seem to indicate that the Lg phase never substantially interacts with this incline. But if the bulge region were lengthened, but not so much as to allow for a double-bottoming, then a substantial interaction with this inclined floor might be possible, and corresponding attenuation of the post-variation region might be observed. Thus we hypothesize that the attenuation measured at the terminus of the model might be controllable and be a cyclical function of the length of the bulge region. This of course could be tested quite easily (but has not as yet been tested).

5.4.4 Effects on Pg compared to Lg

The effects on Pg (Figures 5.7 and 5.9) are for the most part pretty similar to the Lg results (Figures 5.6 and 5.8). In the baseline travel time curves, three general differences are noticeable, and are obviously unrelated to the pinch, bulge, or scattering-region structures. One is that the Pn phase is noticeably excited in the Pg case, whereas the Sn is all but absent in the Lg case. This could indicate that the Moho transition is more transmissive to Pg at near-critical incidence angles, allowing a greater fraction of energy to leak into the transition region and upper mantle(Shaw and Orcutt, 1984), where the energy can propagate at the faster Pn velocity. The second difference to notice is that the series of path multiples making up the Pg wave train seems truncated at a small number beyond approximately 400 km range, in contrast to the much longer wave train that develops in the Lg phase. This may be related to the aforementioned

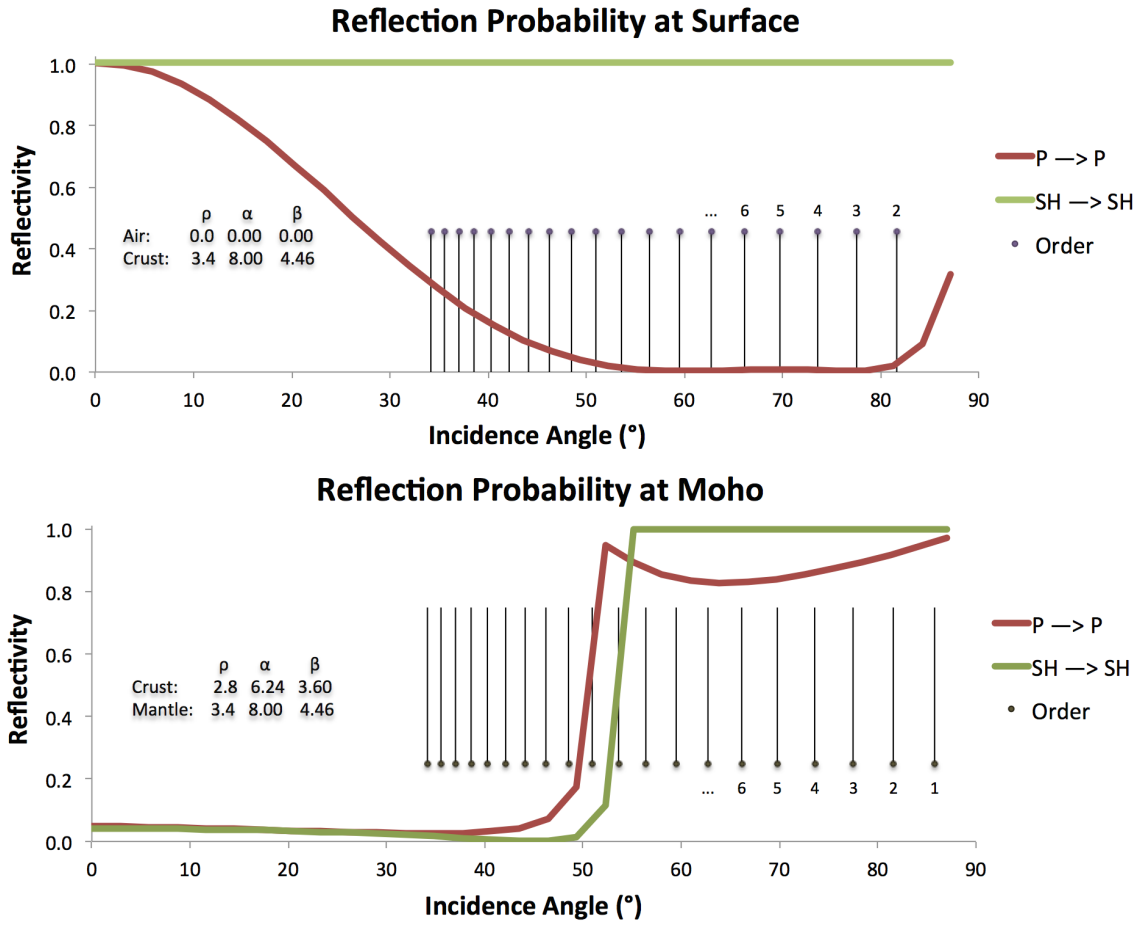

Figure 5.10: Reflectivity at surface and Moho: Figures show the probability of a given ray mode reflecting off the surface or Moho without either changing polarization mode or transmitting into the Mantle as a function of incidence angle to the interface, for a simplified Earth model in which the free surface and Moho are sharp discontinuities. The probabilities are derived from the reflection/transmission coefficients for the selected interfaces, and can be used to predict the waveguide efficiency of the direct arrivals and higher-order path multiples of the Pg and Lg phases at a distant receiver location. Vertical grid lines demarcate the incidence angles by order number for a source-to-receiver distance of 950 km and Moho depth of 35 km. The order number indicates the number of Moho reflections that a ray will experience between source and receiver for a given multi-path. The number of surface reflections will necessarily be one less than the number of Moho reflections. We see here that the SH→SH reflection probability is unity over a wide range of incidence angles, and that for SH-polarized Lg the first nine multi-paths should arrive with high efficiency at 950 km. For Pg, however, the Moho reflection probability is near unity only for the first-order arrival, and the surface reflection probability strongly favors P→SV conversion, thus predicting that the Pg phase will be truncated at first order and will not develop a multi-path wave train like the Lg phase does.

increased transmissivity into the Moho transition region, which may prevent the Pg phase from supporting the higher-order path multiples. Thirdly is that the Pg phase develops a low energy, long-tailed coda region that expands into a much wider velocity window than what is seen in the Lg case. This is a result of scattering. Every model we simulated, even if absent any regions of high-scattering, does have a very small amount of background heterogeneity specified throughout the model. The effect of that is seen in the mild, but long, coda in the Pg results. In general, scattering has a greater effect on P-polarized wavefronts than S-polarized wavefronts, which explains the greater background scattering activity of the Pg results, and furthermore the P→S scattering conversion channel is generally much stronger than the S→P conversion channel, which explains how the Pg coda extends even into the Lg velocity window (Sato et al., 2012).

Despite these overall differences in phase presentation, very little differs qualitatively or quantitatively between the Pg and Lg pinch, bulge, and scatter results. There is, for the most part, a one-to-one correspondence of graphical features between the travel time plot and energy curve results from both sets, except for two notable distinctions, to be discussed below. The similarity between Pg and Lg results is perhaps seen most clearly in the energy curve results (Figure 5.8 for Lg and Figure 5.9 for Pg). Here, the energy trends for each model case can be seen to be quite similar between Pg and Lg in most respects.

Perhaps the most distinct difference between Pg and Lg visible in the energy curve results is in the overall attenuation at the terminal range of the model (950 km). The attenuation of the Pg phase was less than the attenuation of the Lg phase in each model case. For example, in the pinch-with-overlay model, the Lg phase was attenuated by about -8 dB at 950 km, whereas the Pg phase in the same model experienced an energy attenuation of only about -4 dB. Similar reductions are seen in all other model cases

as well. (Indeed, in the bulge model, the Pg phase actually experiences a very slight *amplification* at 950 km, compared to an approximately -2 dB attenuation for Lg.) A simple conclusion to be drawn from this is that the model structures studied here are significantly more efficient Lg-blockers than they are Pg blockers.

The second distinct difference to note, and this is visible in the travel time plots, is that in the Pg results we see a phenomena that is absent in the Lg results, and that is phase conversions. Particularly, we see very clear Pg to Lg conversions in the pinch-without-overlay, bulge, and bulge-with-scattering-region results (Figures 5.7d through 5.7f), beginning around 400 to 500 seconds. This may be because the reflection coefficients for P waves favor P to SV conversions at the surface for a wide interval of incidence angles (see Figure 5.10). Path multiples that include at least one en-route bounce off the surface could experience this conversion channel. The effect is absent, however, from the baseline case (5.7a), which suggests that the pinch or bulge structure must be a contributing factor. A P to SV reflection off the surface will steepen the incidence angle as the reflected SV propagates towards the crust floor. Thus, in the baseline case, the SV-reflected wave from the surface would likely transmit into the mantle and be lost, due to the steep incidence angle. However, in the pinch and bulge structures, the downtrending SV wave can reflect at a more glancing, post-critical angle off the descending segment of the Moho interface in the tapering wings of the crust variation region. This explanation is corroborated by the fact that the Pg-to-Lg phase occurs earlier in the bulge model, where the descending interface occurs on the leading edge of the variation region, than in the pinch model, where the descending interface is on the trailing edge of the region.

5.5 Conclusion

Previous numerical and observational studies of high frequency regional seismic propagation have found that phase attenuation and blockage can be due to a combination of factors, e.g., Kennett (1986), Maupin (1989) and Sens-Schönfelder et al. (2009). These factors include intrinsic attenuation, scattering attenuation, crustal thickness variations, source depth and source mechanism. In this chapter we have described the application of a fast, efficient, radiative transport algorithm to the modeling of Lg propagation that allows all of these factors to be included and tested against observations. Some general effects of crustal thickness variations have been demonstrated for several source depths and mechanisms. For earthquakes and explosions at shallow depths in the crustal waveguide having propagation paths crossing crustal thinning regions, Lg is amplified at receivers within the thinned region but strongly disrupted and attenuated at receivers beyond the thinned region. For the same source depths and mechanisms having propagation paths crossing regions of crustal thickening, Lg amplitude is attenuated at receivers within the thickened region, but experiences little or no reduction in amplitude at receivers beyond the thickened region. Localized regions of intense scattering within laterally homogeneous models of the crust increase Lg attenuation but do not disrupt its coda shape. The effects of crustal thickness variations on Pg correlate with those on Lg, but are much stronger on Lg. In future work, we plan on systematically testing the effects of a broad spectrum of Earth model and source parameters for regional phase paths crossing at least one specific region each of crustal thinning and thickening. These can regions may include regions that have studied by other investigators, including the North Sea, Barents Sea, Sea of Japan, Tibet Plateau, and the Pyrenees.

Chapter 6

Radiative3D Development Roadmap

This chapter describes some of the work still to be done to maximize the utility of RADIATIVE3D. The development of RADIATIVE3D is an ongoing project, which aims to be of use to the scientific community at large. To best serve that community, RADIATIVE3D is offered as free and open-source software.

6.1 Features in development

6.1.1 Anisotropy of heterogeneity scale lengths

Anisotropy of heterogeneity scale lengths that scatter high frequency seismic waves can affect coda shapes (Hong and Wu, 2005) and spatial coherence of amplitudes (Tkalčić et al., 2010) depending on the angle their wavefronts make with the axes of vertically or horizontally stretched heterogeneity. Nielsen and Thybo (2006), for example, found the need to incorporate horizontally stretched heterogeneity to model Pn and Sn codas observed in Russian PNE data. In a teleseismic problem (Cormier et al., 2011), we have applied some of the extensions for anisotropy of scale lengths described by Margerin (2006) and Jing et al. (2014) but have not yet implemented these extensions in the RADIATIVE3D code. A more efficient simulation of the effects of

heterogeneity stretched in a quasi-horizontal direction might be to simply combine random perturbations to thin layering together with isotropic heterogeneity. This can be accomplished with our existing code.

6.1.2 Phase tracking

While RADIATIVE3D currently produces seismic envelope plots, it is technically possible to produce full-waveform seismograms by tracking not only the amplitude, but also the phase (e.g., $\pm\pi/2$) of each phonon as it propagates through the model. By binning the seismic energy as amplitude phasors rather than energy scalars, full seismograms, rather than envelopes, can be produced. These phase factors are actually already calculated by the codebase when it calculates scattering and reflection/transmission probabilities, making it easy add the feature. A disadvantage of phase tracking is that it would require finer temporal resolution in bin spacing, and a corresponding increase in phonon cast count to get suitable bin filling compared to coda envelopes. Thus, full waveform simulation would come at an additional, though manageable, computational cost.

6.1.3 Source spectrum and earthquake slip histories

Currently RADIATIVE3D allows input of single point sources described by moment tensors with no specific options for handling the source time function. The source spectrum can be handled by applying an appropriate scalar factor to each simulated narrow band frequency envelope to simulate the effects of a source spectrum. A possible future application of radiative transport modeling will be to estimate high frequency strong ground motions excited by extended and complex earthquake slip histories. A loop over point sources distributed over a fault plane or within a volume can be added

to achieve envelope simulations for spatially extended earthquake sources.

6.1.4 Ground velocity signal channels

The current signal channels output by RADIATIVE3D virtual seismometers are proportional to the energy flux rate of phonons intersecting the gather area of the seismometers, decomposed into directional channels based on the angle of incidence and polarization of the incoming wave. Although these signal channels allowed for rapid prototyping, and provide interesting and useful signal output for analysis, it is not possible to directly correlate these signals to ground motion, e.g. particle velocity at the site of a seismometer, as would be recording by real seismometers. This is due to the fact that the squared velocity of a ground element is proportional to the energy density in the neighborhood of the element, rather than the flux rate of energy crossing a nearby surface element. Because the flux rate signal mixes phonons arriving with differing wave speeds and at differing incidence angles, it is impossible to extract energy density from the signal after-the-fact.

Additionally, realistic ground motion amplitudes at an interface in an Earth model, e.g. the Earth's surface, are an amplitude-weighted summation of the wave amplitude vectors of the incoming wave and all reflected waves (both the P and S reflections in isotropic media), or equivalently, the weighted sum of all transmitted waves. As such, the reflection and transmission coefficients are needed in order to compute ground motions and directionality from the interaction of an incoming wave with the surface. The process of computing this is sometimes referred to as a free-surface correction, although the procedure is general enough to compute motions at any sharp interface. The process is discussed in Section 2.1.4 in Chapter 2 of this work. Although reflection and transmission coefficients are computed in the RADIATIVE3D code as it currently stands, they are not currently utilized to compute ground motion signals at virtual

seismometers.

Planned improvements to RADIATIVE3D include adjusting the phonon recording and binning procedures to encode amplitudes from energy density, rather than energy flux rate, and to apply free-surface corrections in order to get accurate decomposition into the directional components of motion, so as to enable ground velocity output channels. The process of computing energy density from phonon incidence is discussed further in Section 2.1.5 of Chapter 2 of this work.

6.2 Code validation

Although we see qualitative realism in the modeling scenarios that we have tested thus far, RADIATIVE3D is still in need of proper validation, which would consist of comparing simulation output of RADIATIVE3D against simulations of similar or identical models produced by other simulation techniques, in order to assess whether our implementation of the radiative transport algorithm can be considered reliable and reasonably free from errors in coding or design.

Rigorous validation will depend upon the addition of the free surface corrections discussed above (subsection 6.1.4) so that comparison can be made on the basis of comparable signal channels (ground velocity or ground velocity envelopes).

Examples of previous numerical simulations that may be useful for comparison and validation are contained in reports by Tibuleac et al. (2005) and Bonner et al. (2008). These reports specify the parameters of deterministic crust and upper mantle models of NTS and Kazakh nuclear test sites, parameters of statistical heterogeneity, and show figures of synthetic Lg coda that we are digitizing for comparison with our radiative transport simulations. These validation experiments will enable us to quantify errors in the approximations and assumptions of the radiative transport algorithm, including

neglect of the effects of surface wave to body wave conversions included in numerical syntheses as a function of range.

6.3 Development facilities

RADIATIVE3D development is facilitated by a code repository and version tracking system that we host at `https://rainbow.phys.uconn.edu/geophysics/trac/browser/Radiative3D`. The repository facilitates collaborative editing, branched development, and version tagging and history. The site also features a ticketing system wherein needed changes are identified, prioritized, and organized to guide development. This site is visible to the public and we welcome collaboration on the future development of the code.

Additionally, our group hosts a wiki, one of the purposes of which is to provide additional documentation of the features, functionality, and usage of RADIATIVE3D, and also hosts results of many of the simulations that we have performed with it thus far. The landing page for RADIATIVE3D on our wiki is located at: `https://rainbow.phys.uconn.edu/geowiki/Radiative3D`.

Bibliography

K. Aki. Analysis of the seismic coda of local earthquakes as scattered waves. *J. geophys. Res.*, , 74(2):615–631, 1969.

K. Aki and B. Chouet. Origin of coda waves: Source, attenuation, and scattering effects. *J. geophys. Res.*, , 80(23):3322–3342, 1975.

K. Aki and P. Richards. *Quantitative Seismology: Theory and Methods*, volume 1. WH Freeman & Co, 1980.

B. P. Allmann, P. M. Shearer, and E. Hauksson. Spectral discrimination between quarry blasts and earthquakes in Southern California. *Bull. seism. Soc. Am.*, , 98(4):2073–2079, 2008.

D. L. Anderson. *Theory of the Earth*. Blackwell Scientific Publications, 1989.

C. B. Archambeau. General theory of elastodynamic source fields. *Rev. Geophys.*, , 6(3): 241–288, 1968.

G. Bal and M. Moscoso. Polarization effects of seismic waves on the basis of radiative transport theory. *Geophys. J Int.*, , 142(2):571–585, 2000.

S. Ballard, J. Hipp, A. Encarnacao, C. Young, and B. Kraus. A generalized Earth model software utility. In *prepared for 2012 Monitoring Research Review*, Albuquerque, NM, 2012.

D. R. Baumgardt. Sedimentary basins and the blockage of Lg wave propagation in the continents. *Pure Appl. Geophys.*,, 158(7):1207–1250, 2001.

J. Bonner, A. Stroujkova, and K. Mayeda. Predicting explosion-generated Sn and Lg coda using synthetic seismograms. In *30th Seismic Research Review: Ground-Based Nuclear Explosion Monitoring Technologies*, 2008.

B. G. Bukchin, A. Z. Mostinsky, A. A. Egorkin, A. L. Levshin, and M. H. Ritzwoller. Isotropic and nonisotropic components of earthquakes and nuclear explosions on the Lop Nor test site, China. *Pure Appl. Geophys.*,, 158:1497–1515, 2001.

S. Cao and K. J. Muirhead. Finite difference modelling of Lg blockage. *Geophys. J Int.*, , 115(1):85–96, 1993.

V. Červenỳ. *Seismic Ray Theory*. Cambridge University Press, 2001.

V. Červenỳ and R. Ravindra. *Theory of Seismic Head Waves*. University of Toronto Press, 1971.

S. Chandrasekhar. *Radiative Transfer*. Dover Publications, 1960.

V. F. Cormier and T. S. Anderson. Efficiency of Lg propagation from SmS dynamic ray tracing in three-dimensionally varying crustal waveguides. *Pure Appl. Geophys.*,, 161 (8):1613–1633, 2004.

V. F. Cormier, J. Attanayake, and K. He. Inner core freezing and melting: Constraints from seismic body waves. *Phys. Earth Planet. Inter.*, , 188(3–4):163–172, 2011.

J. W. Eaton et al. GNU Octave. (computer software) http://www.octave.org.

G.-W. Fan, T. Lay, and S. Bottone. Path corrections for source discriminants: A case study at two international seismic monitoring stations. In *Monitoring the Compre-*

hensive Nuclear-Test-Ban Treaty: Seismic Event Discrimination and Identification, pages 651–678. Springer, 2002.

M. Fehler, M. Hoshiba, H. Sato, and K. Obara. Separation of scattering and intrinsic attenuation for the Kanto-Tokai region, Japan, using measurements of S-wave energy versus hypocentral distance. *Geophys. J Int.*, , 108(3):787–800, 1992.

M. D. Fisk. Source spectral modeling of regional P/S discriminants at nuclear test sites in China and the former Soviet Union. *Bull. seism. Soc. Am.*, , 96(6):2348–2367, 2006.

A. M. Forte and R. L. Woodward. Seismic-geodynamic constraints on three-dimensional structure, vertical flow, and heat transfer in the mantle. *J. geophys. Res.*, , 102(B8):17981–17994, 1997.

A. Frankel and R. W. Clayton. Finite difference simulations of seismic scattering: Implications for the propagation of short-period seismic waves in the crust and models of crustal heterogeneity. *J. geophys. Res.*, , 91(B6):6465–6489, 1986.

J. A. Goff, K. Holliger, and A. Levander. Modal fields: A new method for characterization of random seismic velocity heterogeneity. *Geophys. Res. Lett.*, , 21(6):493–496, 1994.

S. Gregersen and F. Vaccari. Lg-wave modelling for the North Sea. *Geophys. J Int.*, , 114 (1):76–80, 1993.

Ó. Gudmundsson and M. Sambridge. A regionalized upper mantle (RUM) seismic model. *J. geophys. Res.*, , 103(B4):7121–7136, 1998.

A. A. Gusev and I. R. Abubakirov. Monte-Carlo simulation of record envelope of a near earthquake. *Phys. Earth Planet. Inter.*, , 49(1–2):30–36, 1987.

S. H. Hartzell. Earthquake aftershocks as Green's functions. *Geophys. Res. Lett.*, , 5(1): 1–4, 1978.

T.-K. Hong and R.-S. Wu. Scattering of elastic waves in geometrically anisotropic random media and its implication to sounding of heterogeneity in the Earth's deep interior. *Geophys. J Int.*, , 163(1):324–338, 2005.

T.-K. Hong, B. Kennett, and R.-S. Wu. Effects of the density perturbation in scattering. *Geophys. Res. Lett.*, , 31(13), 2004.

M. Hoshiba. Separation of scattering attenuation and intrinsic absorption in Japan using the multiple lapse time window analysis of full seismogram envelope. *J. geophys. Res.*, , 98(B9):15809–15824, 1993.

M. Hoshiba. Seismic coda wave envelope in depth-dependent S wave velocity structure. *Phys. Earth Planet. Inter.*, , 104(1–3):15–22, 1997.

Y. Jing, Y. Zeng, and G. Lin. High-frequency seismogram envelope inversion using a multiple nonisotropic scattering model: Application to aftershocks of the 2008 Wells earthquake. *Bull. seism. Soc. Am.*, , 104(2):823–839, 2014.

H. Kanamori. The energy release in great earthquakes. *J. geophys. Res.*, , 82(20):2981–2987, 1977.

B. Kennett, E. Engdahl, and R. Buland. Constraints on seismic velocities in the Earth from travel times. *Geophys. J Int.*, , 122(1):108–124, 1995.

B. L. N. Kennett. *Seismic Wave Propagation in Stratified Media*. Cambridge University Press, 1983.

B. L. N. Kennett. Lg waves and structural boundaries. *Bull. seism. Soc. Am.*, , 76(4): 1133–1141, 1986.

C. Kittel. *Introduction to Solid State Physics*. Wiley, 8th edition, 2004.

K. D. Koper, D. A. Wiens, L. Dorman, J. Hildebrand, and S. Webb. Constraints on the origin of slab and mantle wedge anomalies in Tonga from the ratio of S to P velocities. *J. geophys. Res.*, , 104(B7):15089–15104, 1999.

G. Laske, G. Masters, and C. Reif. Crust 2.0: A new global crustal model at 2x2 degrees. `http://igppweb.ucsd.edu/~gabi/crust2.html`, 2011.

A. Levander, R. England, S. Smith, R. Hobbs, J. Goff, and K. Holliger. Stochastic characterization and seismic response of upper and middle crustal rocks based on the Lewisian gneiss complex, Scotland. *Geophys. J Int.*, , 119(1):243–259, 1994.

L. Margerin. Introduction to radiative transfer of seismic waves. In A. Levander and G. Nolet, editors, *Seismic Earth: Array Analysis of Broadband Seismograms*, pages 229–252. American Geophysical Union, Washington, D. C., 2005.

L. Margerin. Attenuation, transport and diffusion of scalar waves in textured random media. *Tectonophysics*, , 416(1–4):229–244, 2006.

L. Margerin and G. Nolet. Multiple scattering of high-frequency seismic waves in the deep Earth: Modeling and numerical examples. *J. geophys. Res.*, , 108(B5):ESE 5–1 – ESE 5–17, 2003.

L. Margerin, M. Campillo, and B. V. Tiggelen. Monte Carlo simulation of multiple scattering of elastic waves. *J. geophys. Res.*, , 105(B4):7873–7892, 2000.

V. G. Martynov, F. L. Vernon, R. J. Mellors, and G. L. Pavlis. High-frequency attenuation in the crust and upper mantle of the northern Tien Shan. *Bull. seism. Soc. Am.*, , 89 (1):215–238, 1999.

V. Maupin. Numerical modelling of Lg wave propagation across the North Sea Central Graben. *Geophys. J Int.*, , 99(2):273–283, 1989.

C. D. Mendi, B. O. Ruud, and E. S. Husebye. The north sea Lg-blockage puzzle. *Geophys. J Int.*, , 130(3):669–680, 1997.

W. Menke. Case studies of seismic tomography and earthquake location in a regional context. In A. Levander and G. Nolet, editors, *Seismic Earth: Array Analysis of Broadband Seismograms*. American Geophysical Union, Washington, D. C., 2005.

L. Nielsen and H. Thybo. Identification of crustal and upper mantle heterogeneity by modelling of controlled-source seismic data. *Tectonophysics*, , 416(1–4):209–228, 2006.

A. Obermann, T. Planès, E. Larose, C. Sens-Schönfelder, and M. Campillo. Depth sensitivity of seismic coda waves to velocity perturbations in an elastic heterogeneous medium. *Geophys. J Int.*, , 194(1):372–382, 2013.

H. A. Pedersen, J.-P. Avouac, and M. Campillo. Anomalous surface waves from Lop Nor nuclear explosions: Observations and numerical modeling. *J. geophys. Res.*, , 103 (B7):15051–15068, 1998.

W. Phillips, H. Hartse, S. Taylor, A. Velasco, and G. Randall. Regional phase amplitude ratio tomography for seismic verification, Los Alamos National Laboratory. Technical report, LAUR-99-1904, submitted to PAGEOPH, 1999.

J. Przybilla, U. Wegler, and M. Korn. Estimation of crustal scattering parameters with elastic radiative transfer theory. *Geophys. J Int.*, , 178(2):1105–1111, 2009.

S. Pullammanappallil, A. Levander, and S. P. Larkin. Estimation of crustal stochastic parameters from seismic exploration data. *J. geophys. Res.*, , 102(B7):15269–15286, 1997.

A. N. Rachman and T. W. Chung. Depth-dependent crustal scattering attenuation revealed using single or few events in South Korea. *Bull. seism. Soc. Am.,* , 106(4): 1499–1508, 2016.

B. Romanowicz. Can we resolve 3D density heterogeneity in the lower mantle? *Geophys. Res. Lett.,* , 28(6):1107–1110, 2001.

T. Saito, H. Sato, and M. Ohtake. Envelope broadening of spherically outgoing waves in three-dimensional random media having power law spectra. *J. geophys. Res.,* , 107 (B5):ESE 3–1–ESE 3–15, 2002.

H. Sato and M. C. Fehler. Synthesis of wavelet envelope in 2-D random media having power-law spectra: Comparison with FD simulations. *Geophys. J Int.,* , 207(1):333–342, 2016.

H. Sato, M. C. Fehler, and T. Maeda. *Seismic Wave Propagation and Scattering in the Heterogeneous Earth*. Springer-Verlag, 2 edition, 2012.

N. Selby, D. Bowers, A. Douglas, R. Heyburn, and D. Porter. Seismic discrimination in Southern Xinjiang: The 13 March 2003 Lop Nor earthquake. *Bull. seism. Soc. Am.,* , 95(1):197–211, 2005.

C. Sens-Schönfelder, L. Margerin, and M. Campillo. Laterally heterogeneous scattering explains Lg blockage in the Pyrenees. *J. geophys. Res.,* , 114(B7), 2009.

P. Shaw and J. Orcutt. Propagation of PL and implications for the structure of Tibet. *J. geophys. Res.,* , 89(B5):3135–3152, 1984.

P. M. Shearer and P. S. Earle. The global short-period wavefield modelled with a Monte Carlo seismic phonon method. *Geophys. J Int.,* , 158(3):1103–1117, 2004.

P. M. Shearer and P. S. Earle. Observing and modeling elastic scattering in the deep Earth. In H. S. M. Fehler, editor, *Advances in Geophysics, Volume 50: Earth Heterogeneity and Scattering Effects on Seismic Waves*. Elsevier, 2008.

L. R. Sykes and M. Nettles. Dealing with hard-to-identify seismic events globally and those near nuclear test sites. In *Poster presented at the International Scientific Studies Conference*, Vienna, Austria, 2009. Comprehensive Nuclear-Test-Ban Treaty Organization.

W. Tape and C. Tape. *A Geometric Setting for Moment Tensors*. Geophys. J. Int., 2012.

I. Tibuleac, A. Stroujkova, J. Bonner, and K. Mayeda. Predicting explosion-generated Sn and Lg coda using synthetic seismograms. In *27th Seismic Research Review: Ground-Based Nuclear Explosion Monitoring Technologies*, 2005.

H. Tkalčić, V. F. Cormier, B. L. N. Kennett, and K. He. Steep reflections from the Earth's core reveal small-scale heterogeneity in the upper mantle. *Phys. Earth Planet. Inter.*, , 178(1–2):80–91, 2010.

M. D. Trifunac and A. G. Brady. On the correlation of seismic intensity scales with the peaks of recorded strong ground motion. *Bull. seism. Soc. Am.*, , 65(1):139–162, 1975.

W. R. Walter, K. M. Mayeda, and H. J. Patton. Phase and spectral ratio discrimination between NTS earthquakes and explosions. Part I: Empirical observations. *Bull. seism. Soc. Am.*, , 85(4):1050–1067, 1995.

W. R. Walter, E. Matzel, M. E. Pasyanos, D. B. Harris, R. Gok, and S. R. Ford. Empirical observations of earthquake-explosion discrimination using P/S ratios and implications for the sources of explosion S-waves. In *Proceedings of the 29th Monitoring Research Review: Ground-Based Nuclear Explosion Monitoring Technologies*, 2007.

R.-S. Wu. Multiple scattering and energy transfer of seismic waves — separation of scattering effect from intrinsic attenuation — I. Theoretical modelling. *Geophys. J Int.*, , 82(1):57–80, 1985.

K. Yoshimoto. Monte Carlo simulation of seismogram envelopes in scattering media. *J. geophys. Res.*, , 105(B3):6153–6161, 2000.

T.-R. Zhang and T. Lay. Why the Lg phase does not traverse oceanic crust. *Bull. seism. Soc. Am.*, , 85(6):1665–1678, 1995.

L. Zhu and Y. Ben-Zion. Parametrization of general seismic potency and moment tensors for source inversion of seismic waveform data. *Geophys. J Int.*, , 194(2):839–843, 2013.

Index